Development and Analysis of a Solar Humidification Dehumidification Desalination System

Reza Enayatollahi

A thesis submitted to

Auckland University of Technology

in fulfilment of the requirements for the degree of

Doctor of Philosophy (PhD)

2016

School of Engineering, Computer and Mathematical Sciences

ABSTRACT

In this thesis, an investigation was performed in order to understand the performance of a solar humidification dehumidification (HDH) desalination system. Initially, a mathematical model of the system, including solar water heater, condenser, economizer and long duct humidifier was developed. Using a sensitivity analysis, it was found that improving the intensities of heat and mass transfer in the humidifier would significantly enhance the yield of the system. This led to the development of a novel cascading humidifier, in which air was directed through a series of falling water sheets.

An experiment was performed to first identify and characterise flow regimes in the crossflow interactions, and from this, to develop correlations to describe the heat and mass transfer for such interactions. Four flow regimes were identified and mapped based on the Reynolds number of the air and the Weber number of the water.

Subsequently, Buckingham's π theorem and a least squares analysis was employed to develop a series of empirical relations for Nusselt and Sherwood numbers. This led to the proposal of three new dimensionless numbers named the Prandtl Number of Evaporation, the Schmidt Number of Evaporation and the Lewis Number of Evaporation. These describe the transfer phenomena in low temperature evaporation processes with crossflow.

Finally, the new correlations for Nusselt and Sherwood numbers were used to develop a model of a cascading humidifier, incorporated in a solar HDH system. It was found that a cascading humidifier enhances the yield of the HDH system by approximately 15%, while reducing the evaporation area to approximately a quarter of that required in a long channel humidifier.

TABLE OF CONTENT

ACKNOWLEDGEMENTS

I take this opportunity to express my deepest appreciation to my supervisors; Dr. Roy Nates and Dr. Timothy Anderson for their outstanding supervision and patience. I am privileged to have the opportunity to work under supervision of such knowledgeable and dedicated researchers.

Also, I would like to thank my friends; Theepan, Aziz, Noman and Uzair for all the valuable and encouraging discussion we have had.

A big thanks must also go to my soul mate Maryam Gholami who has supported me unconditionally through all these stressful years.

Last but not least, I would like thank my beloved family who have supported me not only in my PhD, but also through my entire life. Thank you Dad, thank you Mom, I could have never done this without your priceless Love and support.

LIST OF FIGURES

LIST OF TABLES

NOMENCLATURE

A	Area (m^2)
Bd	Bodenstein number
c	Capacity ratio
C_B	Bond conductance ($W/m.K$)
c_p	Specific heat ($J/kg.K$)
Ch	Channel
D	Diameter (m)
E	Effectiveness
F	Fin efficiency
F'	Efficiency factor
F_R	Heat removal factor
g	Gravitational acceleration (m/s^2)
G	Radiation (W/m^2)
$\hbar$	Enthalpy (J/kg)
h	Heat transfer coefficient ($W/m^2.K$)
H	Height (m)
j	Mass transfer coefficient (m/s)
k	Thermal conductivity ($W/m.K$)
L	Length (m)
l	Thickness (m)
Le	Lewis number
$\dot{m}$	Mass flow rate (kg/s)
N	Number
N_{ev}	Evaporation number
NTU	Number of transfer units
P	Pressure (kPa)
Pe	Peclet number
Pr	Prandtl number
Q	Flow rate per unit length (m^2/s)
$\dot{Q}$	Rate of heat transfer (W)
r	Radius
R	Specific gas constant ($J/kg.K$)
Re	Reynolds number
Rh	Relative humidity
s	Angle of solar water collector from the horizon
Sc	Schmidt number
Sh	Sherwood number
S_τ	Tube pitch (m)
T	Temperature (K)
Th	Thickness (m)
U	Overall heat transfer coefficient ($W/m^2.K$)
V	Velocity (m/s)
$\dot{V}$	Volumetric flow rate (m^3/s)
w	Tube spacing (m)
W	Width (m)

We	Weber number

Greek Symbols:

μ	Viscosity ($kg/m.s$)
α	Thermal diffusivity (m^2/s)
ε	Emissivity
λ	Mass diffusivity (m^2/s)
ρ	Density (kg/m^3)
σ	Stephan-Boltzmann constant ($W/m^2.K^4$)
ψ	Surface tension (N/m)
ω	Specific humidity ($kg_{water}/kg_{dry\ air}$)

Subscripts:

∞	Bulk fluid
a	Air
abs	Absorbed
amb	Ambient
a-w	Air to water
bf	Baffle
ch	Characteristic
col	Collector
cond	Condenser
conv	Convection
econ	Economizer
ev	Evaporation
hmd	Humidifier
f	Film
F	Falling
g	Gas
gl	Glass cover
i	Inner
in	Inlet
ins	Insulation
l	Liquid
loc	Local
m	Mean
max	Maximum
min	Minimum
n	Nominal
noz	Nozzle
o	Outer
out	Outlet

p	Absorber plate
pr	Perimeter
R	Resultant
s	Contact surface
sat	Saturation
t	Total
Tr	*Tray*
u	Useful
v	Vapour
w	Water
wd	Wind
τ	Tube

Chapter 1 : INTRODUCTION

1.1. Overview

Although nearly three-quarters of the earth surface is covered with water, only 3 percent of this water is potable [1], that is to say, it contains 500ppm or less of salt [2]. The availability of fresh water has been one of the most significant concerns of humankind throughout history. Therefore, most civilisations have developed in fertile regions close to springs and rivers. However, since fresh water was not available everywhere, ancient humankind had to learn how to convert seawater and brackish underground water to a potable form. Historically seawater desalination has been the most expensive method of potable water production [3]. In the fourth century B.C., Aristotle described a method to evaporate contaminated water and then condense the water vapour in order to obtain fresh water [4]. The first recorded application of seawater desalination goes back to the time when long sea voyages were common (around 200 AD). During these voyages seawater was boiled to generate water vapour that was then captured and condensed by large sponges [4].

In recent times however, demand for fresh water has increased rapidly due to population growth. It has been reported that approximately 70% of the world's population will suffer from fresh water shortages by 2025 [5, 6]. Therefore, a large amount of research and development has been aimed at finding efficient techniques for water treatment [7-15].

The amount of potable water required for the basic needs (drinking and cooking) of a family of five is 20 *litres/day* [16], which can increase up to 50 *litres/day* (10

litres/day/person) in extremely hot environments [17, 18]. Hence, choosing a method to provide this depends mostly on the climatological conditions, the availability of the energy sources, and the application of the desalination system. Hence, a broad knowledge of different techniques and their requirements is essential to choosing an appropriate system for a particular location.

1.2. Desalination Techniques

Desalination techniques can be classified as phase change thermal processes, single-phase membrane technologies and hybrid systems, as shown in Figure 1. Thermal processes can be categorized into two groups: direct methods, when all parts are integrated into one system; and indirect methods, where an external heat source provides the thermal energy [19].

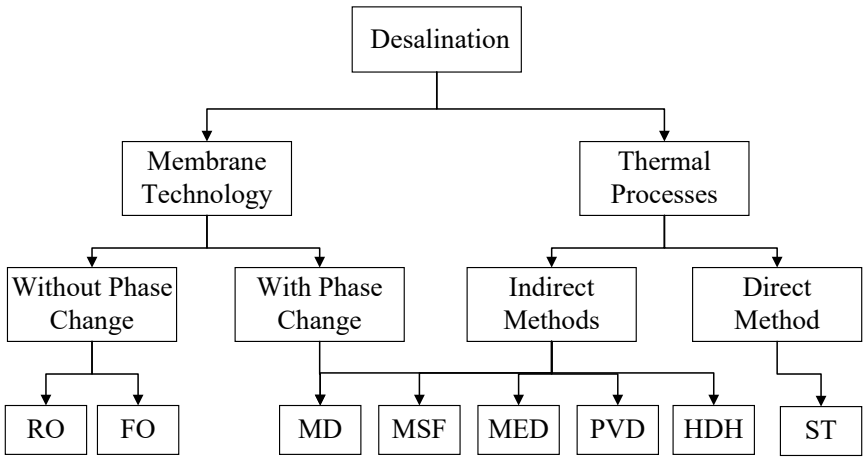

Figure 1. Water desalination methodologies

1.2.1. Membrane Technologies

Membrane technologies use semi-permeable membranes that allow water molecules to pass through and trap salt and other contaminants. This method was initially

limited to urban water treatment, however due to the development of membrane types, usage of this technique has been expanded to other industries and applications [20].

In Forward Osmosis (FO), the solvent would naturally pass through the semi-permeable membrane from the low solute concentration area to the higher concentration area. These systems operate in two steps; firstly, osmotic dilution of the draw solution and secondly, extraction of desalinated water from the diluted draw solution [21]. The post-treatments are often difficult and costly and hence these systems cannot stand as a single process for water desalination [22].

Reverse osmosis (RO) is one of the most efficient methods of desalination for large scale water production, however, these systems require extensive pre-treatment of saline water [23]. This makes them expensive for small scale treatment of highly contaminated feed water [24]. Additionally, in reverse osmosis, significant pressure must be applied in order to overcome the osmotic pressure [23], which necessitates expensive and delicate pumps. Therefore, the application of these systems in seawater desalination, where small scale production is required (remote and rural area), is not cost effective or suitable.

Membrane distillation (MD) is another method, which employs both thermal energy and membrane technology for water purification. Hence, a hydrophobic micro-porous membrane is used which allows only the water vapour to pass [23]. A condenser on the other side of the membrane condenses the water vapour to produce fresh water. These systems are highly sensitive to contaminant concentration and temperature of the feed water, and usually a high water temperature is necessary to provide the required vapour pressure. Also, any air trapped in the membrane causes further resistance to the mass transfer [25].

With the need for high pressure, it is reported that these membrane technologies require a high electrical energy input [26]. Furthermore, membrane technologies, in general, suffer from membrane fouling [27] and so require regular maintenance. These issues preclude the membrane technologies for low-cost solutions.

1.2.2. Thermal Processes

Thermal desalination processes are based on the phase change principle, where heat is added to the water to induce evaporation. Subsequently the latent heat of condensation is removed from the water vapour resulting in condensation. The condensate is potable water, leaving behind contaminates.

In Single Stage Distillation (SSD) systems, as shown in Figure 2, desalination takes place in two steps; firstly, saline water is vaporized by directly supplying heat in the evaporation chamber. Secondly, the water vapour condenses in the condenser, to produce fresh water.

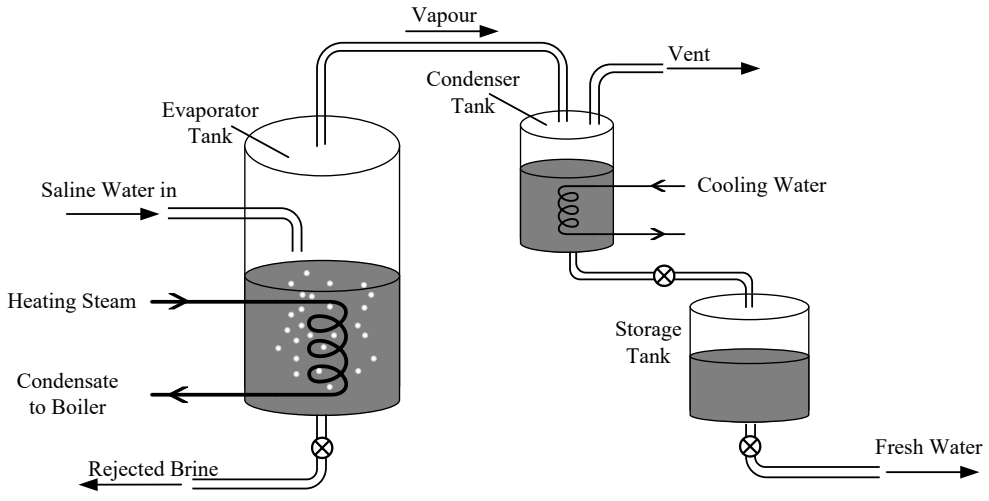

Figure 2. Basic schematic of a single stage distillation (SSD) system [28]

The SSD method, requires a large amount of energy and high temperatures to boil and evaporate water [29]. This method is reported to be suitable only for applications

where having a compact size of the unit is important [29], and where thermal energy sources are high temperature, cheap and abundant. The SSD process has been successfully used in co-generation power plants [30] and marine applications [29]. Decreasing the pressure in the evaporator reduces the boiling temperature and consequently the energy required for evaporation. Furthermore, recovering the latent heat of condensation by sensible heating of the saline feed water increases the overall efficiency of the system. To address this, Multi-Stage Flash (MSF), Multi-Effect Distillation (MED) and Passive Vacuum Desalination (PVD) have been introduced.

In the Multi-Stage Flash (MSF) desalination method, seawater or brackish water is preheated through a series of staged heat exchangers while also being used as the coolant to condense the vapour, as shown in Figure 3. To maximise the yield of these systems high water temperatures and successive pressure reductions at each stage are required [31-33]. However, higher operating temperatures increase the probability of scale formation [34, 35], which impairs the system performance over time.

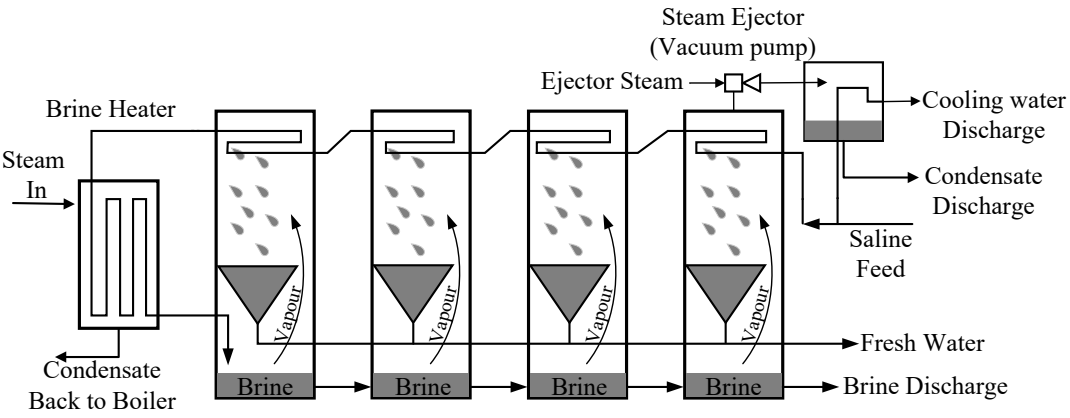

Figure 3. Schematic of a MSF desalination system [31]

Similar to MSF systems, Multi-Effect Distillation (MED) units as shown in Figure 4, consist of a series of low-pressure heat exchangers, named “effects”. However, MED systems reuse the latent heat of condensation to vaporize the seawater [23], making them

more efficient than MSF [36]. Typically, MED needs high brine temperatures and low pressures at the first stage to maximize vaporization. However, some systems have been designed to operate with lower temperatures [37], which reduces fouling but necessitates additional heat transfer area [32].

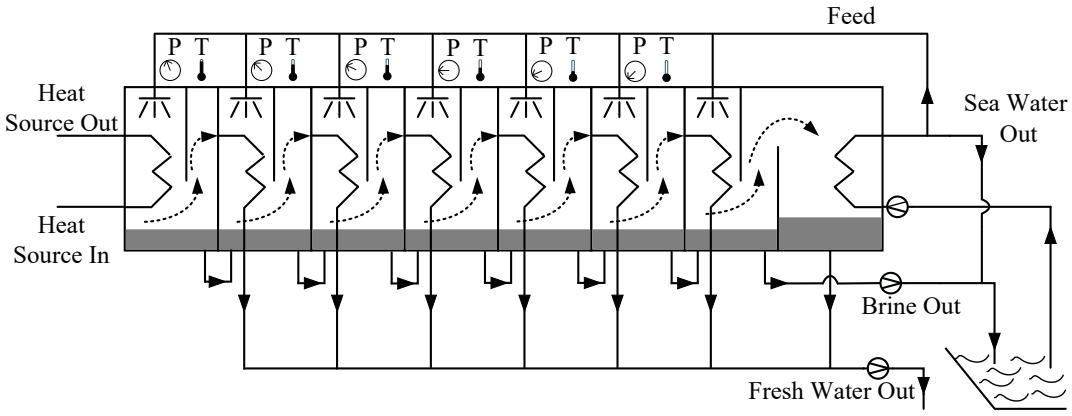

Figure 4. Schematic of a MED desalination system [38]

To provide the low pressure for these MED and MSF systems, vacuum pumps are employed, which increase the energy used as well as the demand for more maintenance [39]. This has led to the development of Passive Vacuum Desalination (PVD), as shown in Figure 5.

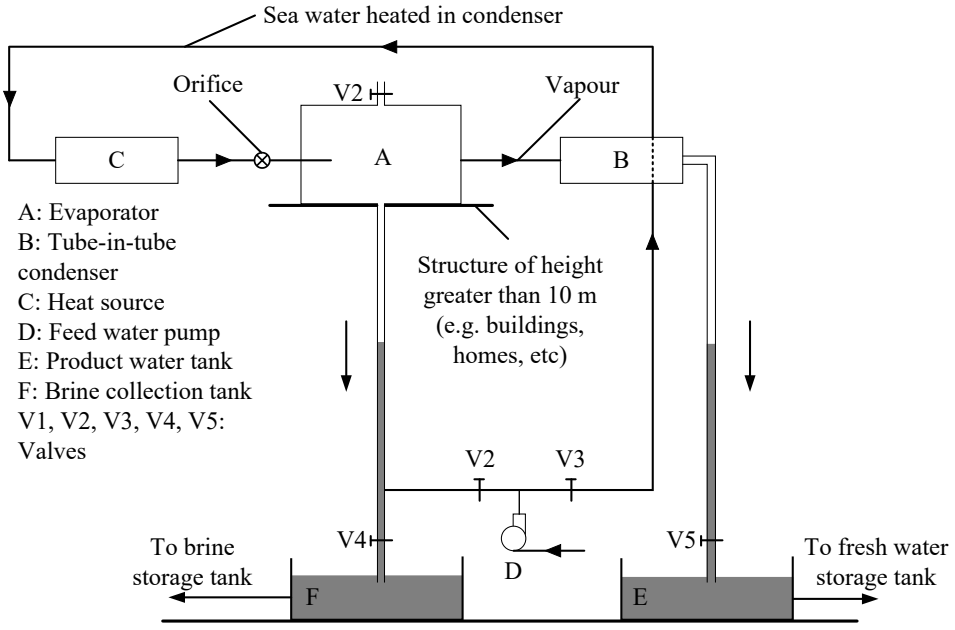

Figure 5. Schematic of a PVD desalination unit [39]

In PVD, the vacuum condition is provided by the falling water from the bottom of evaporator making the PVD system independent of vacuum pumps. However, to provide the required vacuum, a height of at least 10 *m* is required [39].

In all of the above mentioned distillation techniques, either a high temperature source to increase the saline water temperature to the boiling point, or an effective vacuum pressure to reduce the boiling point of saline water is required. These issues preclude these methods for use in low-cost application.

To this end, the Humidification Dehumidification (HDH) desalination technique is an alternative to distillation processes. A typical HDH system, as shown in Figure 6, uses air as the carrier gas [40] to transport water vapour from a humidifier to a dehumidifier. Since this method is based on the humidification of an air stream, it can be operated at low temperatures and atmospheric pressure. In these systems, the required heat of evaporation is transferred to either the water stream, the air stream or both. Subsequently the two streams interact in the humidifier, which results in humidification of the air stream. Afterwards, the latent heat is removed from the moist air by a cooling fluid in the dehumidifier, resulting in the production of potable water.

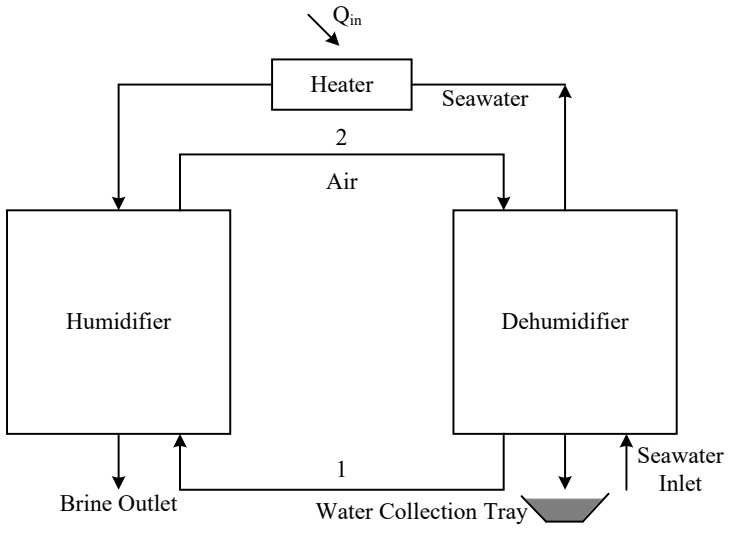

Figure 6. Schematic of a water heated HDH desalination unit [41]

Of the currently available desalination systems, the HDH method has been shown to be a cost and energy efficient solution for small-scale production of potable water for a family house or supplying water to remote and rural area [41-43]. Unlike membrane based technologies, HDH systems can purify saline water with higher concentrations of salt, which makes them a strong candidate for production of desalinated water from natural gas wells [44]. The other advantages of HDH systems are their simplicity, moderate installation cost, flexibility in capacity and low operating cost [40].

1.3. Solar Assisted Desalination

Many of the current desalination plants use fossil fuels to provide the heat energy for thermal processes and electrical energy for membrane technologies [42], but these are often costly and not environmentally sustainable [45]. Developing desalination systems that can be operated with renewable sources of energy would appear to be economic, and environmentally friendly.

As water shortages are mostly seen in barren and remote areas that are rich in solar energy, using solar energy to provide the required energy is an obvious solution for both water shortage and pollution in such areas. Solar energy is the largest source of energy on the earth and all the other sources of energy are derived from it.

Many investigations have explored the use of solar energy for various desalination methods [46-57]. Among the desalination methods mentioned in the previous section, distillation processes (SSD, MSF, MED, PVD) and membrane technologies (RO, FO, MD) require a high value energy sources, making them inappropriate to be coupled with solar energy.

A solar still (ST), shown in Figure 7, is perhaps the simplest solar assisted desalination method [58]. In this method, water distillation and heat absorption occur in a single chamber. The water vapour forms due to solar irradiance and then rises up to the transparent cover, where condensation takes place as a result of heat transfer to the outer environment. The condensate trickles down due to the slope of the transparent cover and can be collected from the bottom side.

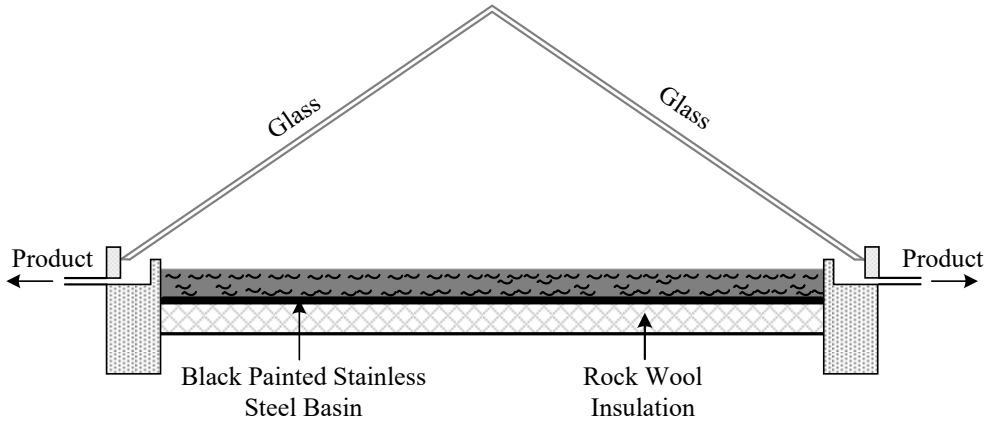

Figure 7. Schematic of a solar still distillation system [58]

Due to the condensation on the transparent cover, these systems lose latent heat to the environment. Furthermore, solar stills are categorized as a direct method of desalination, where direct heating increases the temperature of the glass condensing surface which negatively influences the performance of these systems [59, 60]. Consequently the yield of these systems is relatively low, with a daily production of 3-4 *litre/m*^{2} [61].

1.4. Solar Assisted HDH Desalination

The HDH desalination method is based on the same principles as solar stills, but the heating, humidification and dehumidification occur in different components and hence they can be independently designed [62]. As a consequence, a variety of different

configurations can be used in HDH systems [41]. Additionally, decoupling the heater in the HDH desalination technique eliminates the undesirable impact of direct heating.

A solar HDH desalination system, shown in Figure 8, is composed of three principal components; solar air/water heater, humidifier and dehumidifier (condenser). Enhancing the performance of these individual components would increase the overall performance of the system.

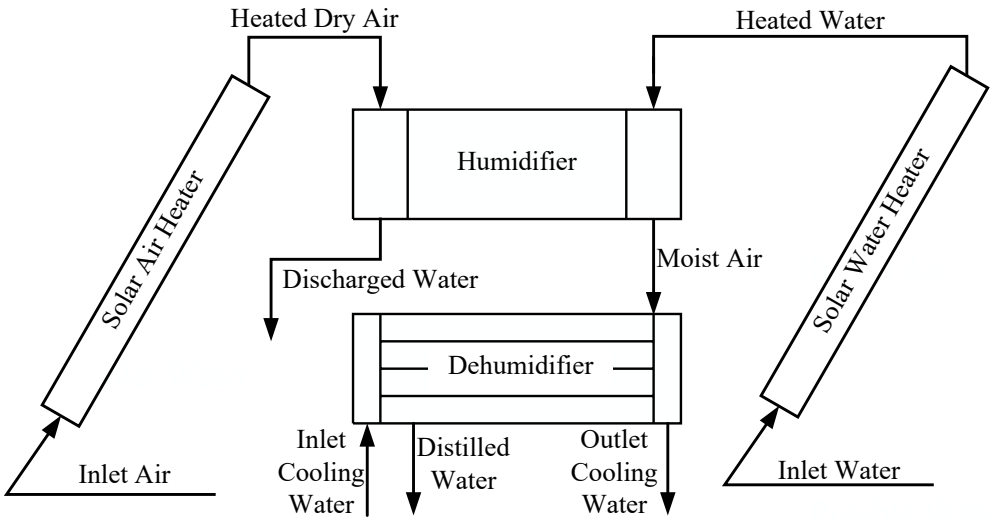

Figure 8. Components of a typical solar assisted HDH desalination system

Additionally, a challenge to the HDH desalination system is choosing the appropriate cycles for air and water streams, based on climatic and operational conditions, as this influences the yield of the system significantly. Choosing appropriate cycles of air and water in a HDH desalination system depends on the relative technical advantages and disadvantages of the system as well as the environmental conditions.

As shown in Figure 9, the HDH desalination systems can be classified in four main groups based on air and water cycles; “Closed-Air/Closed-Water”, “Closed-Air/Open-Water”, “Open-Air/Closed-Water” and “Open-Air/Open-Water”.

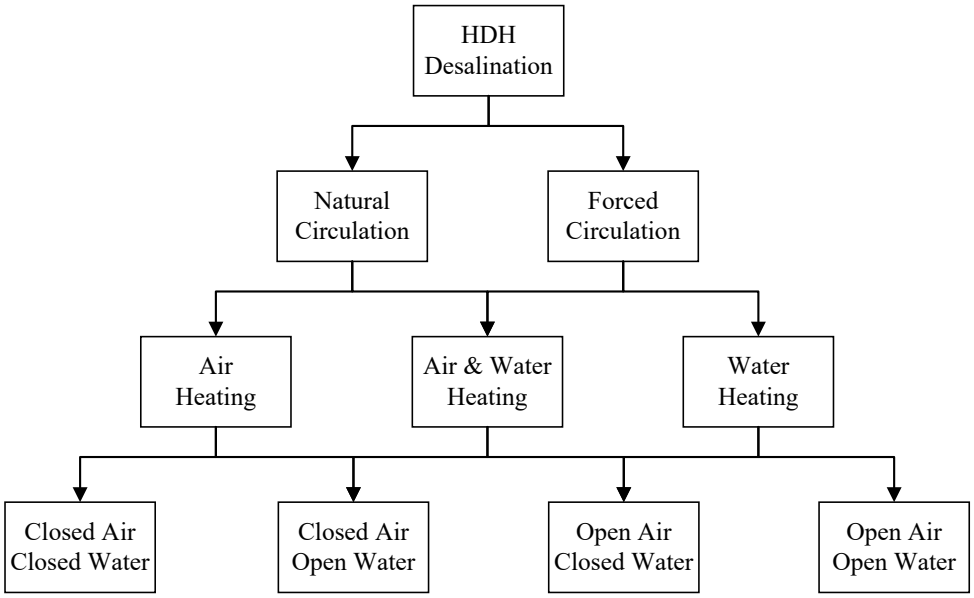

Figure 9. Classification diagram of HDH desalination technique

Further, HDH desalination techniques can also be divided in two groups: forced or natural circulation and also based on the heating technique; air heating, water heating or air and water heating systems.

1.4.1.1. Closed-Air/Closed-Water

In "Closed-Air/Closed-Water" systems, as the name implies, both the air and water streams remain in the system. This is similar to a Solar Still (ST), in that it recovers the latent heat of condensation and hence improves the overall efficiency of the system. A schema of the "Closed-Air/Closed-Water" cycle, studied by Yuan et al. [10], is shown in Figure 10. Both humidification and dehumidification processes occur in a single thermally insulated tower, by continuously circulating air between the humidifiers and condensers. Hot water from a solar collector is sprayed over honeycomb humidifiers, while the condensers are fed with seawater. The outflow water from the humidifiers is returned to the seawater pool and hence, the remaining thermal energy is recovered.

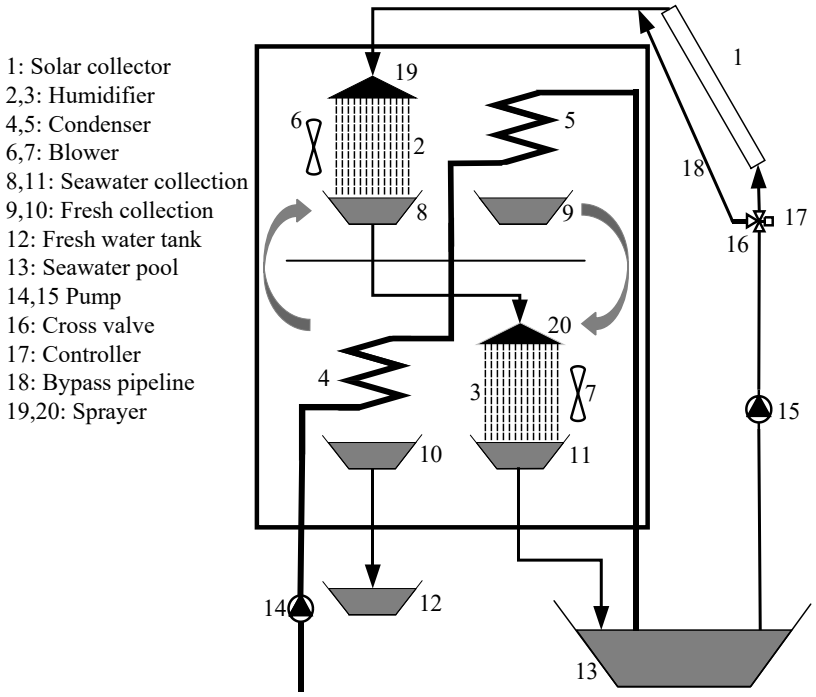

Figure 10. Schematic of Yuan et al. HDH system [10]

It was reported that, owing to the seawater tank, the system was able to operate 24 hours a day with a production of 5.2 *litre/m^2/day* in June and 2.7 *litre/m^2/day* in December in Xi'an, China. It was also found that for a fixed solar absorber area, production decreased with increasing water flow rate and that by proper utilization of the latent heat, the process efficiency could increase.

In 2014, Zamen et al. [63] performed an experimental investigation on a two-stage solar HDH system, which is illustrated in Figure 11. It was reported that a two-stage HDH desalination unit had 20% more production than a similar single-stage unit. The maximum production of potable water during the summer time was reported to be 7.25 *litre/m^2/day* with 80 *m^2* of solar absorber area. They concluded that although the unit production improved with additional stages, the improvement was negligible when more than two stages were used. Considering the cost of unit production, they suggest the best choice would be a two-stage unit.

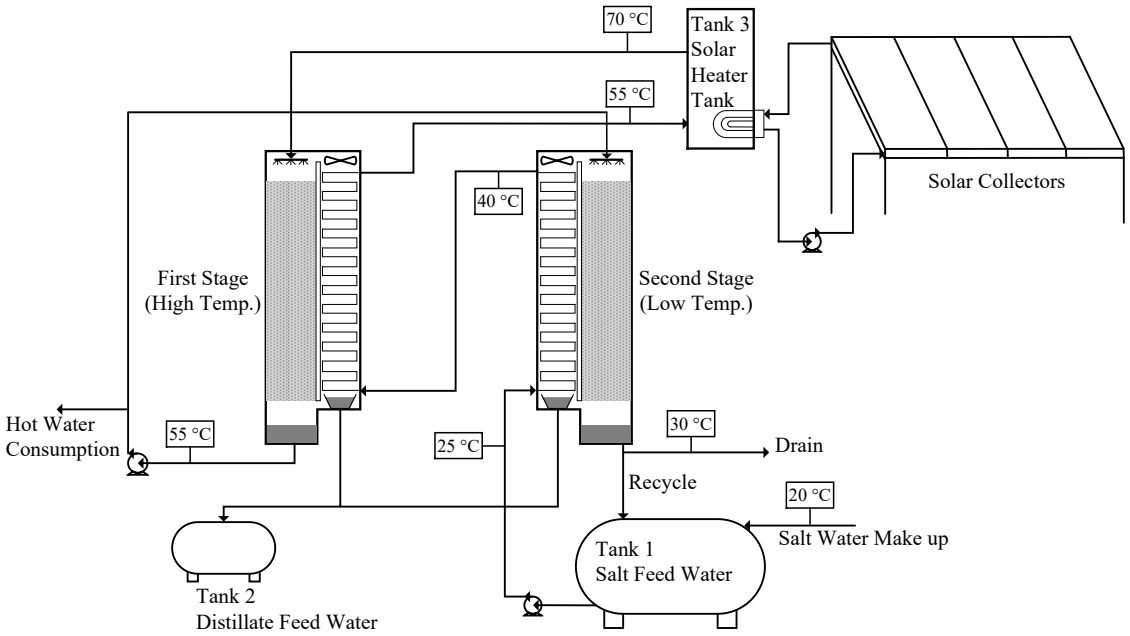

Figure 11. Two stage evaporation/condensation HDH desalination unit [63]

Mahmoud et al. [64] carried out a theoretical and experimental investigation on a HDH desalination unit illustrated in Figure 12. Both "Closed-Air/Closed-Water" and "Open-Air/Closed-Water" cycles were tested. They found that the temperature of the outlet brine from the humidifier was sufficiently high so as to be further used, and they noted that the closed air cycle was more productive than the open-air system.

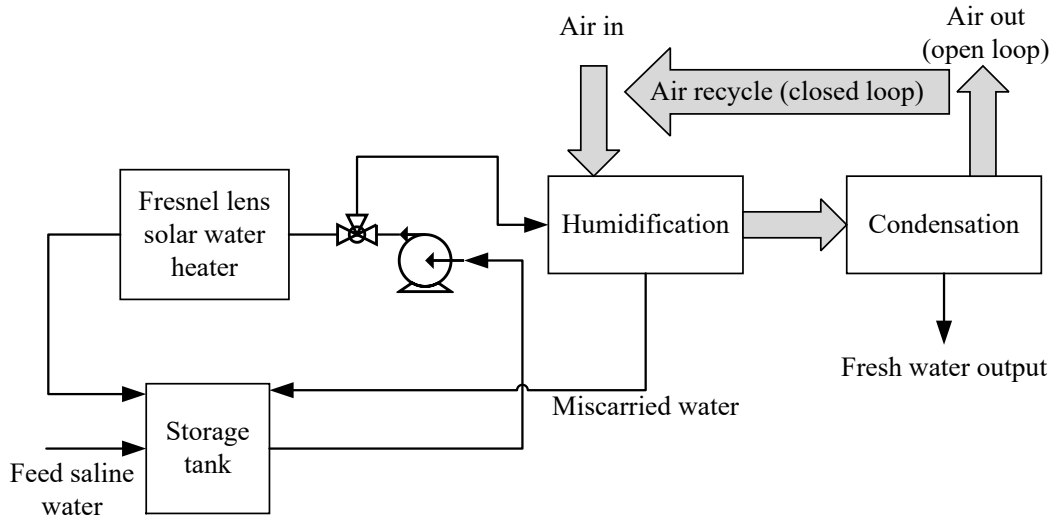

Figure 12. HDH desalination with fresnel lens solar heater [64]

In this regard, the possibility of producing 60 *litre/m^2/day* and 112 *litre/m^2/day* were reported for open and closed air cycles respectively.

From these studies, it can be concluded that the application of "Closed-Air/Closed-Water" units can be justified in circumstances where the ambient air has lower energy and moisture content than the exhaust air from the condenser. Also, these systems are suited to conditions where the temperature of the salt water supply is significantly lower than that of discharged water from the humidifier. However, the concentration of saline water in these systems continuously increases after each cycle, which increases the risk of sedimentation.

1.4.1.2. Closed-Air/Open-Water

The "Closed-Air/Open-Water" HDH cycle, as the name implies, circulates the air within the system, while discharging the brine. Shown in Figure 13 is the system tested by Al-Hallaj et al. [65], in which water is sprayed over the evaporator after being pre-heated by moist air in the condenser and passing through a flat plate solar collector. The air is cycled between the evaporator and condenser alternately being humidified and dehumidified. It was reported that a maximum output was achieved at an optimal water flow rate, beyond which output diminished because of lower evaporation and condensation efficiencies at higher flow rates. This was explained by increased heat and mass transfer coefficients at higher water flow rates. The effect of air velocity was also reported to be significant at low temperatures, while it had a smaller effect at higher temperatures. Thus, natural air circulation was suggested only for high temperature conditions.

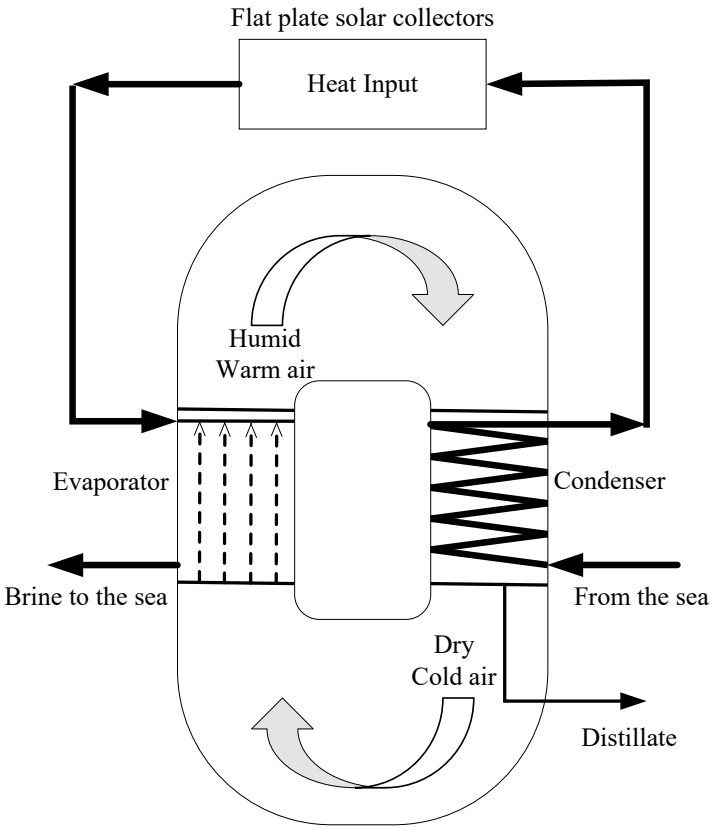

Figure 13. The HDH desalination structure presented by Al-Hallaj et al. [65]

Amer et al. [66] carried out a theoretical and experimental investigation on the "Closed-Air/Open-Water" HDH desalination system shown in Figure 14. The main intention of the study was to improve the cycle by evaluating the effect of operating conditions on the unit productivity. As such, the effect of actual wet area as well as the mass transfer coefficients were evaluated by examining three different materials as the packed bed. Also, both forced and natural circulation of air were examined.

The maximum productivity of the unit was reported for a packed bed with wooden slates while the system operated with forced air circulation. The maximum productivity of the unit was 5.8 *litre/hr* with the inlet water temperature to the humidifier at 85°*C* and the water mass flow rate at 2.8 *kg/min*.

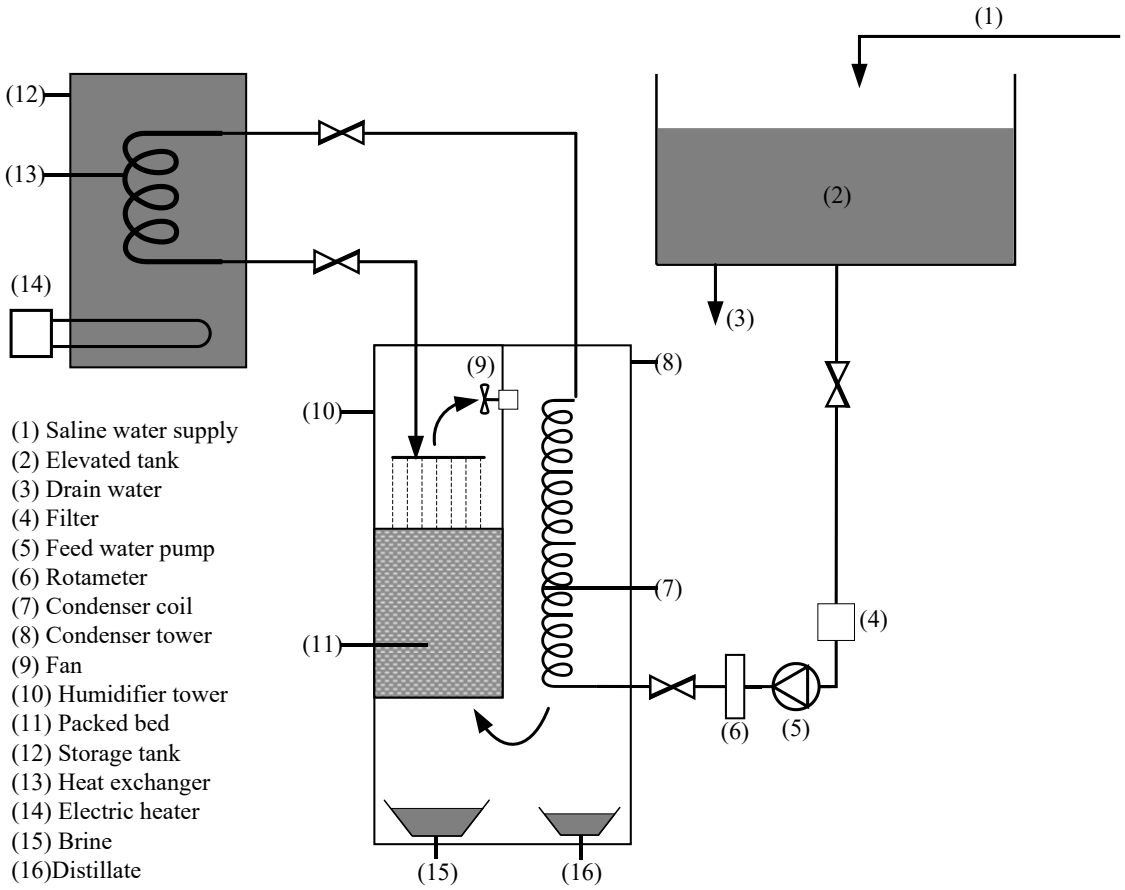

Figure 14. HDH desalination diagram presented by Amer et al. [66]

The application of "Closed-Air/Open-Water" system can be justified in cases where the ambient air has both a low temperature and moisture content, and the energy content of the brine leaving the system is sufficiently low.

1.4.1.3. Open-Air/Closed-Water

Dai et al. [67] examined a HDH desalination system with "Open-Air/Closed-Water" cycle. As shown in Figure 15, a water heating and forced circulation for both air and water streams was used. It was reported that the unit overcame the difficulty of simultaneously increasing the evaporation temperature and decreasing the condensation temperature by using a honeycomb humidifier with forced convection. It was also

concluded that the water and airflow rates and the saline water temperature were the most influential parameters on the unit's performance.

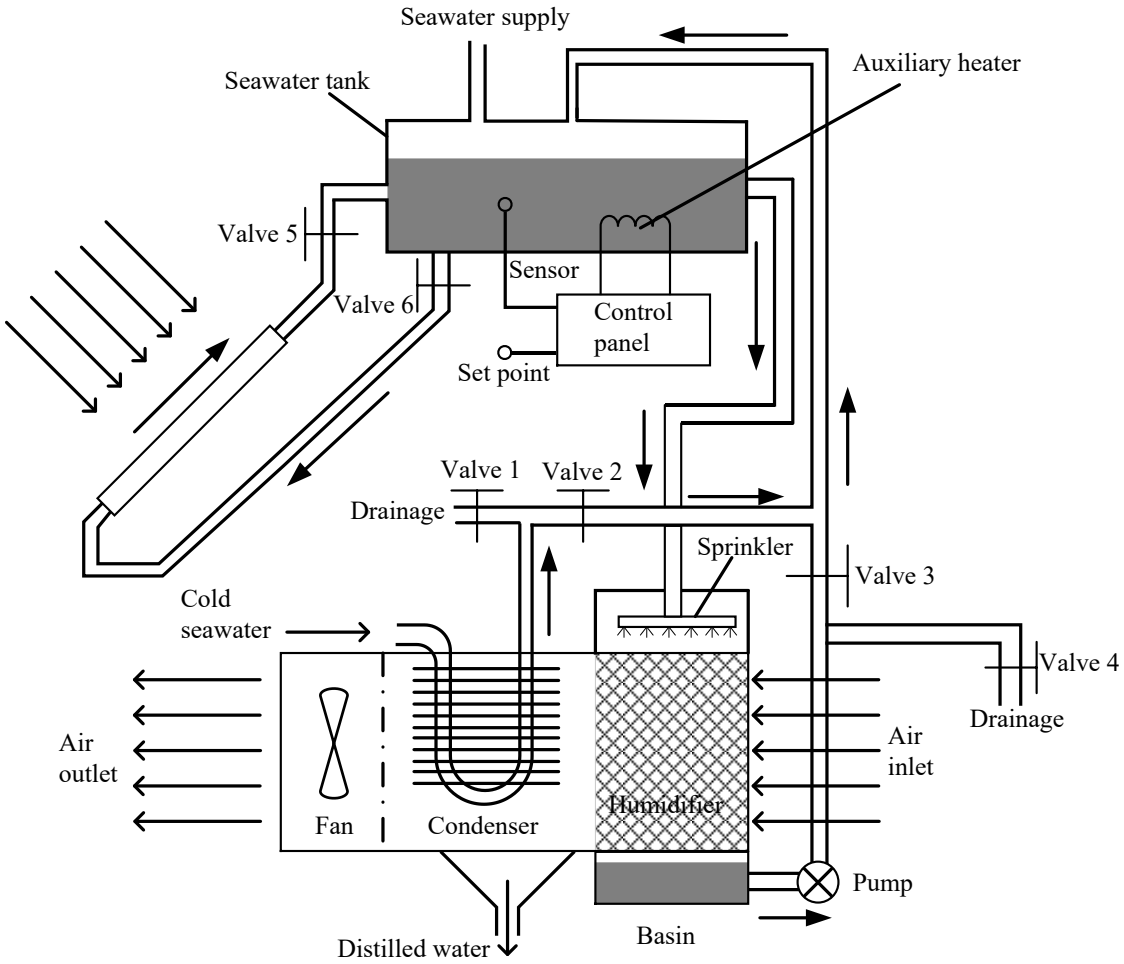

Figure 15. HDH desalination unit presented by Dai et al. [67]

In a subsequent study, Dai et al. [68] mathematically modelled the experimental unit shown in Figure 15. It was found that an increase in water production occurred with increasing inlet air temperature and relative humidity and with decreasing seawater temperatures. Increasing mass flow rates of both feed and cooling water was also found to raise water production.

Al-Enezi et al. [2] performed both mathematical modelling and an experimental investigation on a HDH desalination system with a "Closed-Air/Open-Water" cycle. As illustrated in Figure 16, both the air and water streams were heated and forced circulation

for both streams was used. The highest water production was reported to be at high hot water temperatures, cold cooling water temperatures, high airflow rates and low hot water flow rates.

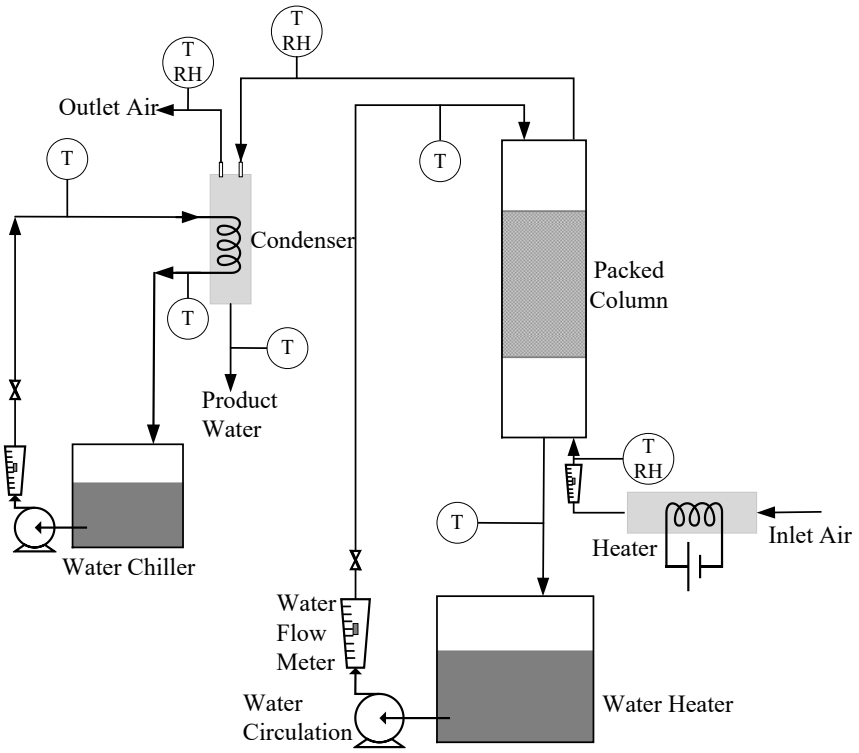

Figure 16. Experimental HDH desalination unit presented by Al-Enezi et al. [2]

In 2008 another experimental study was carried out by Yamali et al. [69] on an "Open-Air/Closed-Water" cycle. As shown in Figure 17, both the air and water streams were heated, and forced circulation were used for both streams. It was reported that an increase in production occurred with an increase in the initial water temperature and quantity of water in the storage tank. Additionally, an increase of 15% in production was achieved by using a double pass solar air heater. The water production and mass flow rates of the seawater being desalinated and cooling water were reported to be proportional, while production decreased with an increasing airflow rate.

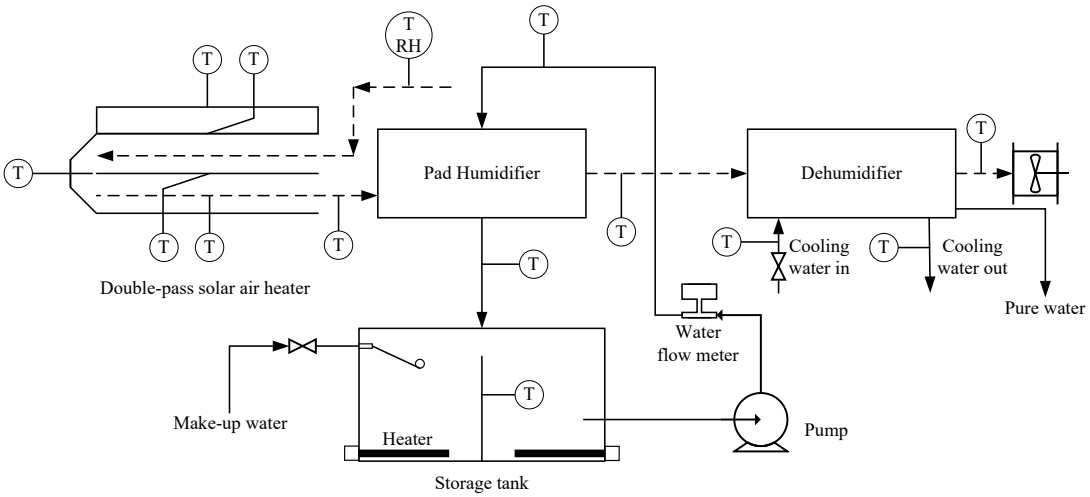

Figure 17. Air heating HDH desalination unit presented by Yamali et al. [69]

From these, it can be concluded that the "Open-Air/Closed-Water" systems can be used in conditions where the exhaust air from the condenser has a lower temperature and moisture content than the ambient air, and the temperature of the discharged brine from the humidifier is high enough so its energy can be used in the system.

1.4.1.4. Open-Air/Open-Water

Yuan et al. [70] carried out an investigation on a solar HDH desalination system with "Open-Air/Open-Water" cycle. As shown in Figure 18, both air and water heating with forced circulation were employed.

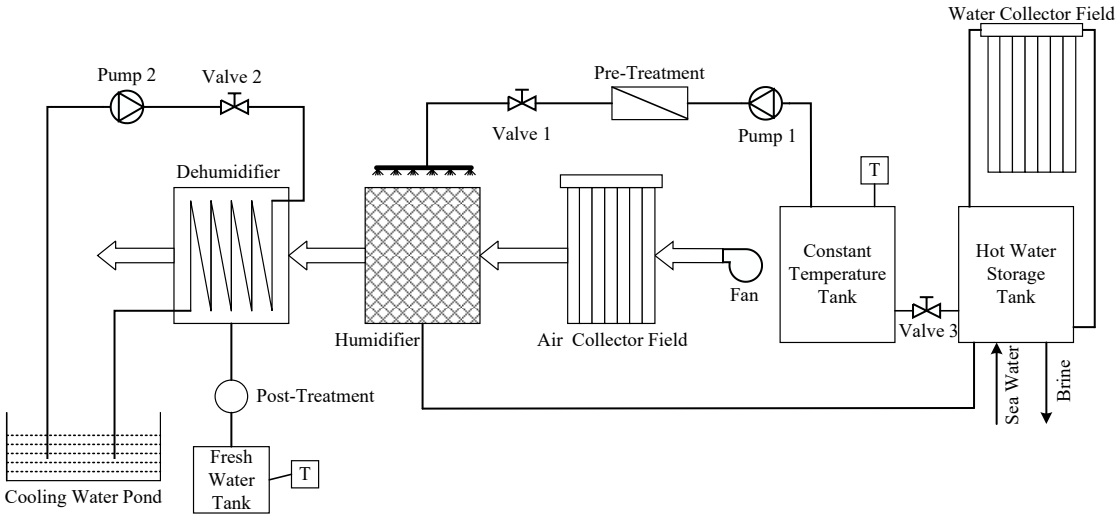

Figure 18. Schematic of HDH structure presented by Yuan [70]

They stated that the system produced 10.52 *litre/m^2/day* of fresh water, with the average intensity of solar radiation was 550 W/m^2.

However, it is found that HDH desalination units with "Open-Air/Open-Water" cycles are likely to have high heat losses to the exit streams. Therefore, using such a cycle can be only justified if the ambient air has more energy and moisture content than the air leaving the condenser, and the temperature of the brine leaving the humidifier is lower or close to the inlet seawater temperature. Otherwise, an additional heat exchanger should be provided to recover the heat.

1.5. Research Question

From the literature, it can be concluded that despite the work undertaken, there is still potential for the development of HDH desalination systems, as there are no definitive systems specifically in small-scale applications. Therefore, this work aims to determine:

How can we develop an efficient solar HDH desalination system for small-scale fresh water production?

Chapter 2 : MATHEMATICAL MODELLING OF A SOLAR HDH DESALINATION SYSTEM

2.1. Overview

To begin to address the research question posed in the previous chapter, an understanding of the HDH desalination cycle, as well as the contribution of each component is required. In this regard, a mathematical model of the system needs to be developed. With the aid of this model, the effect of operating parameters, as well as variations in climatic conditions, on the overall performance can be evaluated. The relative benefits and shortcomings of the system can also be identified and hence the system energy performance can be improved.

As mentioned in Chapter 1, the choice of configuration of the system mostly depends on the environmental conditions of the system. For this study, climatological conditions of a typical summer day in New Zealand is considered. It was assumed that the average radiation received is $1000W/m^2$, the average wind velocity is $5m/s$, the pressure is $1\ atm$, the average seawater temperature (for desalination) is $15°C$, and the ambient air temperature is $20°C$ with a relative humidity of 50%. Additionally, it is assumed that the properties of pure water were applicable to the seawater being desalinated.

2.2. HDH Desalination System Development

In order to achieve an efficient HDH desalination system, an “Open-Air/Open-Water” cycle was chosen. As shown in Figure 19 the main components of the proposed

solar HDH desalination system are the solar water heater, humidifier, condenser and the economizer. The water was heated and for simplicity, the humidifier was considered to be a long channel with counter-current air and water flow pattern. This configuration would reduce the effects of sedimentation on the performance of the humidifier and at the same time reduce the energy required to circulate air and water. A gas-liquid single pass shell and double pass tube heat exchanger was proposed for the condenser, which has a small pressure drop on both air and water stream and hence lowers the energy input to the system.

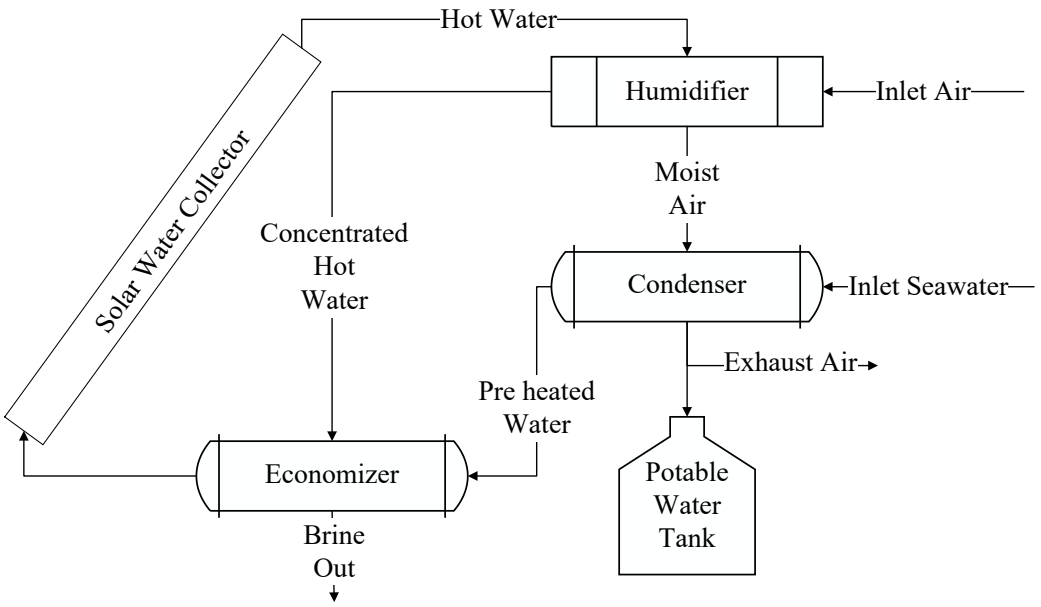

Figure 19. Proposed solar heated HDH desalination unit

Considering seawater as the cooling fluid and assuming effective cooling of the moist air in the condenser, the energy and moisture content of the exhaust air were expected to be lower than that of the ambient air. On this basis, an open cycle for the air stream appears to be suitable for the system. Forced circulation for both air and water streams was included.

Potable water production occurs in the condenser, where the moist air from the humidifier is cooled by the cooling fluid. As shown in Figure 20, the change in the specific humidity of air across the condenser defines the amount of fresh water produced.

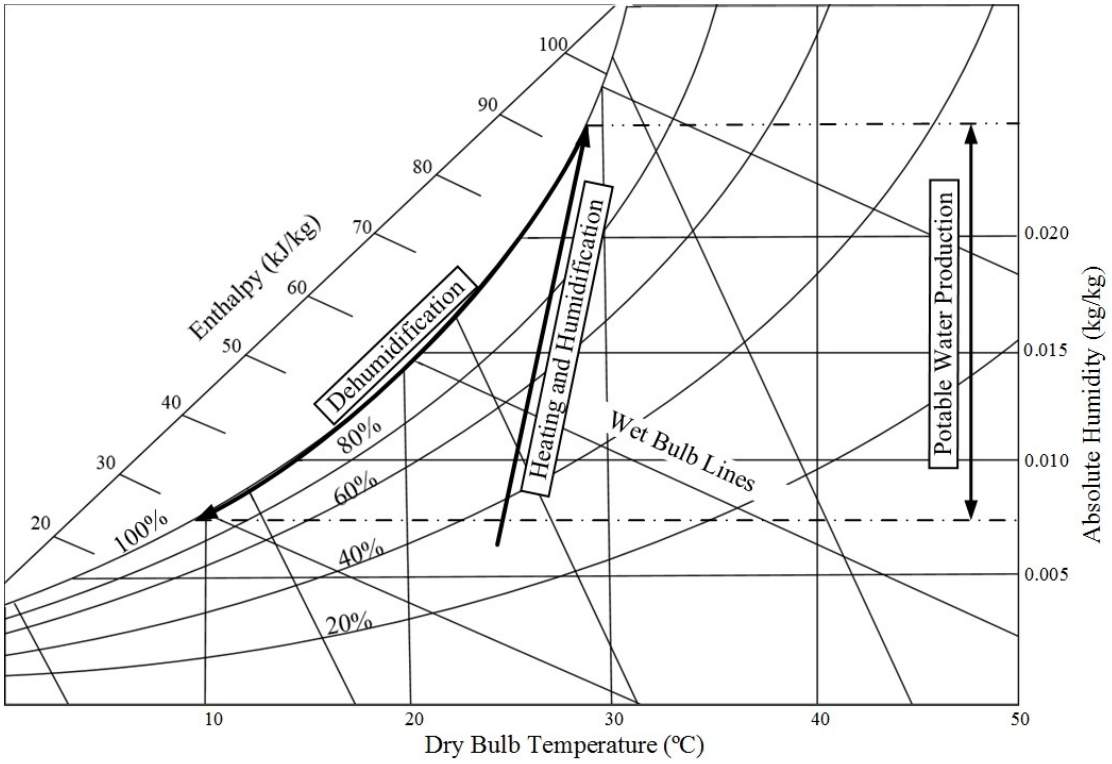

Figure 20. Psychrometric cycle of humidification dehumidification desalination process

2.3. Model Development

As was shown in Figure 19, the proposed HDH desalination system included four main components: solar water collector, condenser, humidifier and economizer. The following sections detail the mathematical model developed for each of these components.

2.3.1. Solar water collector

Flat plate solar water collectors have been used extensively in HDH and other desalination methods [71-74]. A simple double glazed flat plate solar collector was chosen and modelled as the heater.

The Hottel-Whillier equations (Equations 1 to 12) [75] are used to model the collector. The outlet water temperature from the collector can be determined from Equation 1.

$$T_{w,out,col} = T_{w,in,col} + \frac{\dot{Q}_{u,col}}{\dot{m}_{w,in,col} c_{p_{w,col}}} \tag{1}$$

The rate of useful energy gained by the water, in Equation 1, is computed by solving Equations 2 and 3 simultaneously.

$$\dot{Q}_{u,col} = A_{col}[G_{abs} - U_{col}(T_{p,col} - T_{amb})] \tag{2}$$

$$T_{p,col} = T_{w,in,col} + \frac{\dot{Q}_{u,col}/A_{col}}{U_{col} F_{R.col}}(1 - F_{R,col}) \tag{3}$$

In which, the heat removal factor ($F_{R,col}$), in Equation 3 can be calculated from Equation 4.

$$F_{R,col} = \frac{\dot{m}_{w,in,col} c_{p_{w,col}}}{A_{col} U_{col}} \left[1 - e^{\frac{-A_{col} U_{col} F'_{col}}{\dot{m}_{w,in,col} c_{p_{w,col}}}}\right] \tag{4}$$

In Equation 4, F'_{col} is the collector efficiency factor defined by Equation 5.

$$F'_{col} = \frac{1/U_{col}}{w\left[\frac{1}{U_{col}(2S_\tau F + D_{o,\tau,col})} + \frac{1}{C_B} + \frac{1}{h_{i,\tau,col}\pi D_{i,\tau,col}}\right]} \tag{5}$$

Where F is the fin efficiency given by Equation 6.

$$F = \frac{1}{mL_\tau}\left[\frac{\exp(mL_\tau) - \exp(-mL_\tau)}{\exp(mL_\tau) + \exp(-mL_\tau)}\right] \tag{6}$$

And m is defined by Equation 7.

$$m = \sqrt{U_{col}/k_p l_p} \tag{7}$$

The collector overall heat loss coefficient (U_{col}) is the summation of the bottom, edge and top heat loss coefficients. The bottom and edge heat loss coefficients can be calculated from Equations 8 and 9, respectively.

$$U_{bottom} = \frac{k_{ins}}{l_{ins}} \tag{8}$$

$$U_{edge} = U'_{edge}\left(\frac{A_{pr}}{A_{col}}\right) \tag{9}$$

U'_{edge} is the edge overall loss coefficient, where, as reported in the literature [75], was assumed to be 0.5. Equation 10 is used to determine the top loss coefficient [76].

$$U_{top} = \left[\frac{N_{gl,col}}{\frac{Z}{T_{p,col}}\left(\frac{T_{p,col} - T_{amb}}{N_{gl,col} + B}\right)^{0.33}} + \frac{1}{h_{wd}}\right]^{-1}$$

$$+ \frac{\sigma(T_{p,col+}T_{amb})({T_{p,col}}^2 + {T_{amb}}^2)}{[\varepsilon_{p,col} + 0.5N_{gl,col}(1 - \varepsilon_{p,col})]^{-1} + \frac{2N_{gl,col} + B - 1}{\varepsilon_{gl,col}} - N_{gl,col}} \quad (10)$$

Where $N_{gl,col}$ is the number of glass covers, and B and Z are empirical variables, which are given by Equations 11 and 12.

$$Z = 250[1 - 0.0044(s - 90)] \quad (11)$$

$$B = \left[1 - 0.04h_{wd} + 0.0005{h_{wd}}^2\right][1 + 0.091N_{gl,col}] \quad (12)$$

2.3.2. Condenser and Economizer

The condenser was modelled as a gas-liquid single pass shell and double pass tube heat exchanger. These heat exchangers have been previously used as dehumidifiers in HDH desalination systems [15, 77]. For shell and tube heat exchangers, the effectiveness-NTU method can be used to determine the conditions of outlet fluids, as given by Equations 13 and 14 [78]. Both condenser and economizer were assumed to be adiabatic.

$$T_{a,out,cond} = T_{a,in,cond} + \frac{\dot{Q}_{NTU}}{\dot{m}_{a,in,cond}{c_p}_{a,in,cond}} \quad (13)$$

$$T_{w,out,cond} = T_{w,in,cond} - \frac{\dot{Q}_{NTU}}{\dot{m}_{w,in,cond} c_{p_{w,in,cond}}} \quad (14)$$

Where the actual heat transfer rate, $\dot{Q}_{NTU}$, is the product of the effectiveness and maximum possible energy gain, as presented in Equation 15.

$$\dot{Q}_{NTU} = E\dot{Q}_{Max} \quad (15)$$

Equation 16 can be used to compute the maximum possible energy gained.

$$\dot{Q}_{Max} = (\dot{m}c_p)_{min}(T_{a,in,cond} - T_{w,in,cond}) \quad (16)$$

Where $(\dot{m}c_p)_{min}$ is the smaller of the heat capacity rate of air $(\dot{m}_a c_{p_a})$ and heat capacity ratio of water $(\dot{m}_w c_{p_w})$, and Effectiveness for a heat exchanger that involves phase change is given in Equation 17.

$$E_{cond} = 1 - \exp(-NTU) \quad (17)$$

And Equation 18 gives the NTU.

$$NTU = \frac{U_{cond} A_{cond}}{(\dot{m}c_p)_{min}} \quad (18)$$

Now, the overall heat transfer coefficient of the condenser can be determined by Equation 19 [78].

$$U_{cond} = \frac{1}{\frac{1}{h_a} + \frac{A_{i,\tau} \ln\left[\frac{r_{o,\tau}}{r_{i,\tau}}\right]}{2\pi k_\tau L_\tau} + \frac{A_{i,\tau}}{A_{o,\tau}} \frac{1}{h_w}} \tag{19}$$

A similar liquid-liquid heat exchanger was used as the economizer. Again, the effectiveness-NTU method was used to determine the outlet conditions of the fluids from the economizer. Equation 20 is used to determine the effectiveness for economizer as there is no phase change.

$$E_{econ} = 2\left\{1 + c + \sqrt{1 + c^2} \frac{1 + exp\left[-NTU\sqrt{1 + c^2}\right]}{1 - exp\left[-NTU\sqrt{1 + c^2}\right]}\right\}^{-1} \tag{20}$$

Where, c is the capacity ratio, as given by Equation 21.

$$c = \frac{(\dot{m}c_p)_{min}}{(\dot{m}c_p)_{max}} \tag{21}$$

And $(\dot{m}c_p)_{max}$ is the larger of the heat capacity rates of air and water.

2.3.3. Humidifier

A simple humidifier was chosen, consisting of a horizontal long duct with a rectangular cross section, as shown in Figure 21. In this humidifier, water flows along the base of the channel with a counter airflow above the water surface. Since the humidifier operates at moderate temperatures, this was modelled as an adiabatic system.

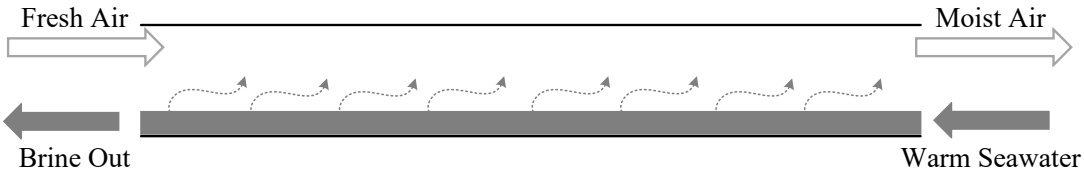

Figure 21. Schematic of a long channel humidifier with rectangular cross-section

The mass and energy conservation as well as the correlations of heat and mass transfer, determine the outlet conditions of both air and water streams. The conservation of energy is given by Equation 22.

$$\dot{m}_{a,hmd}(\hbar_{a,in,hmd-}\hbar_{a,out,hmd}) = \dot{m}_{w,out,hmd}\hbar_{w,out,hmd} - \dot{m}_{w,in,hmd}\hbar_{w,in,hmd} \tag{22}$$

Where, the mass flow rate of discharge water from the humidifier can be calculated from Equation 23.

$$\dot{m}_{w,out,hmd} = \dot{m}_{w,in,hmd} - \dot{m}_{ev} \tag{23}$$

And the rate of evaporation can be computed from Equation 24 [79].

$$\dot{m}_{ev} = j\frac{A_{hmd}}{R_v}\left[\frac{P_{sat,f}}{T_f} - \frac{P_{sat,hmd}}{T_{a,hmd}}\right] \tag{24}$$

The mass transfer coefficient (j), in Equation 24 can be given as a function of the Sherwood number as shown in Equation 25 [78].

$$j = \frac{Sh \times \lambda_{a-w}}{L_{ch}} \tag{25}$$

For flow inside a rectangular duct, the characteristic length is the hydraulic diameter of the duct, and the mass diffusion rate for air-water systems ($\lambda_{a\text{-}w}$) can be determined from Equation 26 [80].

$$\lambda_{a-w} = 1.87 \times 10^{-10} \frac{T^{2.072}}{P} \tag{26}$$

Where, pressure (P) is in atmosphere (atm) and Temperature (T) is in Kelvin (K). In order to determine the Sherwood number, we first need to utilise our understanding of the heat transfer process. In this respect, the total rate of heat transfer between air and water is the summation of convective, evaporative and radiative heat transfer. Due to the system operating at moderate temperatures, the radiative heat transfer can be neglected. The convective and evaporative heat transfer rates can be determined by Equations 27 and 28, respectively.

$$\dot{Q}_{conv} = h_{conv} A_{hmd} (T_{w,in} - T_{a,in}) \tag{27}$$

$$\dot{Q}_{ev} = \dot{m}_{ev} \hbar_{fg} \tag{28}$$

The coefficient of convective heat transfer (h_{cv}) can be determined as a function of the Nusselt number as given in Equation 29.

$$h_{conv} = \frac{Nu \times k_a}{L_{ch}} \tag{29}$$

For the air stream flowing over the water surface, the conditions for an asymmetric heated rectangular channel were considered. Therefore, for the aspect ratio of the model,

under turbulent conditions, the Nusselt number is given by Equations 30 [79] assuming the critical Reynolds number for the flow inside the channel is 2300 [79].

$$Nu = 0.023Re^{0.8}Pr^{1/3} \tag{30}$$

Assuming the HDH desalination system operates at low temperatures and atmospheric pressure, the Chilton-Coburn analogy is applicable for the conditions of this study [79]. Hence the mass transfer coefficient (j), referred to in Equations 24 and 25 can be determined from the analogy given in Equation 31 [81].

$$j = \frac{h_{cv}}{\rho c_p}\left(\frac{Sc}{Pr}\right)^{2/3} \tag{31}$$

Since the heat and mass transfer are analogous, the Sherwood number for turbulent flow conditions can be defined by Equation 32.

$$Sh = 0.023Re^{0.8}Sc^{1/3} \tag{32}$$

2.4. Computational Solution

The intention of this chapter was to model a HDH desalination system, to analyse its yield sensitivity to operational and climatic conditions, and to identify areas of possible improvement. Engineering Equation Solver (EES) [82] was used to determine fluid properties and to solve the sets of equations developed in the previous sections.

To this end, the inputs of the model were the operating parameters such as seawater temperature, ambient air temperature and humidity, air and water flow rates, wind

velocity and total incident radiation. An iterative approach was used to develop the solution for the system, as illustrated in Figure 22. To reach a solution, the model estimated the temperatures of air and water leaving the humidifier, and examined the difference between the estimates of the exiting air and water temperature and the calculated values after the iteration. A solution was achieved when the difference between these was less than 0.01 $°C$.

Equations 13 to 21 are solved for the exit conditions of the condenser and economizer. Subsequently, the model determined the inlet conditions of the humidifier by simultaneously solving Equations 1 to 12 for the exit conditions of the solar water heater.

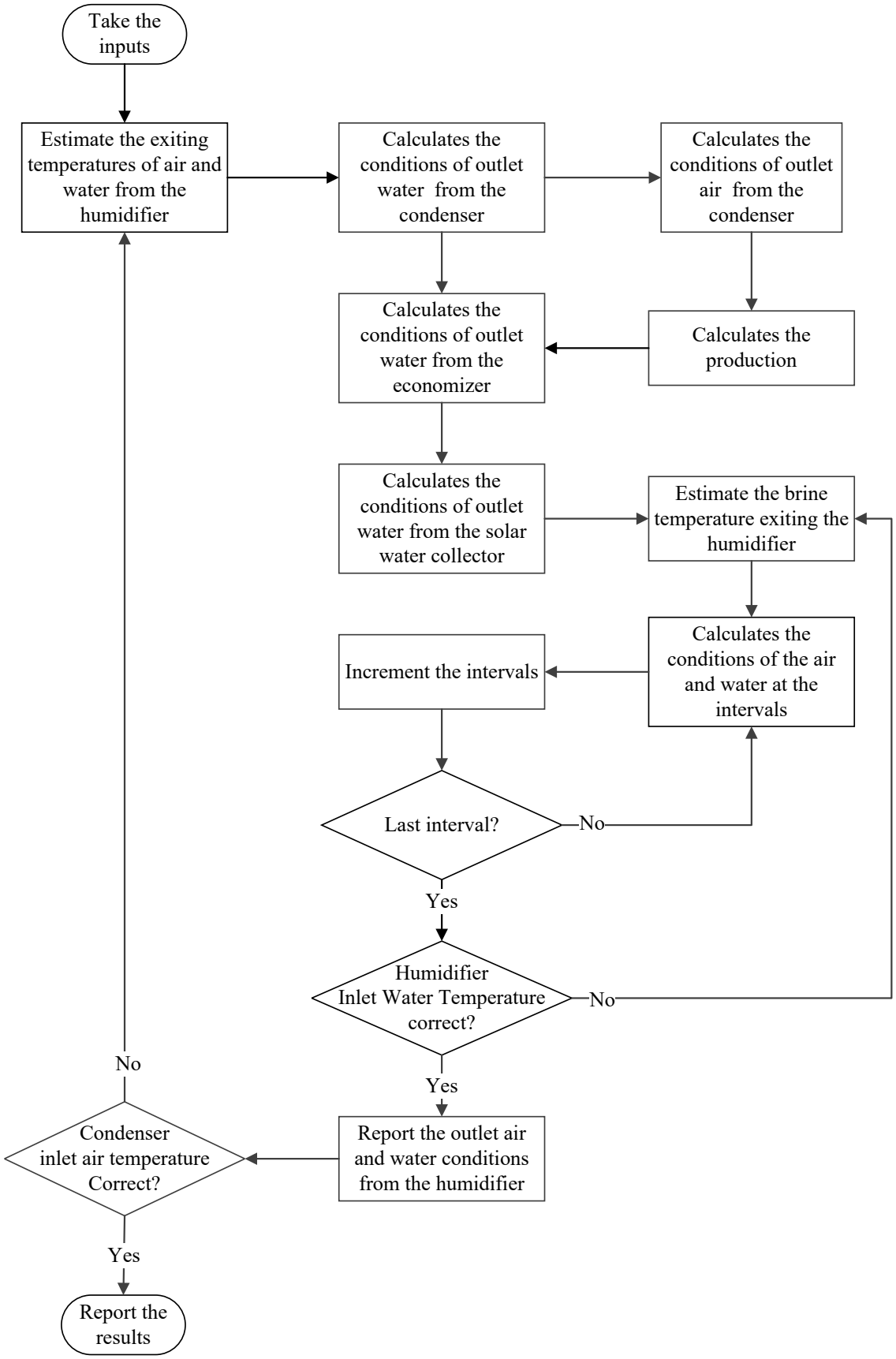

Figure 22. The flow chart diagram of the algorithm used for the model

Inside the humidifier, the heat and mass transfer coefficients vary with vapour pressure and temperature. In order to model this, the humidifier was divided into a series of finite elements, as shown in Figure 23. It was assumed that the conditions were constant within each interval.

An iterative solution was required to determine the outlet air and water conditions from the humidifier. To achieve this, the model first estimated the discharged water temperature to be the wet bulb temperature of the inlet air and then solved Equations 22 to 32 for the exit conditions of each interval. The convergence criteria defined for this iteration was the difference between the temperature of water leaving the solar water collector and the calculated temperature of inlet water to the humidifier, which was taken to be 0.01 $°C$.

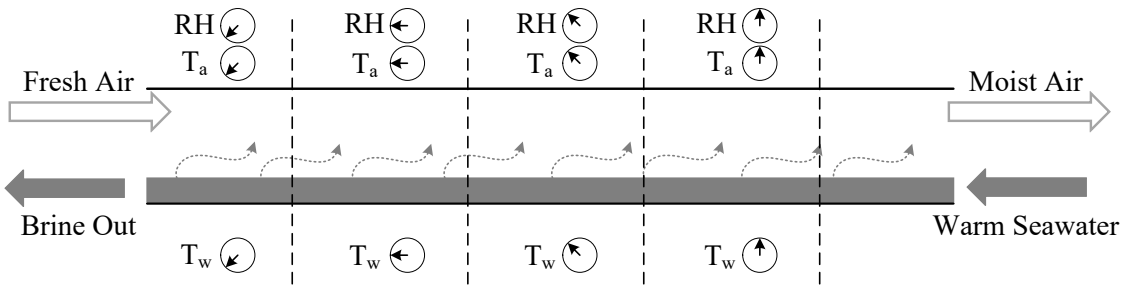

Figure 23. Variation of conditions in each interval along the humidifier

It is obvious that shorter intervals would result in a better accuracy of the calculated results. However, this increases the number of intervals and significantly increases the calculation time. The effect of interval size (and therefore number of intervals) was tested and the result of this analysis is shown in Figure 24. Based on this, it was decided that an interval of $1m$ would yield sufficient accuracy for this work.

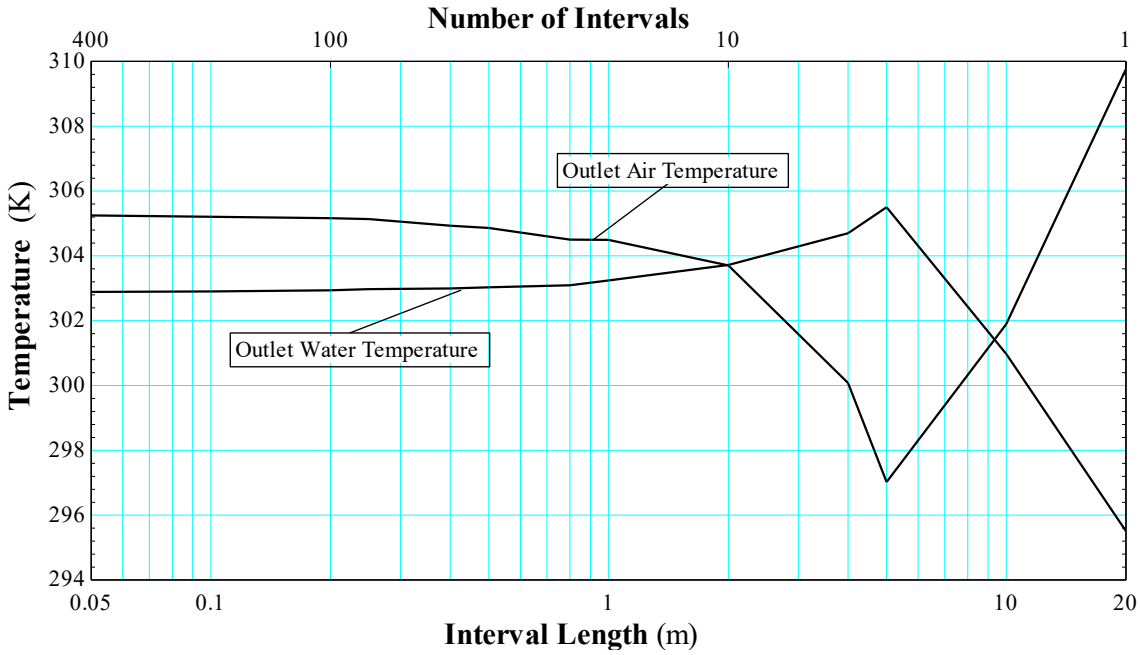

Figure 24. The effect of interval length on the accuracy of the calculated result of the humidifier

2.5. Results of the Model

As the benchmark solution, it was assumed that the HDH model would use two double glazed solar water heaters, providing an absorber area of 4 m^2 to provide the required heat input. The humidifier would provide a total evaporation area of 1 m^2. Two shell and tube heat exchangers, each providing a transfer area of 1.6 m^2, were considered as the dehumidifier and economizer. Further details of the design parameters are shown in Table 1.

Table 1. Design parameters

Water Collector		Humidifier		Condenser		Economizer	
$N_{g,col}$	2 [-]	A_{hmd}	1 [m^2]	$N_{\tau,cond}$	20 [-]	$N_{\tau,econ}$	20 [-]
$N_{\tau,col}$	20 [-]	L_{hmd}	10 [m]	$N_{bf,cond}$	19 [-]	$N_{bf,econ}$	19 [-]
$D_{o,\tau,col}$	0.0127 [m]	W_{hmd}	0.1 [m]	$D_{o,\tau,cond}$	0.0127 [m]	$D_{o,\tau,econ}$	0.0127 [m]
$D_{i,\tau,col}$	0.01181 [m]	H_{hmd}	0.05 [m]	$D_{i,\tau,cond}$	0.01181 [m]	$D_{i,\tau,econ}$	0.01181 [m]

In order to understand how certain parameters affect the performance of the system, a sensitivity analysis was undertaken. The sensitivity of the potable water production to seawater and ambient air temperatures, air and water flow rates, total radiation,

humidification and condensation areas, were evaluated. The range of these variables and their nominal values are given in Table 2.

Table 2. Range and nominal values of the independent variables for sensitivity analysis

Variable	*Unit*	*Range*	*Nominal value*
Humidifier surface area (A_{hmd})	(m^2)	*0.2 to 0.4*	*1*
Condenser surface area (A_{cond})	(m^2)	*0.8 to 2.4*	*1.6*
Air flow rate ($\dot{V}_a$)	(m^3/s)	*0.003 to 0.03*	*0.005 , 0.03*
Water flow rate ($\dot{V}_w$)	(m^3/s)	1.5×10^{-5} *to* 5×10^{-5}	3×10^{-5}
Inlet air temperature ($T_{a,in}$)	($^{\circ}C$)	*10 to 30*	*20*
Inlet water temperature ($T_{w,in}$)	($^{\circ}C$)	*10 to 30*	*15*
Total radiation (G_t)	(W/m^2)	*300 to 1300*	*1000*

As shown in Figure 25, increasing the total radiation linearly increases the yield of the system. Increasing the total radiation results in higher temperature water entering the humidifier and hence leads to more effective humidification in the humidifier.

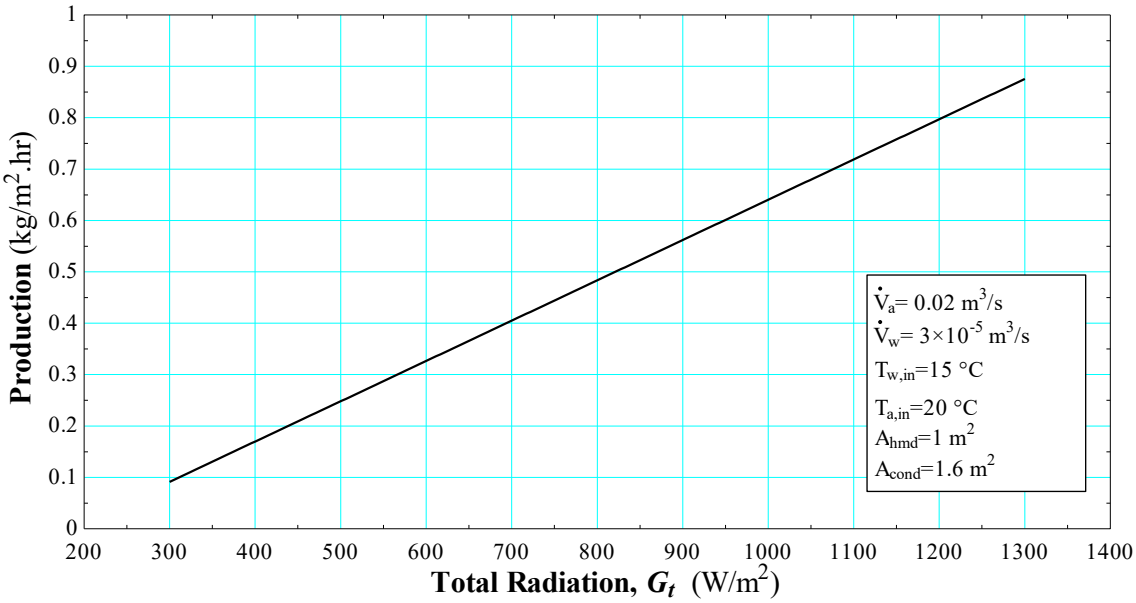

Figure 25. Production rate of potable water vs. total radiation

In Figure 26, the effect of changing inlet seawater temperatures on potable water production is presented. Increasing inlet seawater temperatures increase the total input energy to the system, but the seawater must also condense the moist air from the humidifier. The results show that increasing inlet seawater temperatures decrease the

production rate. Furthermore, higher temperatures of water in the solar collector increase the energy loss to the environment.

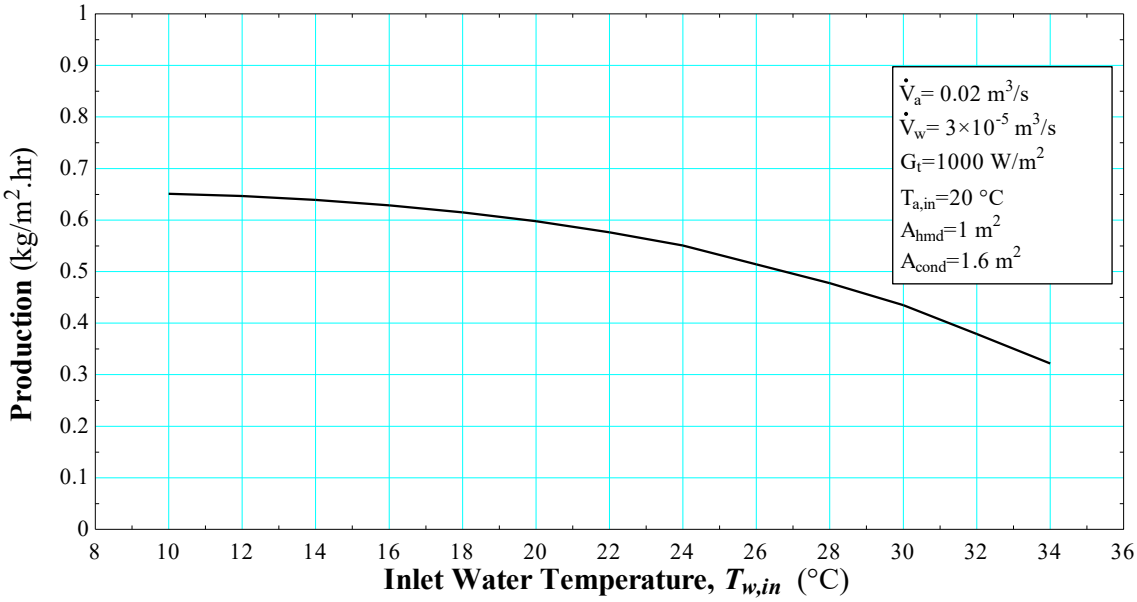

Figure 26. Production rate of potable water vs. inlet water temperature

As shown in Figure 27, increasing the water flow rate decreases the potable water production. This is because a larger quantity of water supplied to the system, reduces the temperature change in the solar collector. Hence, the water enters the humidifier at lower temperatures, and results in less evaporation and thus a lower fresh water production.

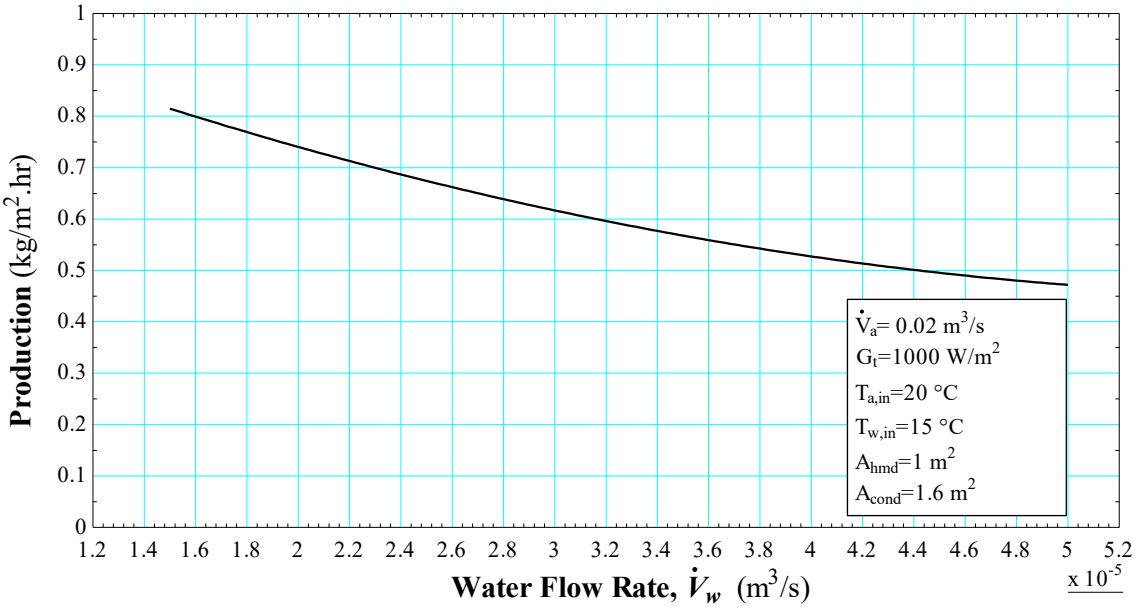

Figure 27. Production rate of potable water vs. volumetric flow rate of water

Sensible heating beyond the saturation condition is expected at higher water temperatures, while for condensation to occur, the overheated air needs to be cooled below its dew point, meaning additional condensation area may be required.

As illustrated in Figure 28, increasing the airflow rate to 0.02 m^3/s results in a significant increase in production, while beyond that the increase in production is not noticeable. This can be explained by the fact that increasing the airflow rate increases the moisture carrying capacity by continuously supplying fresh air, but also reduces the temperature change of air in both the humidifier and condenser. Consequently, by increasing the airflow rate, the moist air temperature drops at the outlet of the humidifier, while the temperature of the exhaust air from the condenser increases. These would eventually reduce the rate of fresh water production.

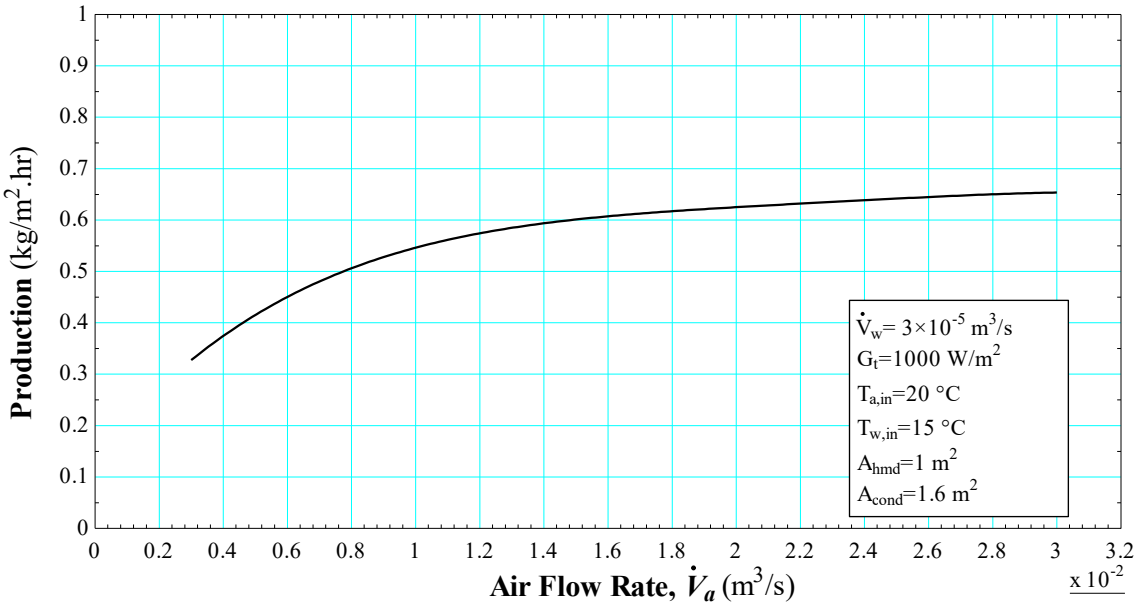

Figure 28. Production rate of potable water vs. volume flow rate of air

Now in Figure 29 it can be seen that with increased ambient air temperatures there is an increase in the potable water production. This is due to the higher moisture carrying capacity of air at higher temperatures, and also due to the sensible heating of the water flow which improves the evaporation process. This sensible heating also increases the

temperature of the discharged water, which is recovered by the inlet water in the economizer. As a result, the temperature of the inlet water to the humidifier is increased, which also increases the rate of evaporation and enhances the production of the system.

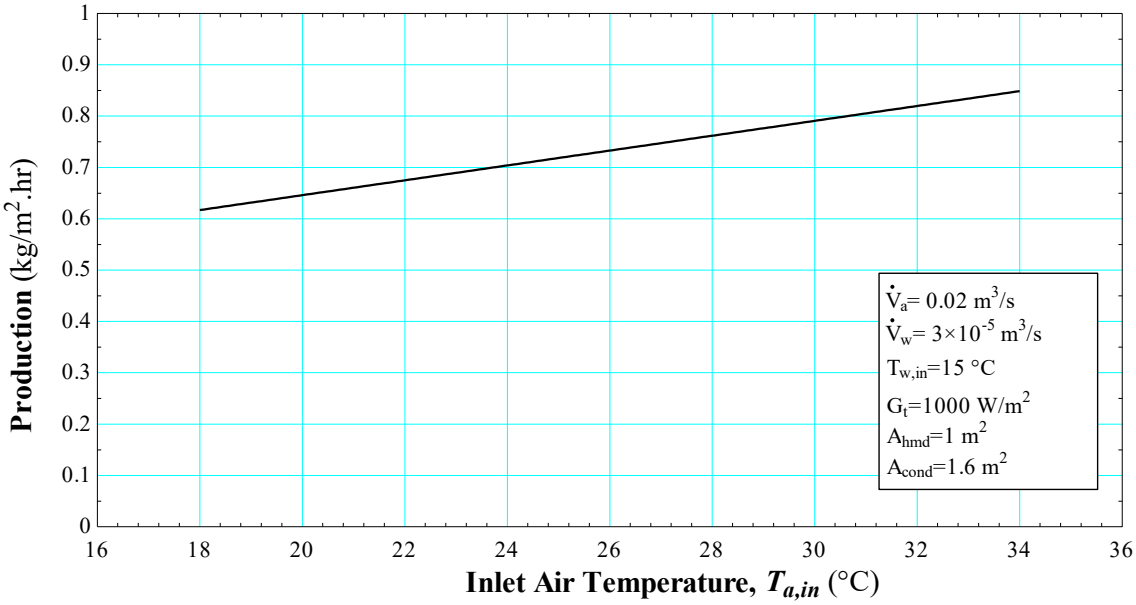

Figure 29. Production rate of potable water vs. ambient air temperature

Previously it was noted that the condenser area could be a significant factor. In Figure 30, it can be seen that increasing the condensation area up to 2 m^2 causes an increase in production of potable water, however, beyond this value there is no significant increase in production. Providing a larger condensation area allows more heat transfer between the water and air streams, but the temperature of the exhaust air from the condenser and consequently the rate of condensation is limited by the condenser inlet water temperature.

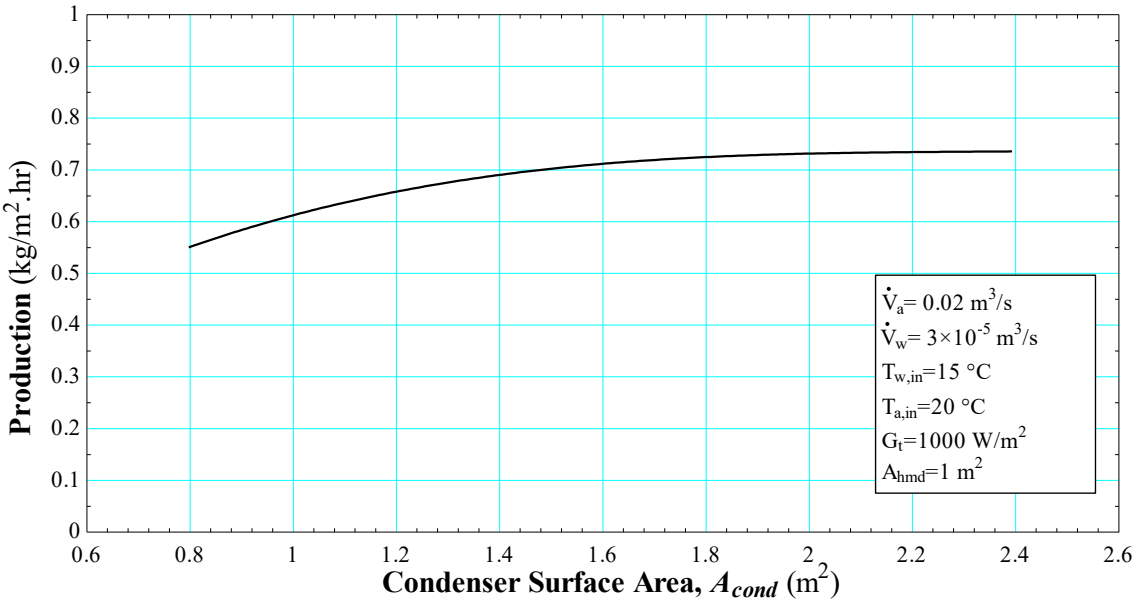

Figure 30. Production rate of potable water vs. condensation area

The effect of humidifier size is shown in Figure 31. Increasing the humidification area to 1.4 m^2 causes a marked increase in production and beyond that value, the production rate increases only slightly. Increasing the area of humidification allows more sensible heating of the air stream by water.

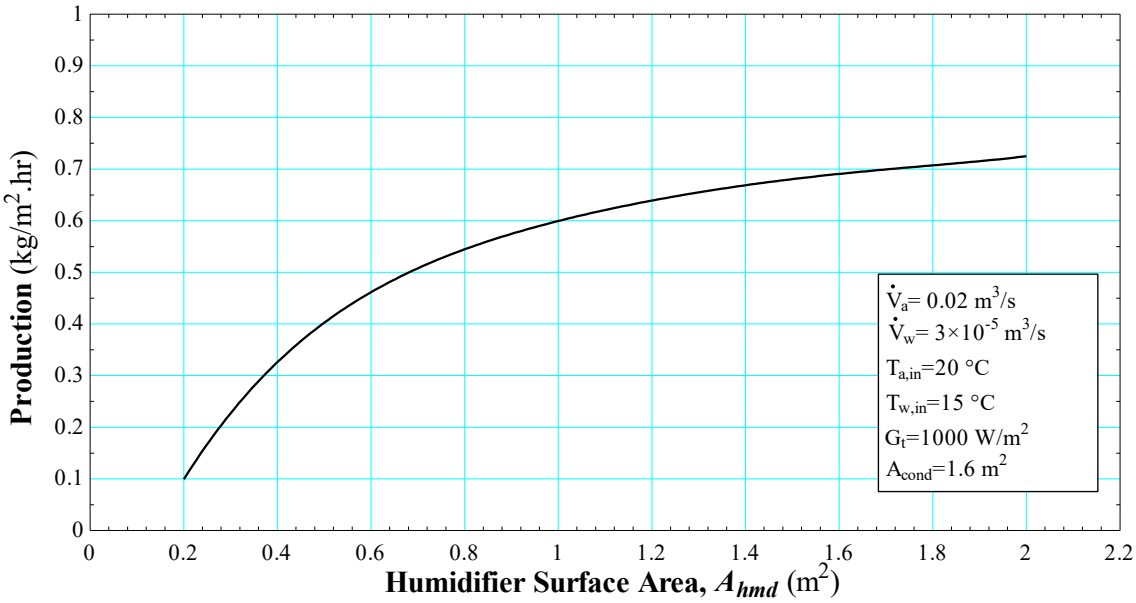

Figure 31. Production rate of potable water vs. evaporation area

This increases the evaporation rate by maintaining the vapour pressure difference between the liquid surface and the bulk stream. The sensible heating however is limited

by the inlet water temperature to the humidifier. Thus, an increase in the humidification area yields diminishing increase in production.

Now for a simple HDH desalination system, a long-channel humidifier is a good solution. However, a large area of humidification is required to achieve a reasonable rate of potable water production. This increases the total size and consequently the cost of the unit. Rather, by improving the heat and mass transfer coefficients, the heating and humidification process and eventually the yield of the system could be enhanced. As shown in Figure 32, for the same humidification areas, if the heat and mass transfer coefficients can be increased by 50% in a hypothetical humidifier, the production of potable water would be significantly increased. This suggests a need to explore ways of achieving such increases to the transfer coefficients.

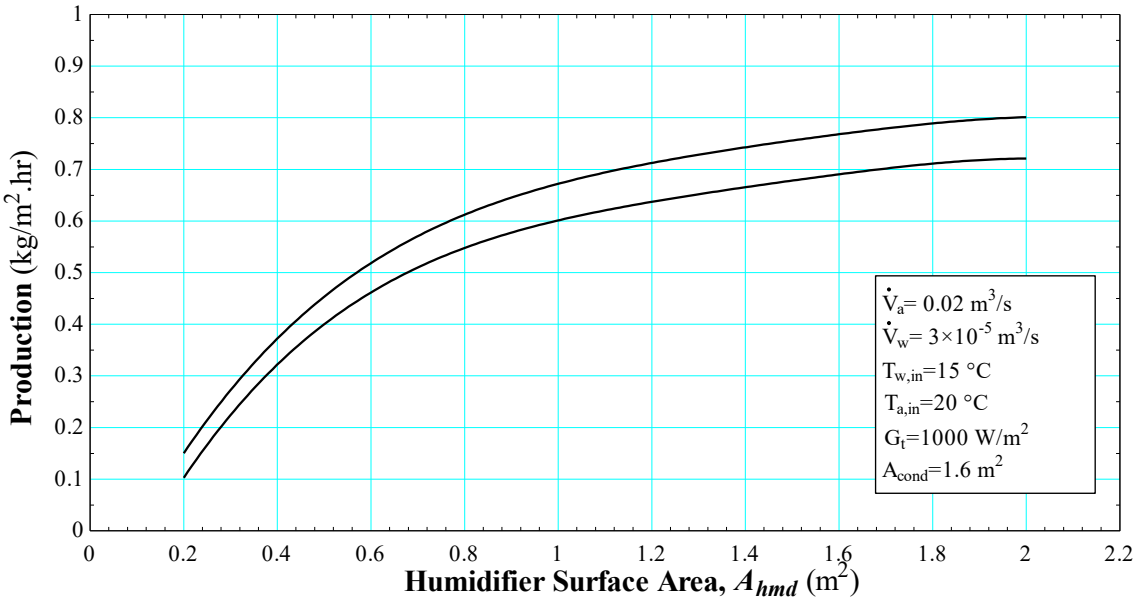

Figure 32. Comparison of HDH production with enhanced heat and mass transfer coefficients

2.6. Chapter Conclusions

In this chapter a simplified model of a solar HDH desalination with a long duct humidifier was developed. The sensitivity of the system water production was evaluated

with respect to climatic conditions and operational parameters. It was shown that higher air and water temperatures in the humidifier as well as increasing the evaporation area and enhancing the heat and mass transfer intensities, improved the heating and humidification process and consequently the system production. On the other hand, increasing the condensation area as well as having lower seawater temperature enhanced the condensation process, which also increased the yield of the system. The results of the model showed that the production rate is mainly influenced by the heating and humidification process rather than the dehumidification process, and in particular the heat and mass transfer in the humidifier.

As such, to develop an efficient solar HDH desalination system the research question posed in Chapter 1 is refined to:

How can one develop a simple humidifier that mixes air and water in an efficient way to enhance the heat and mass transfer phenomena?

Chapter 3 : FALLING WATER SHEETS IN A CROSSFLOW DUCTED AIR STREAM - CHARACTERISING THE FLOW REGIMES

3.1. Introduction

It was shown in the previous chapter that improving the heat and mass transfer processes in the humidifier has the potential to significantly improve the performance of the HDH desalination system. Considering that effective mixing of the liquid and gas streams in heat and mass exchangers increases the intensities of heat and mass transfer, numerous studies have examined the effectiveness of packed beds and spray towers [83-92]. These increase the evaporation area and provide improved mixing of gas and liquid, however, they generally require a considerable power input to blow air through the packing material and to spray water over the humidifier. In HDH systems the water stream is usually warm and salty, which is likely to produce sediment and block the pores of the packed beds or the nozzles of spray towers [70]. The long channel humidifier introduced in Chapter 2 is a good solution for addressing the sedimentation issue. However, due to the lack of effective interaction between the air and water, the intensities of heat and mass transfer are weak. Hence, a humidifier that better mixes air and water with low power input, and is less sensitive to sedimentation needs to be developed.

To address this, it is proposed that the interaction of air and water should occur in a crossflow configuration, where a horizontally ducted airflow crosses through vertical sheets of falling water.

In this regard, a cascading humidifier, shown schematically in Figure 33, where the falling sheets of water are intermittently mixed with horizontally flowing air stream, may significantly improve the transfer phenomena. This would constitute a very simple solution to the requirement and possibly eliminate the sedimentation problem in the humidifier, as any probable sedimentation would occur on the tray surface, which does not influence the heat transfer phenomena. A cascading humidifier similar to this was introduced by Kraft et al [93], to increase the humidification area in a desalination system, but the effects of the falling water were not considered in their study.

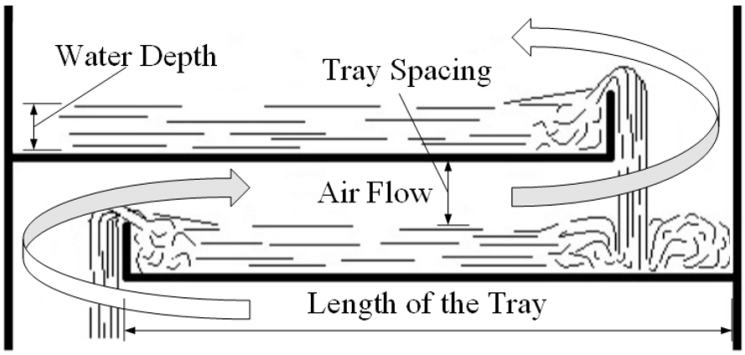

Figure 33. Proposed schematic of a cascading humidifier with crossflow and counter-flow interactions

As seen in Figure 33, two main types of interaction exist in the proposed cascading humidifier; counter-current and crossflow. The counter-current interaction is in fact the same as that in a rectangular duct, which was modelled and discussed in Chapter 2. However, there appears to be very little work done on the crossflow contact of air with a falling sheet of water, which conceptually appears to be a very effective mode of interaction for improving the heat and mass transfer.

Falling liquids in both quiescent and moving gas flows have a variety of different applications including curtain coating, spray and atomization, aeration and gas absorption into liquid media. Numerous studies have examined the behaviour of sheets of falling liquids, without any gaseous crossflow [94-100]. Similarly a number of studies have

examined the behaviour of liquid sheets with gas co-flow and also annular jets in crossflow [101-103]. Bolanos-Jimenez et al. [104] performed a theoretical and experimental study on the behaviour of air and water sheets in a parallel flow situation. They reported a “bubbling” regime that lead to the periodic breakup of the air sheet, and a “jetting” regime, where both sheets evolved slowly downstream without breaking. They suggested that the formation of either of these regimes was dependent on two parameters, namely; the Weber number of the water and the velocity ratio between the air and the water.

Ng et al. [105] performed an experimental investigation on what they termed “bag breakup” of a circular, non-turbulent liquid jet with a gaseous crossflow. They found that as a result of gaseous crossflow a series of column waves would be formed in the jet flow and that the variable wave frequency caused instability. It was reported that the primary breakup processes were due to the aerodynamic effects of the crossflow, regardless of initial disturbances within a liquid jet.

Extending this to liquid sheet flows, Brown [106] investigated the behaviour of a thin sheet of liquid exiting a slot and impinging on a moving solid surface. It was reported that the liquid sheet would be unstable in the region close to the slot unless the liquid velocity outside the slot was greater than $2\ \psi/\dot{m}$, where ψ is the surface tension of the liquid and $\dot{m}$ is the water mass flow rate. It was found that the sheet was stable for Weber numbers greater than unity. Becerra et al. [107] also performed an experimental study on the stability of a viscoelastic liquid sheet and reported that the liquid sheet would be unstable for Weber numbers below 0.94.

Despite the work that has been undertaken on understanding falling liquid sheet flows and circular liquid jets in crossflow, there seem to be no studies that evaluate the

intensities of heat and mass transfer when falling liquid sheets are exposed to a gas crossflow.

Therefore, it was decided to investigate and understand the effect of the crossflow interaction on the intensities of heat and mass transfer with a view to increasing the yield of HDH systems. In doing so, it was expected that various flow regimes would occur when varying the air and water velocities in the system. In other two-phase flows, these flow regimes result in different characteristics of heat and mass transfer and it was considered that this could occur with this combination of flow. This chapter presents the investigation, identification and evaluation of these flow regimes with a view to informing a more in-depth analysis of their heat and mass transfer characteristics.

3.2. Experimental Method: Characterisation of Flow Regimes

An experimental study was developed to characterise the flow behaviour in a crossflow configuration. In these experiments, a sheet of water was injected into a rectangular air channel, as shown in Figure 34. A slotted nozzle, with a width equal to that of the air channel, was used to generate the water sheet as it provided control of the thickness and direction of the sheet. Although this is not a sheet generated by cascading flow over a weir, shown in Figure 33, it provides better experimental control and mirrors the flow interaction. The slotted nozzle was formed by two finely grounded stainless steel plates, providing a uniform thickness of 0.5 *mm* across the jet exit. Stainless steel was chosen due to its low coefficient of thermal expansion ensuring the thickness of the jet could remain reasonably constant over a range of water temperatures. An elevated water reservoir was used to provide a constant pressure head to the jet, where the height of this reservoir was adjustable in order to deliver a range of flow rates. The water flow rate was

determined by measuring the time taken for a known mass of water to pass through the nozzle. To provide the crossflow, air was directed through the duct by a variable speed axial flow fan with a maximum capacity of 280 m^3/hr. The dimensions of the duct were a width of 100 *mm* and a height adjustable between 30 and 100 *mm*. The channel height was adjustable so the effect of fall height on the flow regime could also be assessed. For each test, the airflow rate was determined from measurements made using a pitot static probe traversed across the duct and a differential manometer. The uncertainty associated with the measurements made in the experiment is detailed in Appendix A.

The main intention of this experiment was to examine and characterise the behaviour of the water sheet in a crossflow configuration, and therefore, two cameras (Nikon D300 and Nikon D3300) were used to capture images of the air and water interaction. As seen in Figure 34, the first of these (Camera 1) was mounted to capture a side elevation image while the second (Camera 2) was utilised to capture a profile image of the water sheet.

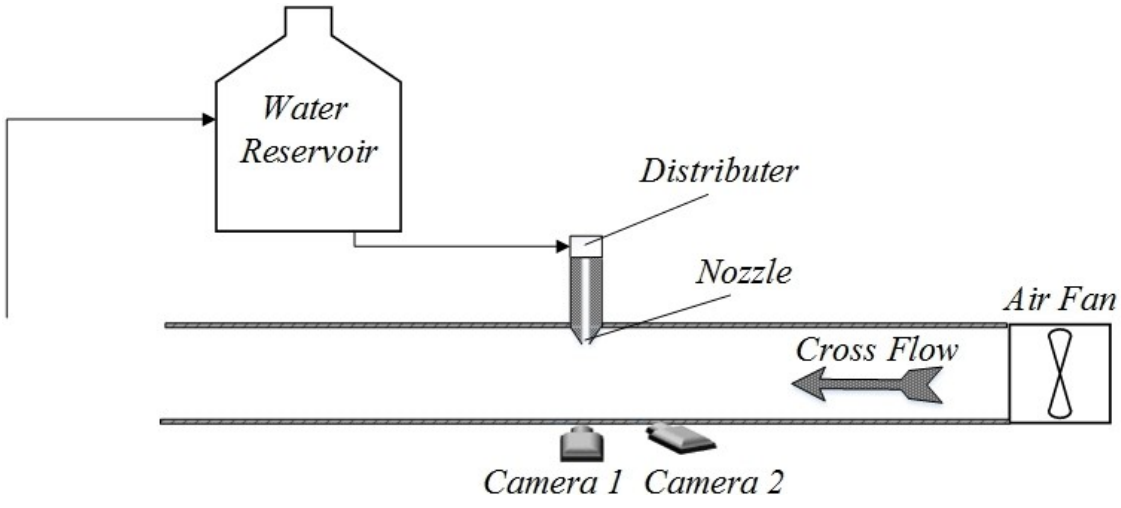

Figure 34. Schematic of the experimental apparatus

In order to understand the behaviour of the water and air interaction, it was decided to investigate the behaviour of falling water by itself. Hence, the experiment was

conducted in two steps; firstly, by variation of water flow rate in the absence of a crossing airflow (quiescent air) and secondly by varying the airflow rates at various water flow rates.

3.3. Results: Water Sheets in Quiescent Air

The behaviour of water sheets when exposed to quiescent air was investigated for two fall heights (36 and 48 *mm*) with the water flow rate varied from 0.75×10^{-5} to 5×10^{-5} m^3/s. This range of flow rates was chosen to demonstrate all the possible flow regimes for a falling flow of water in stagnant air. The properties of water were determined at the average water temperature. The conditions of the experiment are given in Table 3.

Table 3. Experimental conditions for the observation of flow regime in quiescent air

Nozzle width (W_{noz})	(m)	*0.1*
Nozzle thickness (Th_{noz})	(m)	*0.0005*
Water flow rate ($\dot{V}_W$)	(m^3/s)	0.75×10^{-5} *to* 5×10^{-5}
Water temperature (T_w)	($^{\circ}C$)	*15*
Fall height (H_F)	(m)	*0.036 ; 0.048*

It was noted that under these conditions the geometry of the water sheet depended on the water flow rate through the nozzle, as well as the fall height in the channel. Gravity and drag act in the vertical direction, such that, gravity would accelerate the flow while the drag attempts to slow the falling liquid at the walls. Along the width of the nozzle, viscosity influences the velocity profile and surface tension acts to minimize the energy state of the flow.

It was noted that in quiescent air, regardless of the water flow rates, the water sheet was stable. Depending on the fall height and the flow through the nozzle, the stable sheet itself delivered five different geometric forms. In the first instance, as seen in Figure 35a, a liquid sheet was developed in the absence of the airflow by providing a high water flow

rate, thus resulting in a stable sheet that spanned the full width of the duct. As the flow rate was reduced, for a fixed nozzle width and duct height, the flow transitioned through four more regimes, referred to as: ‘trapezoidal’ (Figure 35b, c and d), ‘V sheet’ (Figure 35e), ’Y sheet’ (Figure 35f) and finally ‘finger flow’ (Figure 35g and h). To capture these images a camera (Nikon D3300) was mounted axially along the duct.

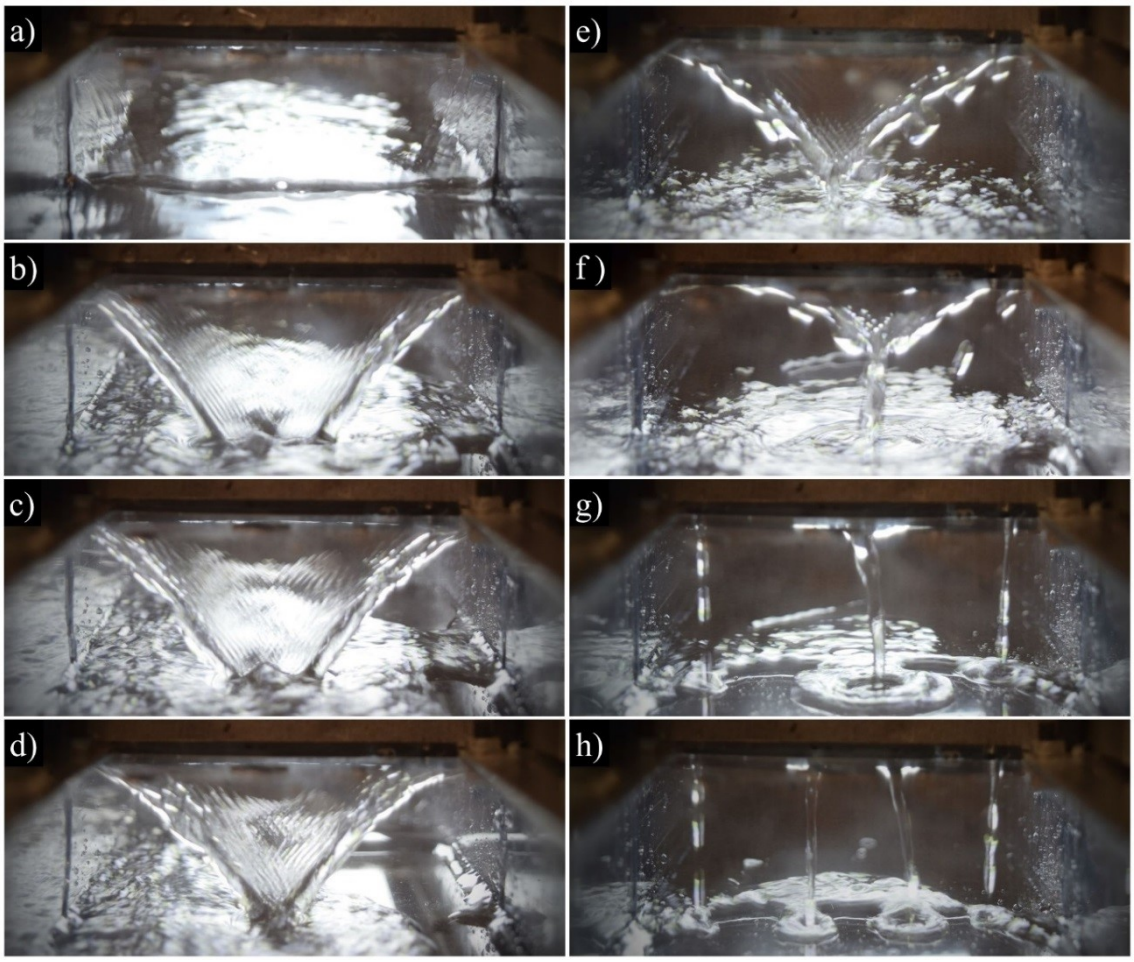

Figure 35. Transformation of the water flow regime from a full width sheet to finger flow (at the fall height of 0.036 m); a) full width sheet ($\dot{V}_w=3.9\times10^{-5}$ m^3/s), b) trapezium sheet ($\dot{V}_w=3.35\times10^{-5}$ m^3/s), c) trapezium sheet ($\dot{V}_w=3\times10^{-5}$ m^3/s), d) trapezium sheet ($\dot{V}_w=2.8\times10^{-5}$ m^3/s), e) V sheet ($\dot{V}_w=2.4\times10^{-5}$ m^3/s), f) Y sheet ($\dot{V}_w=2\times10^{-5}$ m^3/s), g) finger flow ($\dot{V}_w=1.2\times10^{-5}$ m^3/s), h) finger flow ($\dot{V}_w=0.75\times10^{-5}$ m^3/s)

Considering the flow regimes in Figure 35, it is clear that at high flow rates inertia of the liquid dominates the flow formation. For these conditions, the higher velocity of liquid at the jet exit gives rise to sufficient inertia to hold the edges of the sheet to the walls of the channel. At this point adhesion forces, between the liquid and the wall, act to

"attach" the flow to the walls. As such, the boundaries of the wall, the fixed nozzle width and the duct height, constrain the flow to a sheet spanning the full width of the duct.

However, as the flow decreases (or the duct height increased at a fixed flow rate) the ability of the flow to remain attached to the wall and maintain continuity becomes more difficult, particularly as the sheet "thins" due to reducing the water flow rate. As continuity must be maintained *and* the adhesion forces at the wall are relatively weak, they are eventually overtaken by the surface tension acting to minimise the perimeter of the cross section. This eventually results in the detachment of the flow from the wall and gives rise to a 'trapezoidal' regime, as illustrated in Figure 36.

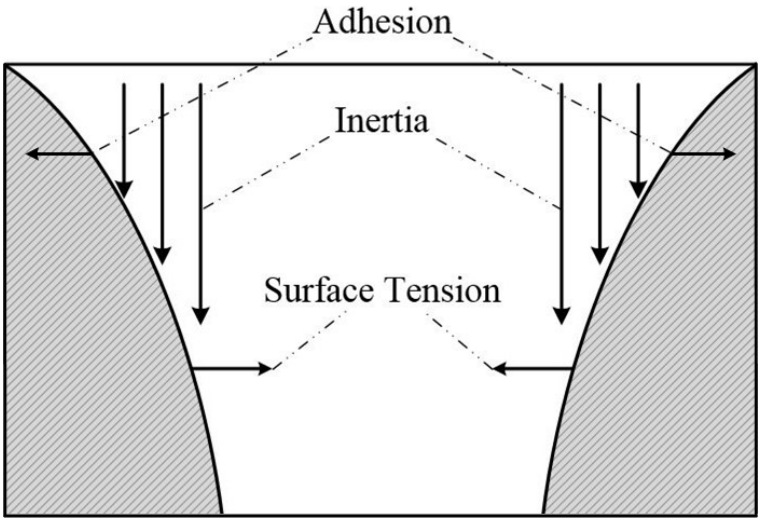

Figure 36. Forces acting on the falling liquid

Decreasing the water velocity even further continues to reduce the momentum relative to the surface tension and consequently the sheet width decreases until the edges of the sheet meet at the bottom of the duct. This leads firstly to a V shaped sheet and eventually a Y shape sheet, in which the edges of the sheet meet before the water lands on the bottom of the duct.

Further decreasing the water velocity, the sheet begins to breakup and forms parallel fingers along the width of the nozzle. This again can be explained by the flow maintaining

continuity, with the surface tension attempting to minimise the perimeter of the surface area. Figure 37 illustrates this, showing that at low water velocities surface tension divides the flow into multiple streams. This results in a so-called ‘finger flow‘ regime leaving the nozzle, with dry spots along its length. This flow behaviour was previously studied by Marston et al. [99].

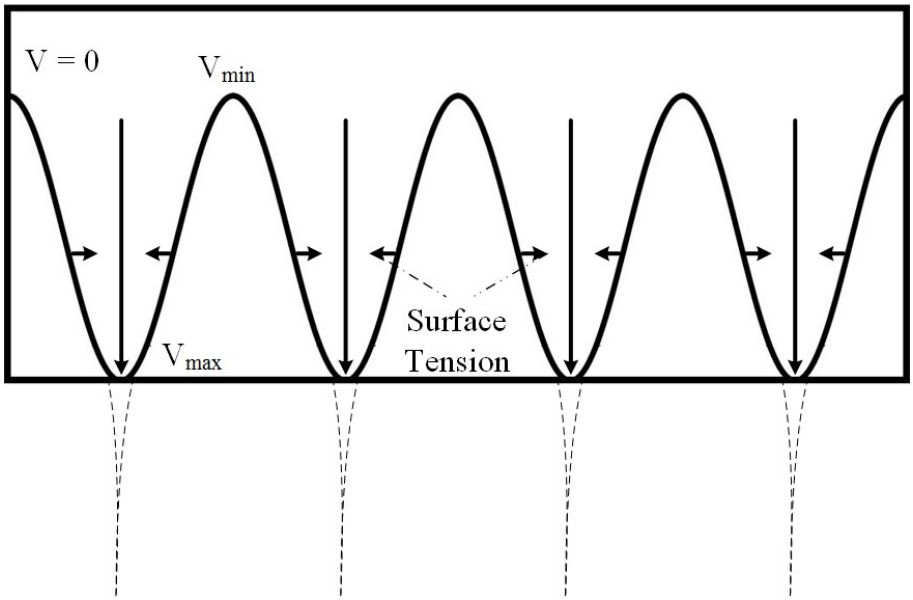

Figure 37. Velocity profile inside the slot

3.4. Results: Water Sheets with Air Crossflow

The behaviour of falling sheets of water in a crossflow configuration was studied at various flow rates (2×10^{-5} to 5×10^{-5} m^3/s) in a range of airflow rates (0.42×10^{-2} to 2×10^{-2} m^3/s). The effect of increasing the fall height from 0.036 *m* to 0.048 *m* was also evaluated. During this series of tests, the same nozzle dimensions were used as in the tests performed with quiescent air. Table 4 shows the experimental conditions.

Table 4. Experimental conditions for the observation of water sheets in air crossflow

Nozzle width	(*m*)	*0.1*
Nozzle thickness	(*m*)	*0.0005*
Water flow rate	(m^3/s)	2×10^{-5} *to* 5×10^{-5}
Air flow rate	(m^3/s)	0.42×10^{-2} *to* 2×10^{-2}
Water temperature	(°*C*)	*15*
Air temperature	(°*C*)	*20*
Air humidity	(-)	*0.50*
Fall height	(*m*)	*0.036 ; 0.048*

By altering the water flow rate, at various airflow rates, four different modes of interaction were found for the conditions tested, as shown in Figure 38. A ’Broken sheet’, shown in Figure 38 (a-b), was formed at higher flow rates of air and low flow rates of water. At lower airflow rates, regardless of water flow rate, the water sheet was observed to be ‘stable’ as seen in Figure 38 (c-d). High flow rates of air and water resulted in formation of a ‘flapping sheet’, shown in Figure 38 (e-f). Further increasing the airflow at higher flow rates of water caused a ‘stable lifted sheet’ to form, as shown in Figure 38 (g-h).

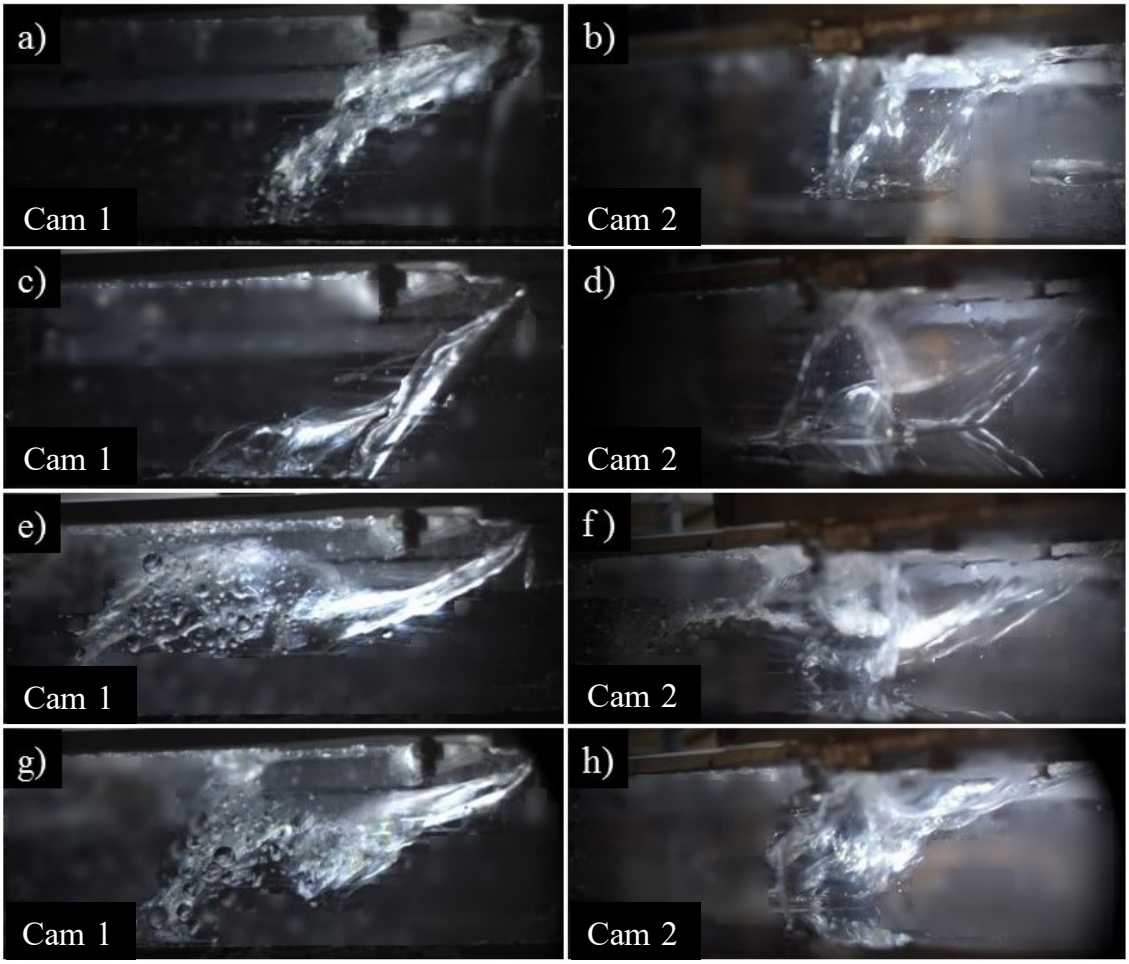

Figure 38. Water flow regime in air crossflow; a and b) broken sheet ($\dot{V}_w=2.4\times10^{-5}$ m^3/s and $\dot{V}_a=0.9\times10^{2}$ m^3/s); c and d) stable sheet ($\dot{V}_w=3.9\times10^{-5}$ m^3/s and $\dot{V}_a=0.71\times10^{2}$ m^3/s); e and f) flapping sheet ($\dot{V}_w=3.9\times10^{-5}$ m^3/s and $\dot{V}_a=0.9\times10^{2}$ m^3/s); g and h) broken sheet ($\dot{V}_w=5\times10^{-5}$ m^3/s and $\dot{V}_a=1.8\times10^{2}$ m^3/s);

Introducing an air crossflow into the channel leads to a pressure difference across the sheet, as well as aerodynamic drag forces, that depend on the velocity of the air stream and the area of the water sheet. The pressure difference across the sheet causes the sheet to bow, pushing out the centre and dragging in the sides. Also, depending on the blockage ratio (the ratio of the sheet area to the cross-sectional area of the channel) a portion of the air passes by the sheet with no significant effect on the water flow regime as illustrated in Figure 39.

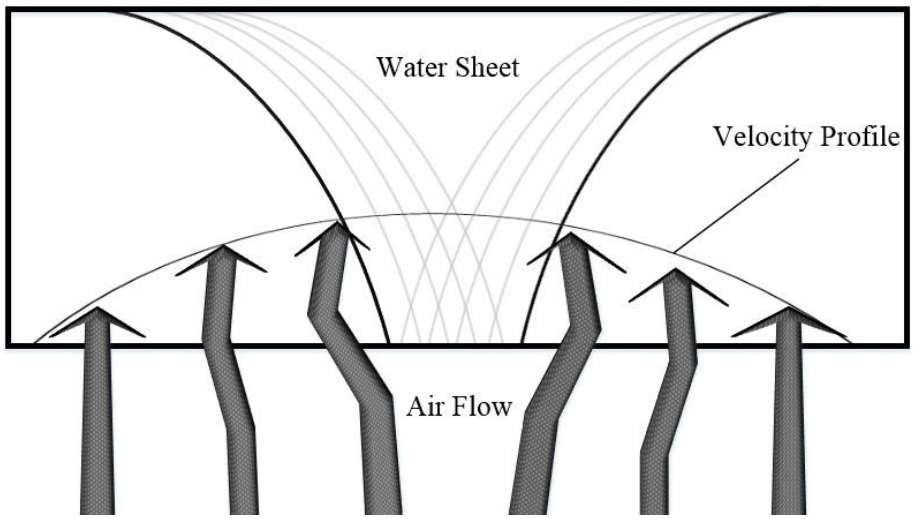

Figure 39. Behaviour of airflow in contact with a relatively small water sheet

Increasing the airflow increases the drag forces and this holds the water sheet at an angle to the horizontal. The inertia and weight of water on the other hand, attempts to "hold" the flow vertical. However, increasing the water flow increases the area and mass of the water sheet and as a result increases the weight and drag forces acting on the water sheet. Within the water sheet, the surface tension attempts to hold the sheet together, however once the drag forces dominate the internal cohesion, the water sheet breaks. It was found that if the velocity distribution in the sheet and hence the thickness of the water sheet was uniform, the sheet breaks up at the tail end of the sheet, as illustrated in Figure 38(e-f). Alternatively, as demonstrated in Figure 38(a-b), if the velocity profile is not uniform it breaks up vertically. In the following sections, the observed modes are discussed in detail.

3.4.1. Stable Sheet

Depending on the fall height and the velocity of water at the nozzle, the geometry of the stable sheets was seen to be a 'Y', triangular or trapezoidal shape, as long as the air was not strong enough to break up or flap the water sheet. At relatively low water flow rates and higher fall heights, the edges of the sheet meet each other above the bottom of

the channel creating a Y sheet, as seen in Figure 35f. By increasing the air crossflow on a stable sheet, the drag due to the air initially inclines the falling water sheet and creates a concave arch in the middle of the sheet. Further increasing the airflow under these conditions increases the concavity of the arch. Figure 40 illustrates this point by showing a stable Y sheet.

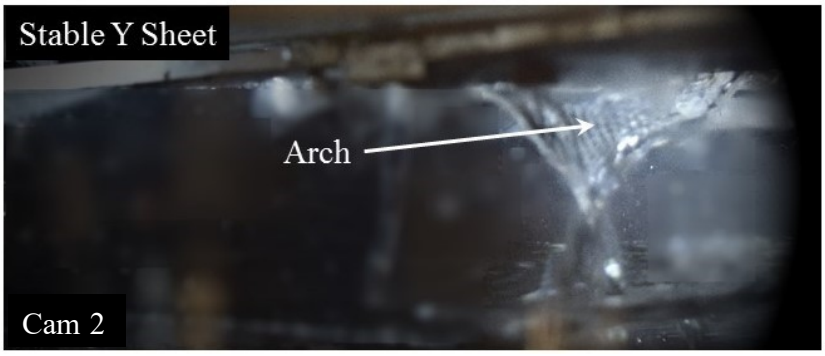

Figure 40. Stable Y Sheet ($\dot{V}_w=2\times10^{-5}$ m^3/s and $\dot{V}_a=0.42\times10^{2}$ m^3/s)

Increasing the water jet velocity increases the inertia of the water stream, which increases the sheet area, by holding the edges of the sheet away from the centre. Increasing the exiting water velocity also increases the momentum of the water stream, which pushes the arch down towards the bottom of air tunnel. At reasonably high momenta of the water stream, where the sheet is strong, the arch will turn into a water tunnel. The position of the arch at different water flow rates with constant airflow rate, and the transformation to water tunnel, are illustrated in Figure 41-a to 41-f. As a consequence of the small blockage ratio in Y sheets, the drag forces on these sheets are relatively small and therefore higher airflow rates are required to break up the sheet.

However, the larger blockage ratio for triangular and trapezium geometries results in higher drag forces. Therefore, at higher water velocities the sheet will change its mode with lower flow rates of air in the duct. In this respect, the inclination angle of the sheet depends on the blockage ratio and the drag force, so that at smaller blockage ratios the

inclination angle is smaller. On the other hand, increasing the water velocity increases the momentum of water in the vertical direction, which attempts to reduce the inclination angle. Counter to this, increasing the air velocity in the duct has the effect of thinning the sheet due to the drag, thereby increasing the size of the concave arch until it eventually breaks up or moves to a flapping mode.

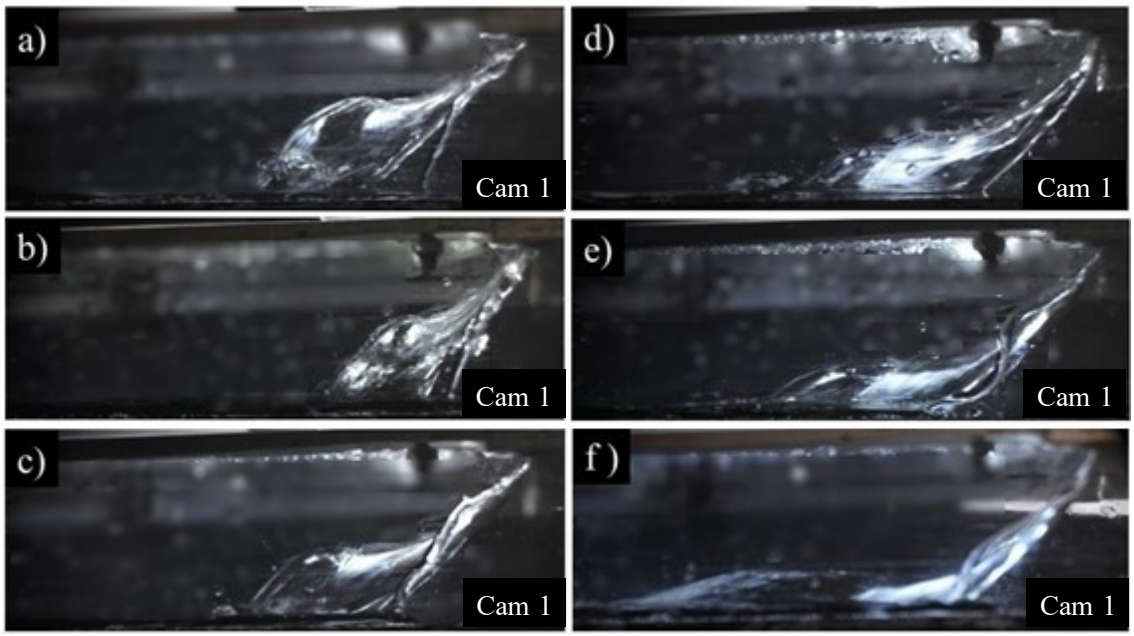

Figure 41. Position and shape of the arch at increased water flow rate and constant airflow of 0.9×10^{2} m^3/s at a fall height of 0.036 m; a) $\dot{V}_w=3\times10^{-5}$ m^3/s, b) $\dot{V}_w=3.35\times10^{-5}$ m^3/s, c) $\dot{V}_w=3.9\times10^{-5}$ m^3/s, d) $\dot{V}_w=4.35\times10^{-5}$ m^3/s, e) $\dot{V}_w=4.74\times10^{-5}$ m^3/s, f) $\dot{V}_w=5\times10^{-5}$ m^3/s

3.4.2. Broken Sheet

Broken sheets can be generated from either flapping or stable sheets by either increasing the air velocity at low water flow rates or reducing the water flow at high airflow rates. Due to the wall effects, the velocity of air is higher at the centre causing a shear stress across the sheet. At the same time, at lower water flow rates thinning occurs closer to the jet exit. Hence, once the sheet is relatively thin and the shear stress due to the airflow is strong enough to overcome the surface tension and inertia of the water

stream, the sheet will break up vertically into fingers or smaller sheets, as shown in Figure 42 (a-f).

After break up, surface tension acts to pull the edges of these disjointed flows towards their centres, in order to minimise the surface area of the water sheet. This eventually thickens each individual flow to form the fingers, which reduce the contact area between the air and water sheet. As a consequence, the drag force on the water flow will be smaller and result in a smaller inclination angle.

By further increasing the airflow at a fixed water flow rate or decreasing the water flow at a fixed airflow rate, the fingers will break into droplets. This can be explained by the water flow accelerating in an inclined direction as a result of the gravitational and drag forces. As the water accelerates, the cross section of the water fingers decreases due to continuity and eventually, surface tension will break the fingers into droplets in order to bring the water flow into its minimum energy state.

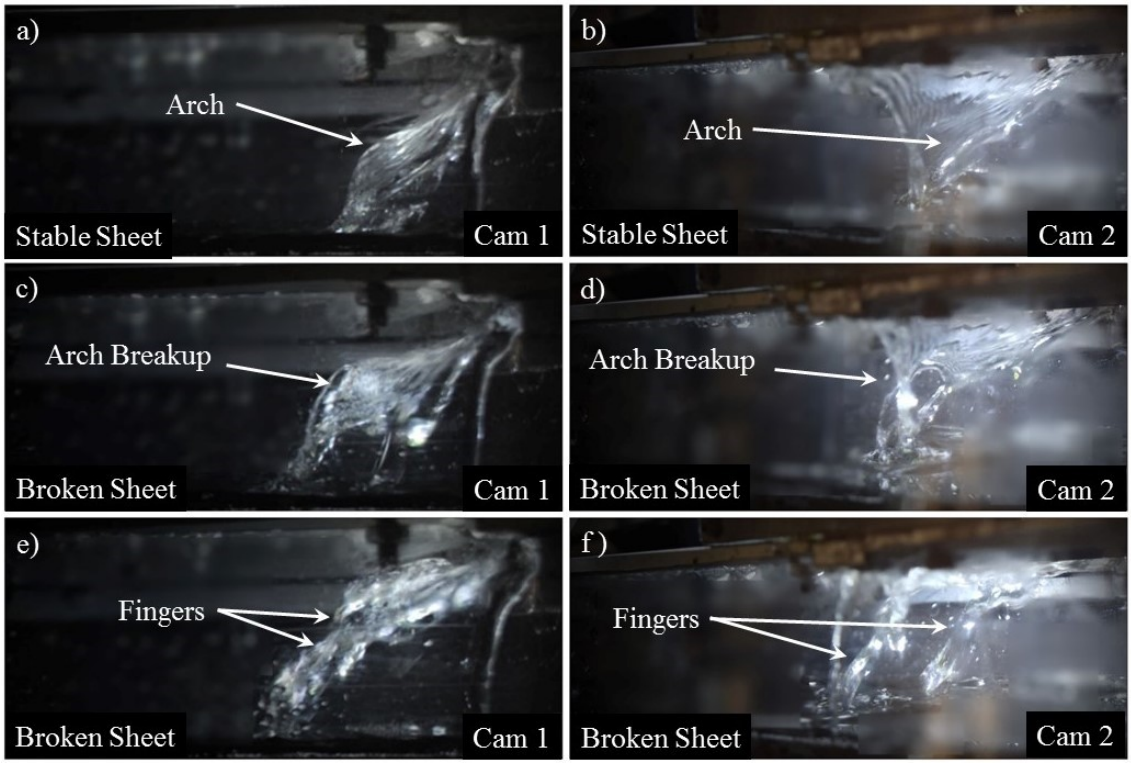

Figure 42. Break up of a triangular sheet into fingers at a constant water flow ($\dot{V}_w=2.4\times10^{-5}$ m^3/s) by increasing the airflow; a and b) $\dot{V}_a=0.41\times10^{-2}$ m^3/s, c and d) $\dot{V}_a=0.7\times10^{-2}$ m^3/s, e and f) $\dot{V}_a=1.21\times10^{-2}$ m^3/s

3.4.3. Flapping and Stable Lifted Sheets

Once the velocity of the water stream at the nozzle is high enough, such that the sheet thins only slightly as it falls, the sheet tends to resist breaking vertically. Under these conditions, if there is sufficient momentum in the air stream, the pressure difference across the sheet is able to lift the sheet as a whole, as illustrated in Figure 43 and Figure 44. Once the sheet is lifted, the tail end of the sheet breaks into droplets, due to the continued acceleration of the water in the near horizontal plane. The lifting of the sheet, unblocks the channel and thus reduces the pressure drop across the sheet, hence, due to gravitational forces, the sheet falls back across the channel and repeats the process. This oscillation, named here as a ‘flapping sheet’, shown in Figure 44 (c-d), has the added

effect of intermittently breaking off the tail of the sheet as it is flicked from the near vertical to horizontal position.

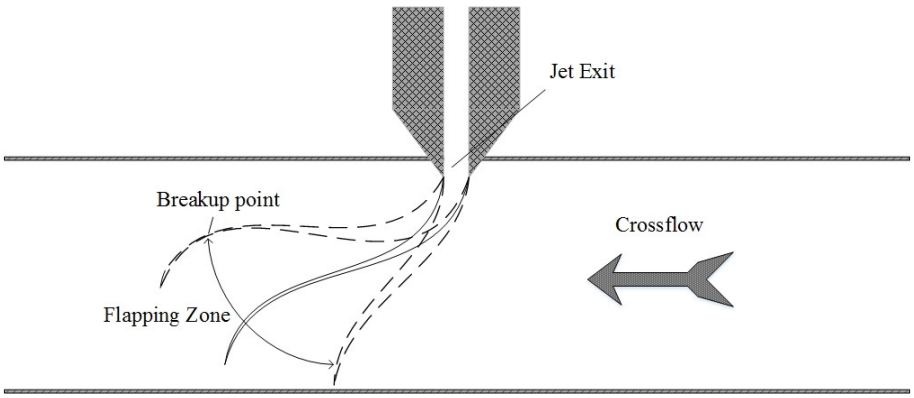

Figure 43. Diagram of the flapping sheet

The flapping zone illustrated in Figure 43 can be further enlarged by increasing either the air or the water velocities. At high enough air velocities, there is sufficient momentum in the air to balance the gravity and hold the sheet with an inclination angle such that the flapping ceases. As expected, the inclination of the sheet was higher with greater airflows. At these conditions, the airflow pushes the edges of the water flow towards the centre of the air channel. Hence, this mode is referred to as a 'stable lifted sheet'. Figure 44 (a-f) shows the transformation of the stable sheet (a-b) to flapping sheet (c-d), and finally to a stable lifted sheet (e-f) at a constant water flow by altering the airflow rate.

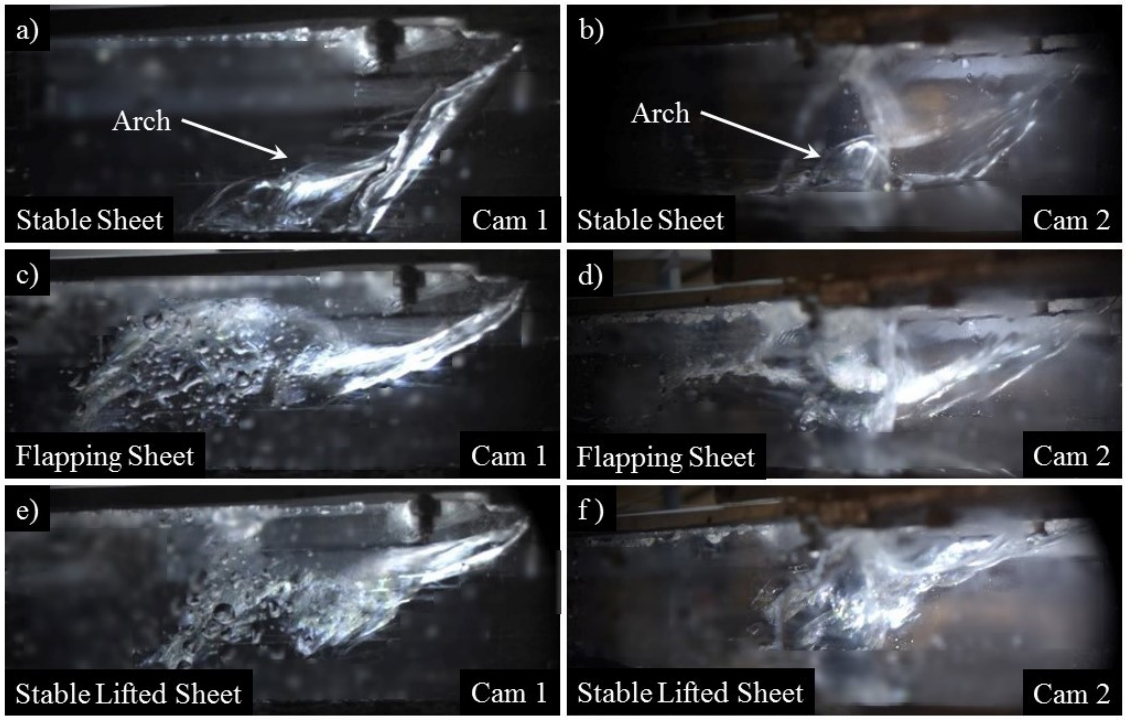

Figure 44. Transformation of the flow regime from stable sheet to flapping sheet and to stable merged flow at the water flow rate of $\dot{V}_w=3.9\times10^{-5}$ m^3/s and fall height of 0.036 m; a and b) $\dot{V}_a=0.5\times10^{-2}$ m^3/s, c and d) $\dot{V}_a=0.92\times10^{-2}$ m^3/s, e and f) $\dot{V}_a=1.8\times10^{-2}$ m^3/s

3.4.4. Mapping the Flow Regimes

Flow regime maps are graphical tools to define the boundaries between different types of flow regimes in a specific system. These are based on the parameters that best describe the system. Many types of flow regime maps have been proposed for various geometries and conditions [108-111]. When describing a falling liquid in stagnant gas, the Weber number, defined as the ratio of inertia to surface tension, is often used to characterise the flow [104, 106, 107]. Considering the gas flow, Reynolds number, defined as the ratio of inertia and viscous forces, is commonly used to describe the characteristics of gas flow in a channel [79].

When a horizontal ducted airflow interacts with falling sheets of water, the characteristics of the water sheet can be described by its Weber number, and the response of the sheet to airflow can be represented by the Reynolds number of the airflow.

Therefore, it was decided to map the flow regimes according to the Weber number of the water, shown in Equation 33, and the Reynolds number of air, given in Equation 34.

$$We_w = \frac{\rho_w {V_{ch,w}}^2 L_{ch,w}}{\psi} = \frac{\rho_w V_{ch,w} Q_w}{2\psi} \tag{33}$$

$$Re_a = \frac{\rho_a V_{ch,a} L_{ch,a}}{\mu_a} \tag{34}$$

In order to accommodate the effects of gravity and fall height, the characteristic velocity of water was taken to be that of water as it lands on the bottom of the channel in stagnant air. This was not measured directly but can be estimated using the Bernoulli equation, as shown in Equation 35. The landing velocity was also used to determine the Weber number by Kyotoh et al. [100].

$$V_{ch,w} = \sqrt{{V_{m,w}}^2 + 2gH_F} \tag{35}$$

Knowing the water flow rate and the cross-sectional area of the nozzle, the mean velocity of water at the nozzle ($V_{m,w}$) can be determined. The characteristic length of a water sheet for the "flow" Weber number has previously been chosen to be half the thickness of the water sheet at the nozzle exit [97], whereas, in this study, in order to accommodate the effects of fall height, the "local" Weber number was considered. For this, the sheet thickness at the bottom of the channel was determined, assuming that there is no crossing airflow and the water sheet spanned the full width of the duct. Half of this thickness, as shown in Equation 36, is taken to be the characteristic length as used in the literature [97].

$$L_{ch,w} = \frac{A_{loc,w}}{2W_{noz}} \tag{36}$$

The shape and extent of the sheet of the falling water influences the Reynold's number of the air crossflow, by its effect on the cross-sectional area of the air stream. As such, higher water flow rates result in larger blockage ratios, which consequently increases the velocity of air by reducing the cross sectional area. Therefore, in the determination of the Reynolds number, the average velocity was considered to be a characteristic velocity as defined in Equation 37.

$$V_{ch,a} = V_{m,a} - V_R \tag{37}$$

Where, the resultant velocity (V_R) is given by Equation 38.

$$V_{\mathrm{R}} = \frac{\dot{m}_a V_{m,a}}{\dot{m}_a + \dot{m}_w} \tag{38}$$

In order to accommodate the influence of fall height and channel width simultaneously on the Reynolds number, the characteristic length ($L_{ch,a}$) of the gas stream in Equation 34, was chosen to be the diagonal of the duct.

A series of experiments were performed in order to characterise and map the different flow regimes in a crossflow interaction of ducted air with falling sheets of water. In these tests, the airflow rate was varied to provide a range of Reynolds numbers between 5000 and 25000, and the water flow rate was changed to provide a variety of Weber numbers from 1.5 to 7. This would more than cover the range of conditions expected in a cascading humidifier.

Figure 45, illustrates the flow regime map based on the Reynolds number of air and the Weber number of water as described.

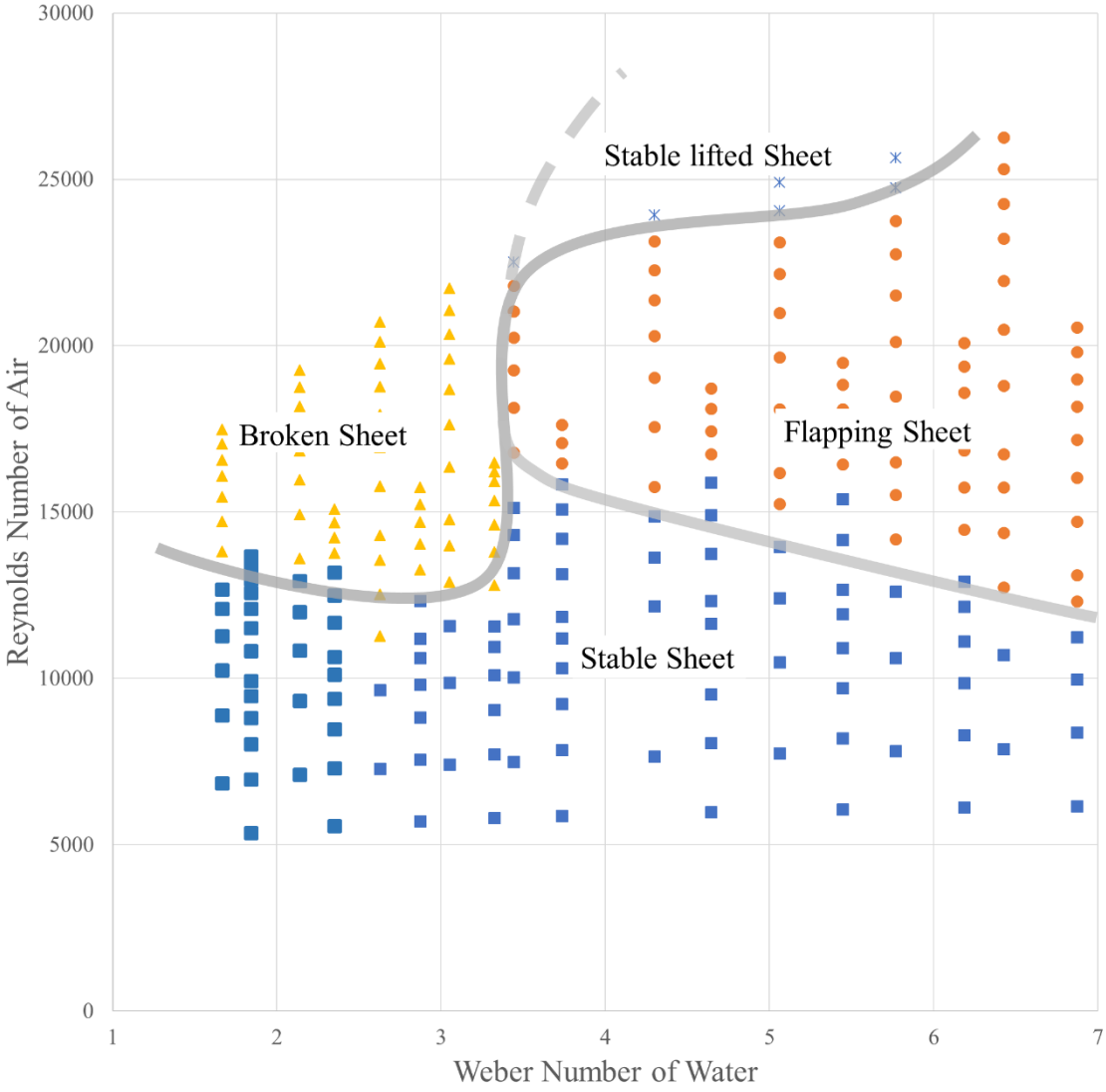

Figure 45. Flow regime map for air and water crossflow interaction based on the Reynolds number of air and the Weber number of water.

It was observed that for the entire range of examined Weber numbers and at lower Reynolds number, the sheet of water was stable. The critical Reynolds number for 'stable sheets' was seen to be around 12500 beyond which, depending on the Weber number of water, the stable sheet was transformed to either a 'broken sheet' or 'flapping sheet'. In the range examined, the critical Weber number was seen to be around 3.5, below this value the flow regime was found to be 'broken', and beyond that the 'flapping sheet' was observed. A second critical Reynolds number of approximately 22500 was also observed, beyond which the 'flapping sheet' was transformed to a 'stable lifted sheet'.

3.4.5. Discussion of the Experiments

In considering the flow regimes and their implications on the transfer phenomena, there are a number of conclusions that can be drawn. Firstly, under the circumstances of a ‘stable sheet’, inertia in the liquid tends to dominate the flow behaviour, which prevents the mixing of air and water, and so the transfer area is limited to the area of the liquid sheet. Poor coefficients of heat and mass transfer could be expected for this flow regime, due to the lack of interaction between air and water.

Secondly, in the ‘broken sheet’ regime, air inertia dominates the flow behaviour, which provides a relatively large transfer area by breaking the sheet of water to droplets. This flow regime was observed at high Reynolds numbers, which enhances the turbulence of the bulk stream and may lead to improvements to the transfer processes. However, the gas flow had less interaction with the liquid sheet due to the large amount of air able to bypass the water sheet.

Thirdly, in a ‘flapping sheet’, the flow behaviour changes repeatedly, with intermittent domination of the inertia of air and water, which provides a well-mixed flow that one may expect to strongly assist in the transfer process. This flow regime provides a large transfer area by breaking the tail end of the sheet into droplets as it flicks in the near horizontal position.

Finally, for a ‘stable lifted sheet’, the inertia of air dominates the behaviour of the flow by holding the sheet at a stable angle. This would reduce the mixing of the two streams but due to continuous acceleration along the horizontal plane, the tail end of the sheets breaks into droplets, which provides a relatively large transfer area. Furthermore, in this flow regime, both velocities are high, which is likely to enhance the transfer

processes. Based on these observations, it is highly probable that among the different modes of interaction, the ‘flapping sheet’ and the ‘stable lifted sheet’ would provide the highest heat and mass transfer coefficients.

3.5. Conclusions of the Experiments

A series of experiments on the behaviour of falling sheets of water in a crossflow ducted air stream was performed in order to identify and map the different flow regimes.

In order to develop an understanding of the phenomena, the behaviour of falling water in quiescent air was initially investigated. It was found that for the constant nozzle dimensions and depending on the water flow rate and the fall height, five modes of falling water can be formed, namely; rectangular, trapezoidal, V shape, Y shape and finger flows. These flow regimes were detailed with respect to the inertia of the falling water as well as the cohesion and adhesion forces.

Followed by the experiment in stagnant air, the existing modes of interaction in a range of water flow rates at various air flow rates were identified as; ‘stable sheets’, ‘broken sheets’, ‘flapping sheets’ and ‘stable lifted sheet’. These were then mapped based on the Reynolds number of the air stream and the Weber number of water.

These modes were explained by the relative intensities of the momentum of the air and water flows, surface tension forces and the blockage ratio. At lower airflow rates and regardless of the water flow rate, the trajectory of the falling water was observed to be stable. This stable sheet was transformed to a broken sheet at increased airflow rates and low water flow rates, whereas at higher water flow rates, increasing the airflow rate

caused the formation of flapping sheets. It was observed that further increase in the airflow rate would cease the flapping, which forms the stable lifted sheet.

The intensities of heat and mass transfer in these flow regimes were briefly discussed based on the characteristics of each flow regime. It is most likely that among the observed modes of interaction, the ‘flapping sheet’ and ‘stable lifted sheet’ would have the highest heat and mass transfer coefficients.

Chapter 4 : FALLING WATER SHEETS IN A CROSSFLOW DUCTED AIR STREAM-HEAT AND MASS TRANSFER

4.1. Introduction

It was shown in Chapter 2 that improving the heat and mass transfer in the humidifier leads to significant improvement of the performance of a solar HDH desalination system. In this regard, a crossflow interaction between air and falling sheets of water was proposed in Chapter 3. Considering that the nature of the flow and the interaction of the phases has a significant influence on the transfer processes, a series of experiments were performed to identify and map the different flow regimes. The flow regime map developed in the previous chapter can now be used to direct the investigation into the heat and mass transfer processes. To address this, another experimental study was designed to measure the rates of heat and mass transfer in the identified flow regimes.

4.2. Formulating the Transfer Processes

In order to be able to generalise heat and mass transfer processes to the design of heat and mass exchangers they should be formulated in dimensionless terms. Nusselt and Sherwood numbers are the representative dimensionless numbers used to describe the heat and mass transfer phenomenon, respectively. In consideration of the mass transfer process, the Sherwood number is defined by Equation 39.

$$Sh = \frac{jL_{ch}}{\lambda_{a-w}} \tag{39}$$

Where, the mass transfer coefficient (j) can be found from Equation 40.

$$j = \frac{\dot{m}_{ev}}{A\left(\rho_{v,f} - \rho_{v,\infty}\right)} \tag{40}$$

The rate of evaporation ($\dot{m}_{ev}$) in Equation 40 is determined from the change in specific humidity in Equation 41.

$$\dot{m}_{ev} = \dot{m}_a(\omega_{a,out} - \omega_{a,in}) \tag{41}$$

And assuming water vapour as an ideal gas, the vapour density (ρ_v) can be calculated from Equation 42.

$$\rho_v = \frac{P_v}{R_v T} \tag{42}$$

On the heat transfer side, the experimental value of Nusselt number is defined by Equation 43.

$$Nu = \frac{hL_{ch}}{k_{a,f}} \tag{43}$$

Where the heat transfer coefficient (h) can be determined from Equation 44.

$$h = \frac{\dot{Q}_{conv}}{A\left(T_f - T_\infty\right)} \tag{44}$$

The film temperature (T_f) is the mean temperature of air and water streams. As mentioned earlier, the effect of radiation heat transfer is neglected, therefore, the rate of convective heat transfer ($\dot{Q}_{conv}$) can be determined from Equation 45.

$$\dot{Q}_{conv} = \dot{Q}_t - \dot{Q}_{ev} \tag{45}$$

Where, the rate of total heat transfer ($\dot{Q}_t$) and the rate of evaporative heat transfer ($\dot{Q}_{ev}$) are given in Equations 46 and 47, respectively.

$$\dot{Q}_t = \dot{m}_a(\hbar_{a,out} - \hbar_{a,in}) \quad (46)$$

$$\dot{Q}_{ev} = \dot{m}_{ev}\hbar_{fg} \quad (47)$$

4.2.1. Dimensional Analysis

For many simple forced convection processes, the Nusselt number is a function of the Reynolds number and the Prandtl number as given in Equation 48 [79],

$$Nu = f(Re, Pr) \quad (48)$$

Similarly, the Sherwood number is governed by the Reynolds and Schmidt numbers, as given in Equation 49 [79].

$$Sh = f(Re, Sc) \quad (49)$$

In circumstances where the thermal and concentration boundary conditions are of the same type, the mathematical function is similar for both Nusselt and Sherwood numbers [79]. In more complex conditions, the Nusselt number might be governed by some other dimensionless groups in addition to the Reynolds and Prandtl numbers [112-115]. Similarly, the Sherwood number might be characterised by dimensionless groups other than Reynolds and Schmidt numbers [116, 117]. Therefore, in order to develop the correlations of heat and mass transfer in terms of Nusselt and Sherwood numbers, the dimensionless groups that describe the heat and mass transfer phenomena, should be identified in advance.

To this end, the Buckingham π theorem was employed in order to identify the effective dimensionless groups in the particular circumstances of a falling sheet of water

crossed by a ducted airflow. This analysis, detailed in Appendix B, delivered eight independent dimensionless groups, as shown in Table 5.

Table 5. Independent dimensionless groups

$\pi_1 = \frac{L_{ch}h}{k_a}$	$\pi_3 = \frac{\rho_a V_{ch} L_{ch} cp_a}{k_a}$	$\pi_5 = \frac{\lambda_{a-w}}{V_{ch} L_{ch}}$	$\pi_7 = \frac{\hbar_{fg}}{{V_{ch}}^2}$
$\pi_2 = \frac{\mu_a}{\rho_a V_{ch} L_{ch}}$	$\pi_4 = \frac{k_a \Delta T}{\rho_a {V_{ch}}^3 L_{ch}}$	$\pi_6 = \frac{j}{V_{ch}}$	$\pi_8 = \frac{\hbar_f}{{V_{ch}}^2}$

Traditional dimensionless groups were identified as follow: π_1 is the Nusselt number (*Nu*), π_2^{-1} is the Reynolds number (*Re*), π_3 is the Peclet number (*Pe*), π_5^{-1} is the Bodenstein (*Bd*) or mass Peclet (Pe_m) number and π_7^{-1} is the Evaporation number (N_{ev}). Grouping π_2 and π_3 delivers the Prandtl number (*Pr*) and combination of π_2 and π_5 gives the Schmidt number (*Sc*).

As seen in Table 5, some new dimensionless group were also identified as follow: π_4 is the ratio of sensible heat transfer to the inertia of the air stream and π_6 is the ratio of the mass transfer coefficient to the characteristic velocity. π_8 is the ratio of the enthalpy content of water at film condition to the kinetic energy of the air stream, which can be considered as both a heat and mass transfer related dimensionless groups.

It should be noted that the Weber number used for mapping the flow regime does not feature in this analysis as it characterises the mechanics of the fluids but not the heat and mass transfer.

4.2.2. Experimental Method

An experimental approach was chosen to characterise and develop the correlations of heat and mass transfer in a crossflow configuration for each mode of interaction. The apparatus used in this experiment, shown in Figure 46, was the same as the one detailed

in Chapter 3. In this case, the intention of the experiment was to measure the heat and mass transfer. To determine the heat and mass transfer coefficients, a set of three humidity/temperature sensors, (Sensirion SHT71) with an accuracy of ±0.3% for relative humidity and ±0.4°*C* for temperature at standard room condition were used. Two of these sensors were placed across the sheet measuring the change in humidity and temperature of the air stream as it crossed the water sheet, and the third one was placed outside the equipment to monitor the room conditions. The first sensor was placed just before the nozzle in order to record the air condition before contacting the water sheet. The sensor recording the conditions of the air after contact was placed 300 *mm* downstream from the nozzle, so the air and water interaction would be completed before reading. The data from the sensors was logged using a Sensirion evaluation kit (EK-H4). Additionally, a set of two thermocouples (type T) with an accuracy of ±0.3℃ accompanied with a PicoLog (TC08) data logger were used to record the water temperature before and after contact with the air stream. An auxiliary water heater was used to control the inlet water temperature.

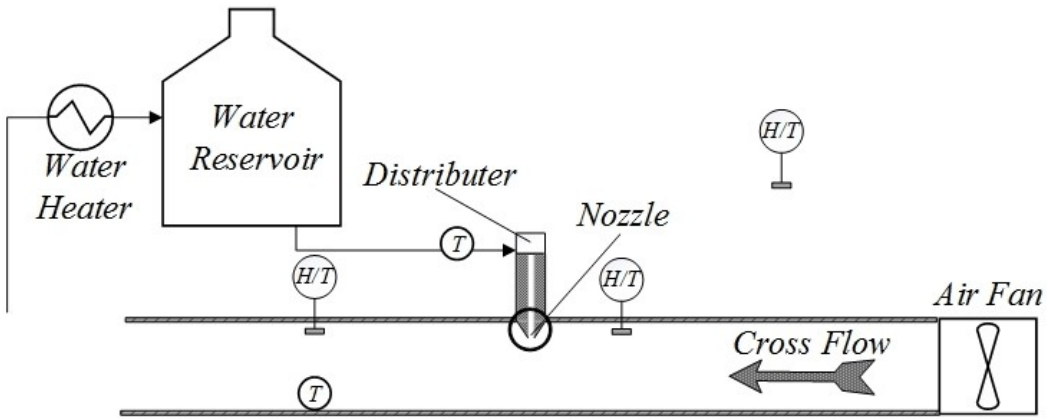

Figure 46. Experimental apparatus

During the experiment, the effects of air and water flow rates, as well as inlet water temperature and channel height were evaluated. The air and water flow rates were determined as previously described in section 3.2. The air temperature and humidity were

not controlled in the experiment, but carefully monitored. The system pressure was also not controlled, but the atmospheric pressure was measured by a mercury barometer (*Griffin & Sons*). Table 6 shows the conditions of the experiment. The uncertainty associated with these measurements is analysed in Appendix A.

Table 6. Experimental conditions for heat and mass transfer measurements

Nozzle width (W_{noz})	(m)	*0.1*
Nozzle thickness (Th_{noz})	(m)	*0.0005*
Air flow rate ($\dot{V}_a$)	(m^3/s)	0.42×10^{-2} *to* 2×10^{-2}
Water flow rate ($\dot{V}_w$)	(m^3/s)	2×10^{-5} *to* 5×10^{-5}
Water temperature (T_w)	($^{\circ}C$)	*30 ; 35 ; 40 ; 45*
Fall height (H_F)	(m)	*0.036 ; 0.048*

4.3. Results: Heat and Mass Transfer Correlation

From the measurements made during the experiment and the dimensionless parameters previously defined, the heat and mass transfer coefficients were determined for each condition tested.

The analogy between the heat and mass transfer for crossflow interaction was also tested. In this respect, it was noted that, due to the low temperature conditions of the experiments, a significant amount of the heat energy supplied would be used to overcome the latent heat. On this basis, it is reasonable to expect that the analogy between the heat and mass transfer would account for this. In this regard, by performing a least squares analysis on the dimensionless parameters identified by the Buckingham π theorem, a modified version of the Chilton-Colburn analogy was developed, as shown in Equation 50.

$$h_t = j\rho_a cp_a \left(Le \frac{\hbar_{fg}}{\hbar_f} \right)^{0.575} \quad (50)$$

This analysis on the "analogy" between heat and mass transfer are detailed in Appendix C, however was not used in this study, as both heat and mass transfer data were determined from the experimental measurements.

With regard to the heat and mass transfer, correlations of the Nusselt and Sherwood numbers are typically reported in the form of power functions [79]. Based on this, it was attempted to deliver the Nusselt and Sherwood numbers as power functions including the effective dimensionless parameters. In order to define these correlations, a least squares analysis was performed for the Nusselt and Sherwood numbers determined from the experimental data. The following sections detail the analysis undertaken for the different modes of interaction as identified in Chapter 3.

4.3.1. Stable Sheet

A stable sheet of water can be formed in air crossflow if the airflow is not strong enough to break the sheet. Increasing the water flow rate at constant airflow rates, enhances the area of the water sheet, which increases the blockage ratio and consequently the air velocity as it passes the sheet. Under the conditions of a stable sheet, this increase in blockage ratio is likely to improve the heat and mass transfer processes. In this respect, the "water to air mass flow ratio" was considered as an effective dimensionless parameter to describe the mass transfer coefficients of a 'stable' sheet. With this, the correlation for Sherwood number was defined as being a function of mass transfer related dimensionless groups, identified by the Buckingham π theorem and the mass flow ratio, as given in Equation 51.

$$Sh = aRe^{x}Sc^{y}{N_{ev}}^{z}{\pi_8}^{t}\left(\frac{\dot{m}_w}{\dot{m}_a}\right)^{k} \tag{51}$$

Performing the least squares analysis on Equation 51, determines the coefficients of the correlation shown in Equation 52.

$$Sh = 3.95 \times 10^{-6}Re^{1.88}Sc^{0.43}{N_{ev}}^{0.43}{\pi_8}^{-0.43}\left(\frac{\dot{m}_w}{\dot{m}_a}\right)^{0.88} \tag{52}$$

From this correlation, shown in Figure 47, it can be seen that more that 85% of the predicted data from the correlation lies within 25% of the experimental values determined by Equation 39.

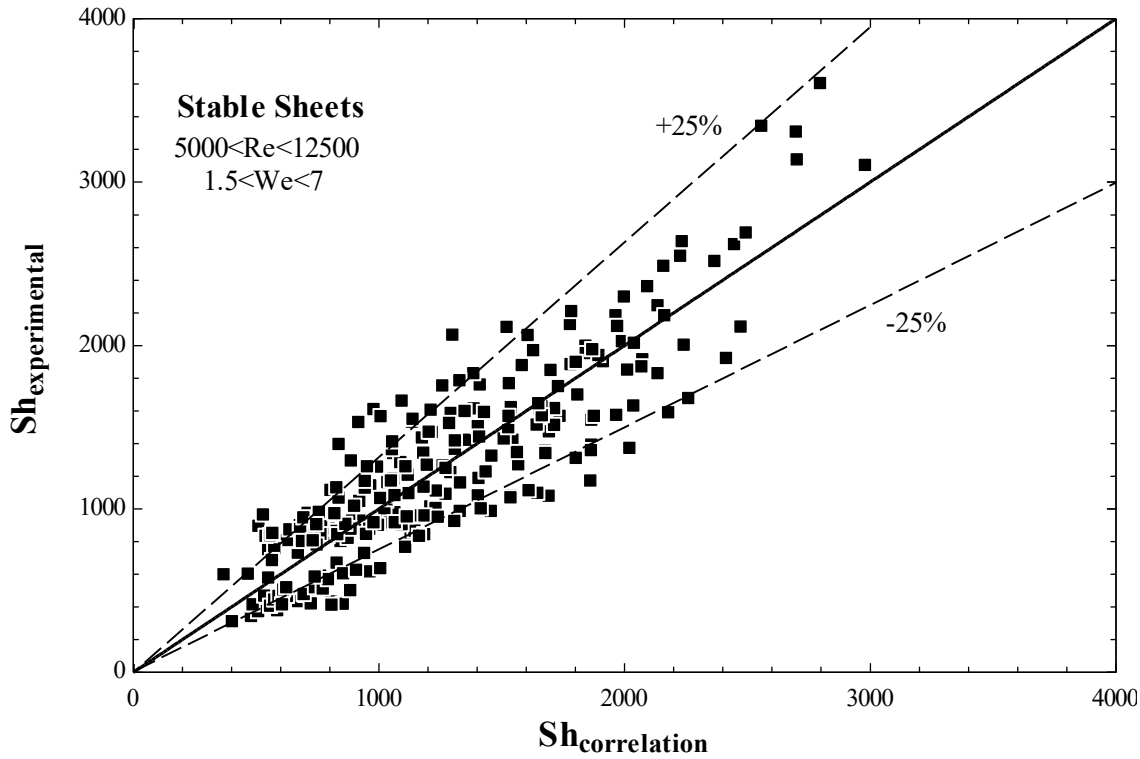

Figure 47. The experimental Sherwood number versus calculated value

In Equation 52 it was found that the exponent of Schmidt and Evaporation numbers are equal and the exponent of π_8 holds the negative value of the exponents of Schmidt and Evaporation numbers. Thus, Equation 52 can be simplified as shown in Equation 53.

$$Sh = 3.95 \times 10^{-6}\, Re^{1.88} \left(\frac{ScN_{ev}}{\pi_8}\right)^{0.43} \left(\frac{\dot{m}_w}{\dot{m}_a}\right)^{0.88} \tag{53}$$

The ratio of Evaporation number and π_8 is in fact the ratio of the enthalpy of evaporation of water to the enthalpy content of air at the film condition, where the air is saturated at the mean temperature of air and water. This ratio will be referred to as the enthalpy ratio in this context, and the product of this ratio and the Schmidt number forms a new dimensionless number. From hereon this will be referred to as the Schmidt Number of Evaporation, as defined in Equation 54.

$$Sc_{ev} = \frac{ScN_{ev}}{\pi_8} = \frac{\frac{\mu_a}{\rho_a \lambda_{a-w}} \frac{\hbar_{fg}}{{V_{ch}}^2}}{\frac{\hbar_f}{{V_{ch}}^2}} = \frac{\nu_a}{\lambda_{a-w}} \frac{\hbar_{fg}}{\hbar_f} = Sc \frac{\hbar_{fg}}{\hbar_f} \tag{54}$$

By examination, it is concluded that this Schmidt Number of Evaporation expresses the viscous diffusion and mass diffusion with respect to the required heat of evaporation and the enthalpy content of the bulk stream at the film conditions. This new dimensionless number characterises the mass transfer in a low temperature evaporation process.

Now, the correlation for the Sherwood number given in Equation 53 can be simplified to Equation 55.

$$Sh = 3.95 \times 10^{-6}\, Re^{1.88} {Sc_{ev}}^{0.43} \left(\frac{\dot{m}_w}{\dot{m}_a}\right)^{0.88} \tag{55}$$

As the Nusselt number is the heat transfer equivalent of the Sherwood number, and since the mechanism of heat and mass transfer are functionally similar, the correlation for Nusselt number is expected to be similar to Sherwood correlation. Therefore, the

correlation of Nusselt number was set as a function of heat transfer-related dimensionless groups from the Buckingham π theorem and the mass flow ratio as given in Equation 56.

$$Nu = aRe^{x}Pr^{y}{N_{ev}}^{z}{\pi_8}^{t}\left(\frac{\dot{m}_w}{\dot{m}_a}\right)^{k} \tag{56}$$

Performing the least square analysis on the Nusselt number given in Equation 56, determines the constants for the correlation as given in Equation 57.

$$Nu = 3.95 \times 10^{-6}Re^{1.88}Pr^{0.43}{N_{ev}}^{0.43}{\pi_8}^{-0.43}\left(\frac{\dot{m}_w}{\dot{m}_a}\right)^{0.88} \tag{57}$$

As illustrated in Figure 48 more that 85% of data from this correlation are within 25% of the experimental values of the Nusselt number.

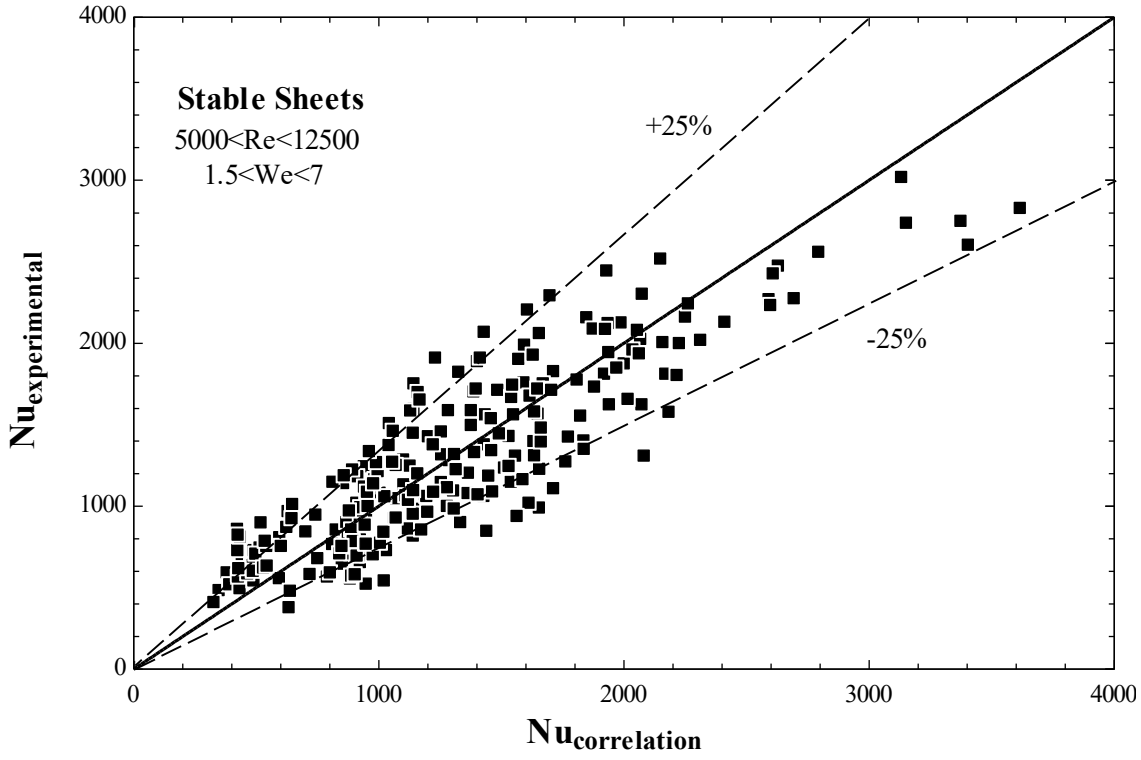

Figure 48. Comparison of Nusselt number with its experimental values

Analogous to the correlation of Sherwood number, the dimensionless groups; π_8, Prandtl and Evaporation numbers can be combined, which reduces Equation 57 to Equation 58.

$$Nu = 3.95 \times 10^{-6}\, Re^{1.88} \left(\frac{PrN_{ev}}{\pi_8}\right)^{0.43} \left(\frac{\dot{m}_w}{\dot{m}_a}\right)^{0.88} \tag{58}$$

The product of Prandtl number and the ratio of π_8 and Evaporation number, as presented in Equation 59, form a new dimensionless group, hereafter called the Prandtl Number of Evaporation.

$$Pr_{ev} = \frac{PrN_{ev}}{\pi_8} = \frac{\frac{cp_a \mu_a}{k_a}\frac{\hbar_{fg}}{{V_{ch}}^2}}{\frac{\hbar_f}{{V_{ch}}^2}} = \frac{cp_a\, \mu_a}{k_a}\frac{\hbar_{fg}}{\hbar_f} = Pr\frac{\hbar_{fg}}{\hbar_f} \tag{59}$$

The Prandtl Number of Evaporation expresses the ratio of viscous diffusion to thermal diffusion relative to the enthalpy of vaporization and the enthalpy content of the air stream at its film condition. Hence, higher values indicate that viscous diffusion is the dominant mechanism. The ratio of latent heat of vaporization to the heat capacity of the bulk fluid, characterizes the low temperature evaporation processes where the enthalpy of evaporation is significantly higher than that delivered to the system.

Following from this, Nusselt number has a similar functional form to the Sherwood number and is determined to be a function of Reynolds number and Prandtl Number of Evaporation, as well as the water to air mass flow ratio. Equation 60 shows the empirical relation for Nusselt number found from this work.

$$Nu = 3.95 \times 10^{-6}\, Re^{1.88} {Pr_{ev}}^{0.43} \left(\frac{\dot{m}_w}{\dot{m}_a}\right)^{0.88} \quad (60)$$

4.3.2. Broken Sheet

A broken sheet was formed at relatively low flow rates of water and high airflow rates. When compared to stable sheets, the water sheet has a very small effect on the cross-sectional area of air stream. Due to the narrow range of water flow rates that led to broken sheets, the mass flow rate of water and consequently mass flow ratio was found to be practically ineffective on the mass transfer. Therefore, the functional form of the Sherwood number was taken to be a function of the mass transfer related dimensionless groups from the Buckingham π theorem, as given in Equation 61.

$$Sh = aRe^{x}Sc^{y}{N_{ev}}^{z}{\pi_8}^{t} \quad (61)$$

By performing the least squares analysis, the coefficients of the correlation were determined that defined the Sherwood number as shown in Equation 62.

$$Sh = 0.00035\, Re^{2.9}Sc^{2.9}{N_{ev}}^{0.91}{\pi_8}^{-0.000335} \quad (62)$$

As illustrated in Figure 49, more that 80% of the calculated results from the empirical correlation are within 25% of the experimental values of the Sherwood number.

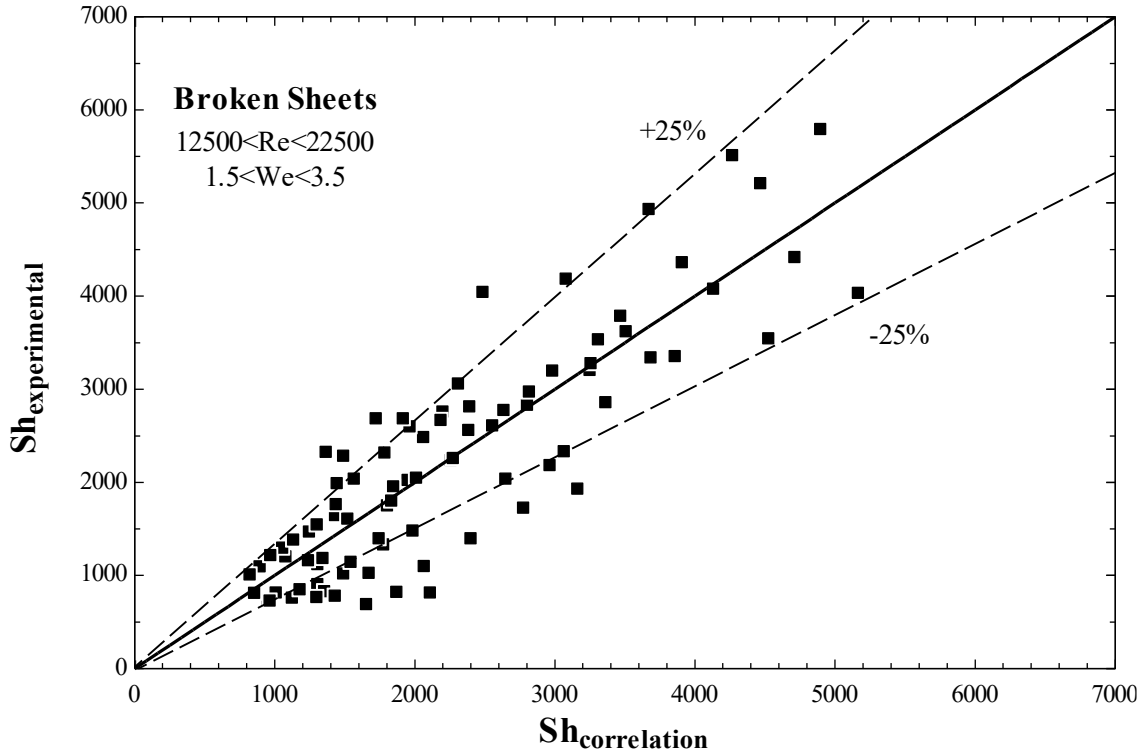

Figure 49. Experimental Sherwood number versus the corresponding values from the empirical correlation

The exponents of the Reynolds and Schmidt numbers, in Equation 62, are equal and are combined to form the Bodenstein Number (mass transfer Peclet number). The very small exponent of π_8 suggests that, in the range tested, this number does not affect the value of Sherwood number and can be excluded from the correlation. Hence, Equation 62 can be simplified as Equation 63.

$$Sh = 0.00035\ Bd^{2.9} {N_{ev}}^{0.91} \tag{63}$$

This can be explained by the fact that in a broken sheet, the water sheet breaks into smaller fingers or droplets, and since the airflow is considerably higher than the water flow rate, the water temperature drops rapidly to the wet bulb temperature of air as a result of evaporative cooling. Under these circumstances, the film temperature would be the wet bulb temperature of the air stream. Therefore, the main mechanism of mass transfer would be through advection, which can be described by the Bodenstein number. On the other

hand, some of the mass transfer is taking place as a result of sheet breakup by the air stream through viscous diffusion, where the driving force is the kinetic energy of the air stream.

Analogous to the Sherwood number, the Nusselt number was determined to be a function of the Peclet number, which is the equivalent of the Bodenstein number in heat transfer, and the Evaporation number. Due to the heat and mass transfer analogy, the functional form of the Nusselt number is similar to that describing Sherwood number and is given by Equation 64.

$$Nu = 0.00035\ Pe^{2.9}\mathrm{N}_{ev}{}^{0.91} \tag{64}$$

As shown in Figure 50, more that 80% of the calculate data are within 25% of the experimental values of the Nusselt number.

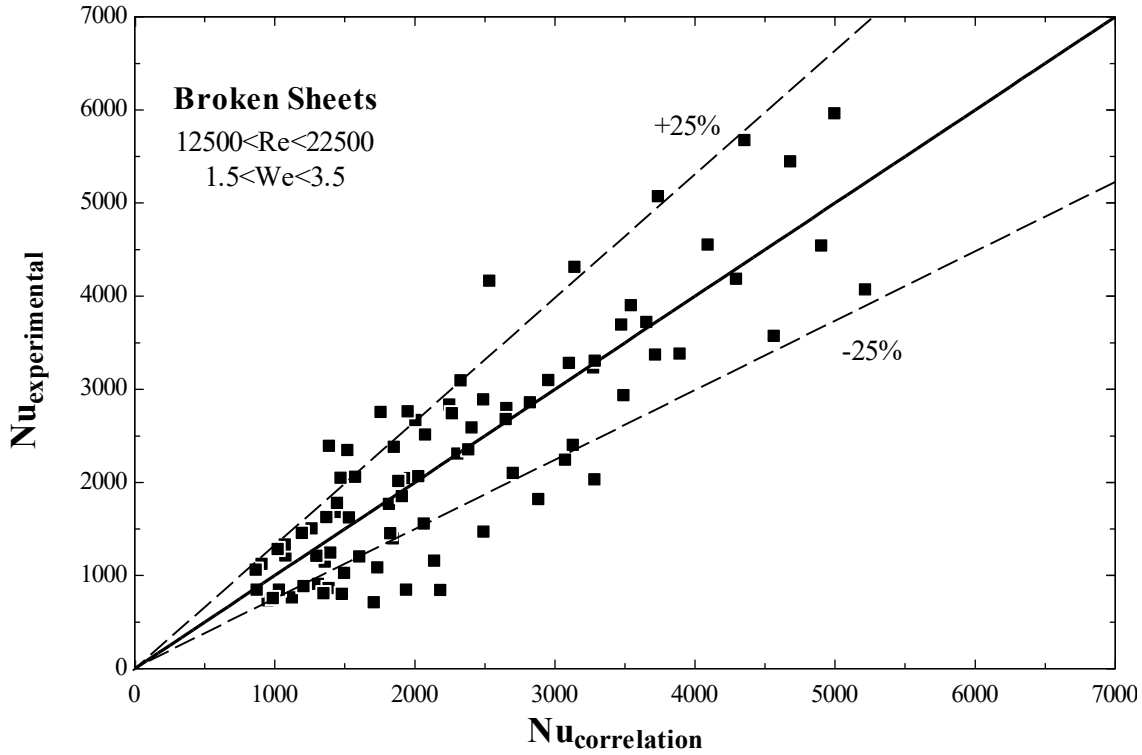

Figure 50. Experimental Nusselt number versus the corresponding calculated values

4.3.3. Flapping Sheet

Increasing the airflow at high water flow rates results in the formation of flapping sheets of water. As a result of high flow rates of water, the mechanism of heat and mass transfer under the conditions of flapping sheets is similar to stable sheets. However, due to the flapping nature of this flow regime, the blockage ratio changes continuously. This makes the cross sectional area of the airflow independent of the water flow rate and as a consequence, the mass flow ratio was found to have little influence on the Sherwood number. Therefore, the initial correlation of Sherwood number was written as a function of mass transfer related dimensionless groups from the Buckingham π theorem, as shown in Equation 65.

$$Sh = aRe^{x}Sc^{y}{N_{ev}}^{z}{\pi_8}^{t} \tag{65}$$

A least squares analysis was used to determine the coefficients of the correlation, which resulted in Equation 66.

$$Sh = 4.78 \times 10^{-8}Re^{2.23}Sc^{1.17}{N_{ev}}^{1.17}{\pi_8}^{-1.17} \tag{66}$$

Similar to the correlation of the Sherwood number for the stable sheets, the exponent of Schmidt and Evaporation numbers are equal and the exponent of π_8 holds the negative value of the exponents of Schmidt and Evaporation numbers. Therefore, the Sherwood number correlation for flapping sheets can be represented as a function of the Reynolds and Schmidt Number of Evaporation as given in Equation 67.

$$Sh = 4.78 \times 10^{-8}\, Re^{2.23}{Sc_{ev}}^{1.17} \tag{67}$$

A comparison of the predicted and measured values of the Sherwood number is shown in Figure 51, where it is seen that more that 80% of the predicted values, are within a range of 30% of the experimental values.

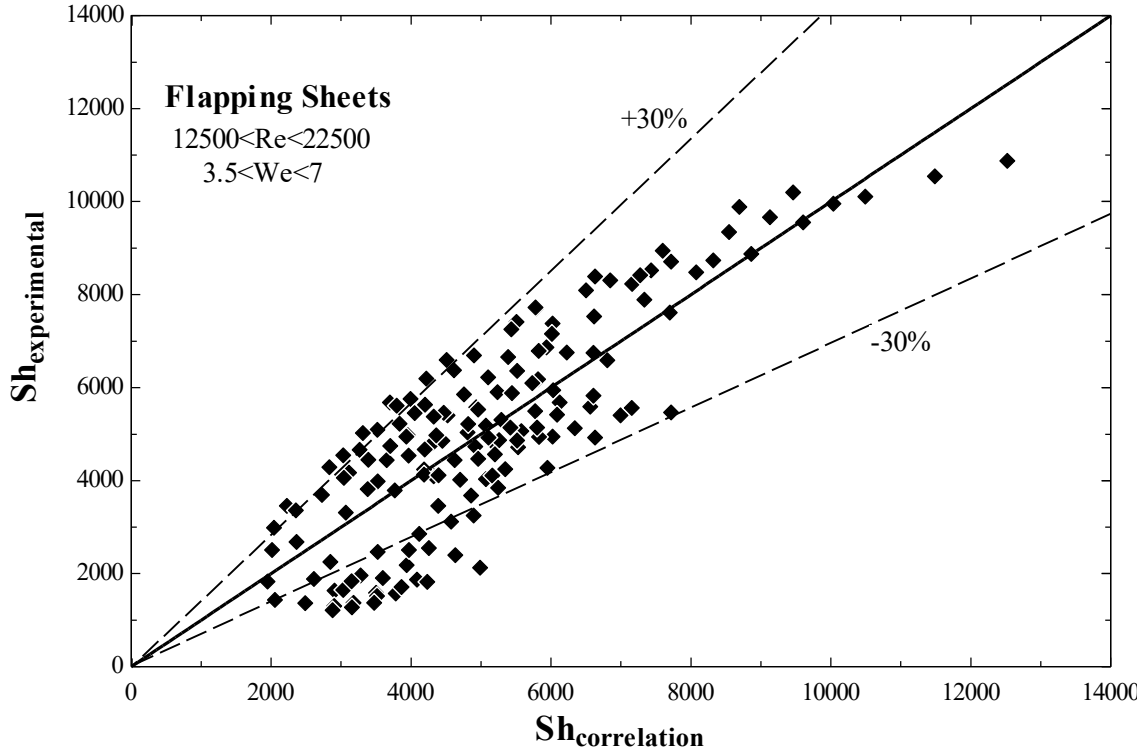

Figure 51. Experimental Sherwood versus the correlation for flapping sheet

In consideration of the heat transfer in flapping sheets, analogous to Sherwood number, the correlation for Nusselt number was initially set to be a function of the heat transfer-related dimensionless groups from the Buckingham π theorem as given in Equation 68.

$$Nu = aRe^{x}Pr^{y}{N_{ev}}^{z}{\pi_8}^{t} \tag{68}$$

The coefficients of the correlation, determined by performing a least squares analysis, are given in Equation 69.

$$Nu = 4.78 \times 10^{-8}Re^{2.23}Pr^{1.17}{N_{ev}}^{1.17}{\pi_8}^{-1.17} \tag{69}$$

The comparison of the predicted and experimental values of Nusselt number, Plotted in Figure 52, shows that more that 80% of the calculated data, are within 30% of the experimental values.

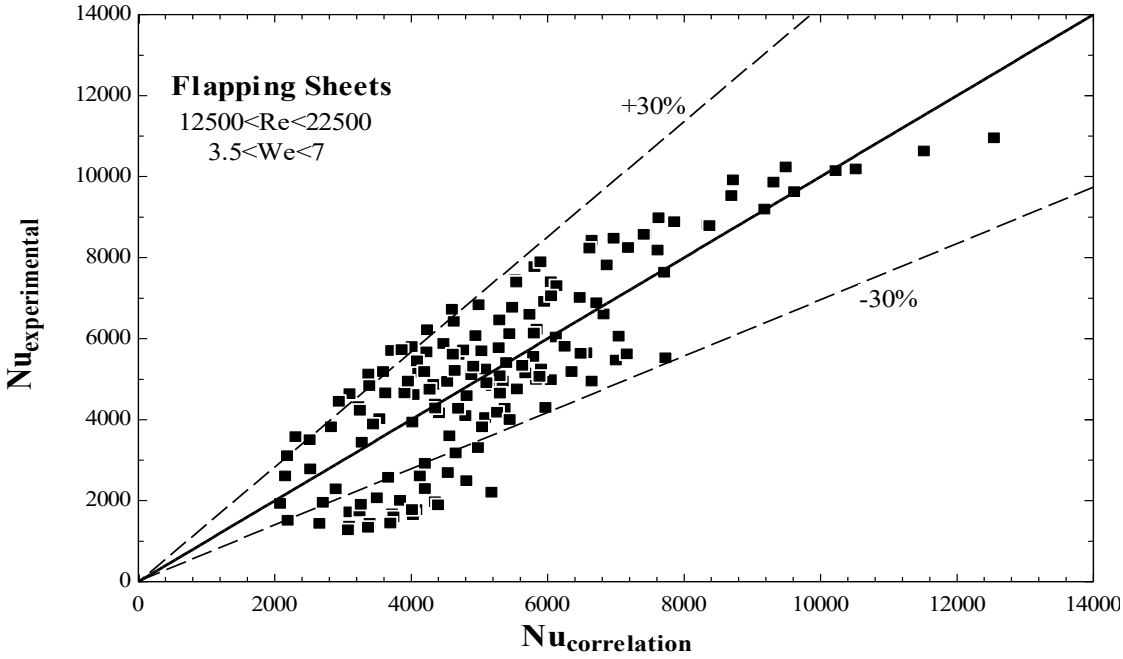

Figure 52. Comparison of the correlation of Nusselt number with the experimental values

It was seen in Equation 69 that the exponents of Prandtl and Evaporation numbers are equal and the exponent of π_8, holds the negative value of the exponent of Prandtl and Evaporation numbers. Therefore, the correlation for Nusselt number of flapping sheets can be defined as a function of the Reynolds number and the Prandtl Number of Evaporation, as given by Equation 70.

$$Nu = 4.78 \times 10^{-8}\, Re^{2.23} {Pr_{ev}}^{1.17} \tag{70}$$

4.4. Conclusions of the Experiment

An experimental investigation was performed in order to formulate the intensities of heat and mass transfer in different flow regimes in a crossflow interaction of air and falling sheets of water. Correlations for the Nusselt and Sherwood numbers were determined for the stable, broken and flapping sheets, using the Buckingham π theorem and a least squares analysis. Table 7 shows a summary of the derived correlations with their range of occurrence.

Table 7. Experimental correlation of Sherwood and Nusselt numbers for crossflow liquid and gas interaction

	Flow regime	Criteria	Experimental Correlation
Nusselt Number	Stable	Re<12500	$Nu = 3.95 \times 10^{-6}\, Re^{1.88} {Pr_{ev}}^{0.43} \left(\frac{\dot{m}_w}{\dot{m}_a}\right)^{0.88}$
		1.5<We<7	
	Broken	Re>12500	$Nu = 0.00035\, Pe^{2.9} {\mathrm{N}_{ev}}^{0.91}$
		1.5<We<3.3	
	Flapping	12500<Re<24000	$Nu = 4.78 \times 10^{-8}\, Re^{2.23} {Pr_{ev}}^{1.17}$
		3.3<We<7	
Sherwood Number	Stable	Re<12500	$Sh = 3.95 \times 10^{-6}\, Re^{1.88} {Sc_{ev}}^{0.43} \left(\frac{\dot{m}_w}{\dot{m}_a}\right)^{0.88}$
		1.5<We<7	
	Broken	Re>12500	$Sh = 0.00035\, Bd^{2.9} {\mathrm{N}_{ev}}^{0.91}$
		1.5<We<3.3	
	Flapping	12500<Re<24000	$Sh = 4.78 \times 10^{-8}\, Re^{2.23} {Sc_{ev}}^{1.17}$
		3.3<We<7	

From these analyses, new dimensionless parameters were identified to characterise the transfer phenomena for low temperature evaporation processes. One of these parameters was defined as the ratio of the enthalpy of evaporation to the enthalpy of the air at film condition, which was referred to as the enthalpy ratio. In considering the heat transfer process, the product of this parameter and the Prandtl number gave rise to a new dimensionless number, which was named the Prandtl Number of Evaporation. Similarly,

with regard to mass transfer, the Schmidt Number of Evaporation was defined as the product of the Schmidt number and the enthalpy ratio.

For ‘stable’ sheets, as a consequence of the weak inertia of the airflow, the two stream cannot be mixed effectively and hence the transfer area is limited to the area of the water sheet. This leads to the weakest intensities of heat and mass transfer. It was noted that the mass flow ratio was an additional dimensionless parameter to describe the correlation of heat and mass transfer. This was explained by the effect of mass flow rate of water on the relative velocity of air as it passes the water sheet. Therefore, the correlation of Sherwood number was defined as a function of the Reynolds number and the Schmidt Number of Evaporation as well as the mass flow ratio. Analogous to mass transfer, the Nusselt number was determined to be a function of the Reynolds number, Prandtl Number of Evaporation and the mass flow ratio of air and water.

For ‘broken’ sheets, as a consequence of droplet formation, a large transfer area was provided, which led to higher intensities of heat and mass transfer. However, due to the comparatively low mass flow rate of water, the water temperature drops quickly in the air stream, which reduces the transfer phenomena. It was found that on the mass transfer side, the Sherwood number is a function of the Bodenstein and the Evaporation numbers. Similarly, on the heat transfer side, the Nusselt number was described based on the Peclet and Evaporation numbers.

For ‘flapping’ sheets, due to oscillation of the water flow, the airflow continuously changes around the water, which significantly improves the transfer processes. Furthermore, the droplet formation at the tail end of the sheet provides a large transfer area, which also aids the heat and mass transfer. Therefore, as expected, higher intensities of heat and mass transfer were observed for flapping sheets. In consideration of mass

transfer, the correlation of Sherwood number was presented as a function of the Reynolds number and the Schmidt Number of Evaporation, similarly for heat transfer the Nusselt number was defined as a function of the Reynolds number and the Prandtl Number of Evaporation.

In the proposed humidifier in Chapter 2, the air and water interaction was a simple counter-flow contact that provided no mixing of the fluids. Compared to the interaction modes in a cascading humidifier illustrated in this chapter, this seems to be less effective. Therefore, the performance of the cascading humidifier is expected to be significantly higher than the simple long channel, that was modelled in Chapter 2. This would justify an attempt to mathematically model a cascading humidifier based on the heat and mass transfer correlations that have been developed in this chapter.

Chapter 5 : MATHEMATICAL MODELLING OF AN ADVANCED HDH DESALINATION SYSTEM WITH CASCADE HUMIDIFIER

5.1. Introduction

As mentioned earlier, it appears that the application of a cascading humidifier in HDH desalination systems has not been investigated. Based on the relationships of the heat and mass transfer, gained in Chapter 4, and with respect to the flow regime map, developed in Chapter 3, one would be able to develop a cascading humidifier that can be used to improve the efficiency of the simple HDH Desalination system that was proposed in Chapter 2.

5.2. Model Development: Cascading Humidifier

In the proposed cascading humidifier, water enters the humidifier from top and flows over the first tray. At the tail end of the tray, water falls to the underneath tray and then flows over the second tray. Air is blown into the humidifier from the bottom in the opposite direction to the water stream, which forms a counter current flow pattern over the trays. Once the air reaches the tail end of the tray, it passes through the falling water, which makes a crossflow pattern at the tail ends of trays. In Chapter 2 the air stream flowing over the trays, was modelled for flow in an asymmetric heated rectangular duct. The Nusselt number for turbulent conditions was given in Equation 30, which is repeated in Equation 71.

$$Nu = 0.023Re^{0.8}Pr^{1/3} \tag{71}$$

Analogous to heat transfer, the Sherwood number for laminar flow was 3.39, and for turbulent flow was determined from Equation 32, which is repeated in Equation 72.

$$Sh = 0.023Re^{0.8}Sc^{1/3} \tag{72}$$

Adding the crossflow to this system, the correlations for Sherwood and Nusselt numbers given in Table 8 were determined for stable (Equations 55 and 60), broken (Equations 63 and 64) and flapping sheets (Equations 67 and 70).

Table 8. Experimental correlation of Sherwood and Nusselt numbers for crossflow liquid and gas interaction

	Flow regime	Criteria	Experimental Correlation
Nusselt Number	Stable	Re<12500	$Nu = 3.95 \times 10^{-6}\ Re^{1.88}Pr_{ev}{}^{0.43}\left(\frac{\dot{m}_w}{\dot{m}_a}\right)^{0.88}$
		1.5<We<7	
	Broken	Re>12500	$Nu = 0.00035\ Pe^{2.9}\mathrm{N}_{ev}{}^{0.91}$
		1.5<We<3.3	
	Flapping	12500<Re<24000	$Nu = 4.78 \times 10^{-8}\ Re^{2.23}Pr_{ev}{}^{1.17}$
		3.3<We<7	
Sherwood Number	Stable	Re<12500	$Sh = 3.95 \times 10^{-6}\ Re^{1.88}Sc_{ev}{}^{0.43}\left(\frac{\dot{m}_w}{\dot{m}_a}\right)^{0.88}$
		1.5<We<7	
	Broken	Re>12500	$Sh = 0.00035\ Bd^{2.9}\mathrm{N}_{ev}{}^{0.91}$
		1.5<We<3.3	
	Flapping	12500<Re<24000	$Sh = 4.78 \times 10^{-8}\ Re^{2.23}Sc_{ev}{}^{1.17}$
		3.3<We<7	

Once the Nusselt number was calculated, the heat transfer coefficient was calculated from Equation 73.

$$h = \frac{Nu\ k_a}{L_{ch}} \tag{73}$$

Subsequently, the convective heat transfer rate was determined from Equation 74.

$$\dot{Q}_{conv} = hA(T_f - T_{a,in}) \tag{74}$$

Knowing the experimental Sherwood number, the coefficient of mass transfer was calculated from Equation 75.

$$j = \frac{Sh\ \lambda_{a-w}}{L_{ch}} \tag{75}$$

Similarly, the rate of mass transfer was determined from Equation 76.

$$\dot{m}_{ev} = jA(\rho_{a,s} - \rho_{a,\infty}) \tag{76}$$

Knowing the rates of heat and mass transfer, and applying the energy balance, the conditions of air and water at both ends of humidifier was predicted.

5.2.1. Computational solution

Engineering Equation Solver (EES) was employed to model this cascading humidifier. An iterative algorithm, illustrated in Figure 53, was designed to calculate the temperature and humidity of the outlet air as well as the outlet temperature of water based on the inlet flow rates and conditions of each stream and the characteristics of the humidifier.

The model first assumes the outlet temperature of water to be the wet-bulb temperature of the inlet air, as the lowest possible temperature of the system. In the second step, it calculates the conditions of air after the first crossflow contact with water, using the equations given in Table 8 and considering that the enthalpy of air remains constant due to evaporative cooling below saturation conditions. Applying the energy balance across the water sheet, the enthalpy and consequently temperature of water at the tail end of the last tray can be determined. Thereafter, if the air is not saturated, the model

calculates the conditions of air after counter-current interaction, based on Equations 71 and 72.

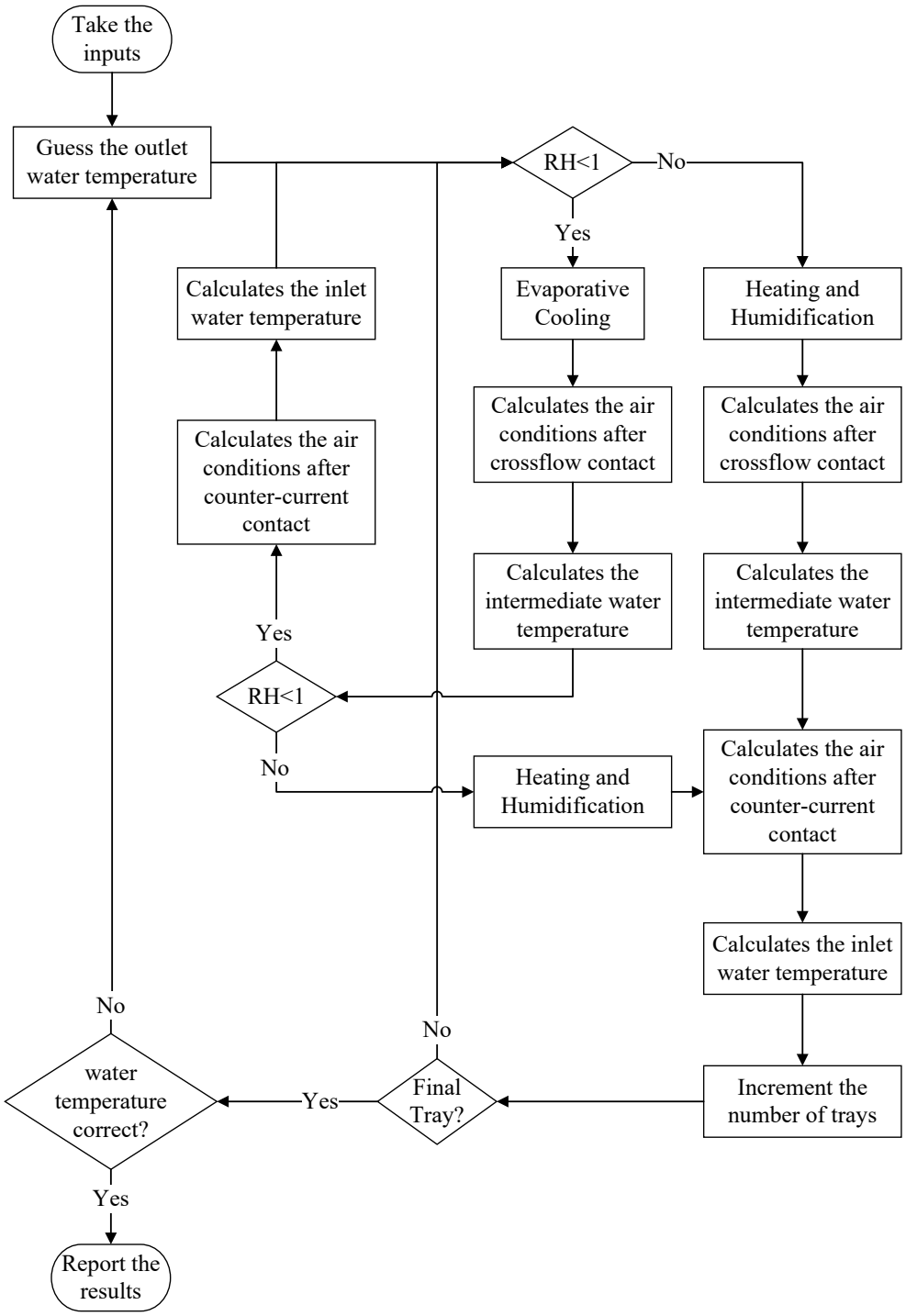

Figure 53. Flow chart of the humidifier model

Again applying the energy balance the water temperature at the front end of the tray can be determined. The model then checks the conditions of the airflow and if not yet saturated, repeats the process above. Otherwise, calculates the air conditions,

considering heating and humidification process. Successively solving for each tray, the water temperature at the front end of the top tray as well as the condition of the exhaust air can be determined.

Once the inlet temperature of the top tray is determined, the program compares it with the given inlet water temperature to the humidifier, based on a pre-defined convergence limit. If the error is in an acceptable range ($< 0.01\ ^{\circ}C$), the model reports the outlet water temperature as well as the humidity and temperature of the exhaust air. Otherwise, the initial guess value would be refined according to the value of the calculated error.

5.2.2. Results: The Humidifier

The performance of a humidifier can be evaluated based on the total amount of evaporation as well as the conditions of the exhaust air. A sensitivity analysis was performed on the evaporation rate as well as the temperature of exhaust air by changing the operating parameters and fluid conditions. Table 9 shows the variables examined, their range of variation and their nominal values.

Table 9. Range of the operating parameters in the cascading humidifier

Variable	*Unit*	*Range*	*Nominal value*
Evaporation area (A_{hmd})	(m^2)	0.12 to 0.75	0.36
Air flow rate ($\dot{V}_a$)	(m^3/s)	0.003 to 0.032	0.005 , 0.03
Water flow rate ($\dot{V}_w$)	(m^3/s)	2×10^{-5} *to* 5×10^{-5}	3.5×10^{-5} , 2.8×10^{-5}
Inlet water temperature ($T_{w,in}$)	($^{\circ}C$)	25 to 45	37
Inlet air temperature ($T_{a,in}$)	($^{\circ}C$)	10 to 30	20

Considering the overall performance of the HDH desalination system, it was also shown in Chapter 2, that the temperature of the water stream leaving the humidifier has an effect on the yield of the system. Therefore, in addition to the conditions of the air

stream leaving the humidifier, the temperature of the outlet water was also considered in sensitivity analysis.

As shown in Figure 54 and Figure 55, preheating the air stream, has a significant effect on increasing the temperature of the discharge brine, but a poor effect on increasing the exhaust air temperature and thus evaporation rate. However, increasing the temperature of inlet water to the humidifier showed a striking effect on the outlet conditions of both air and water streams.

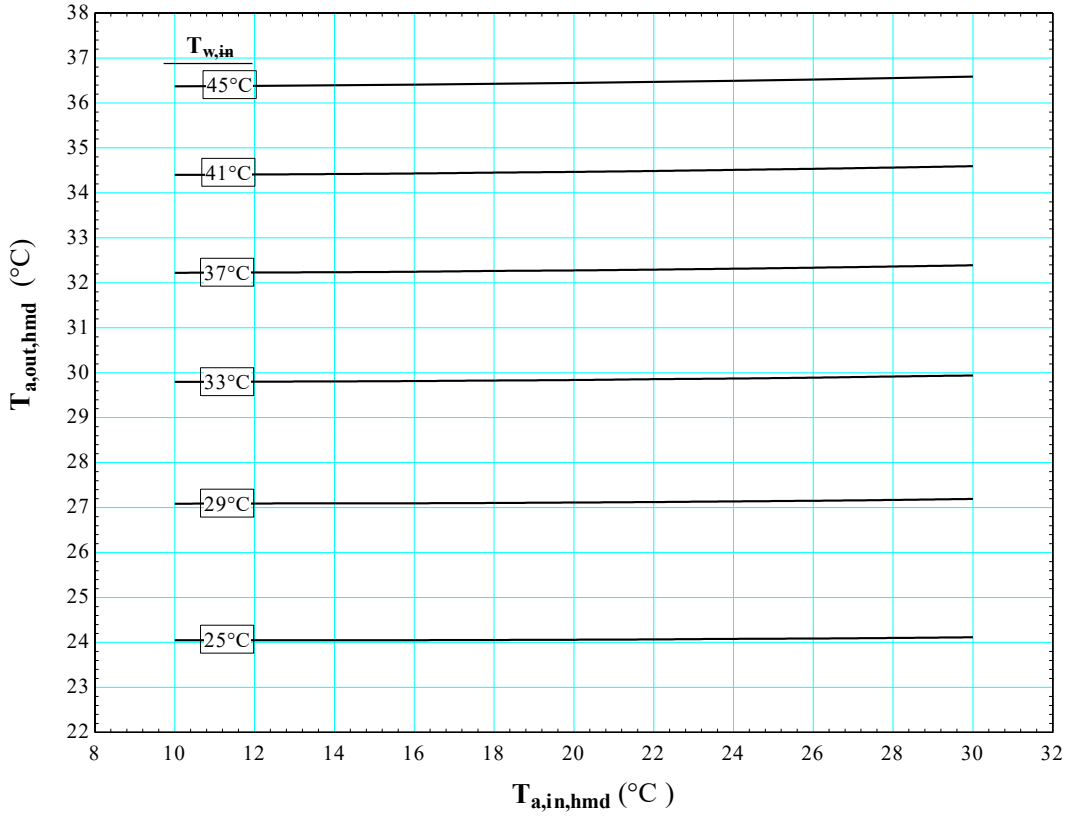

Figure 54. Variation of the moist air temperature leaving the humidifier with changing the inlet air and water temperatures

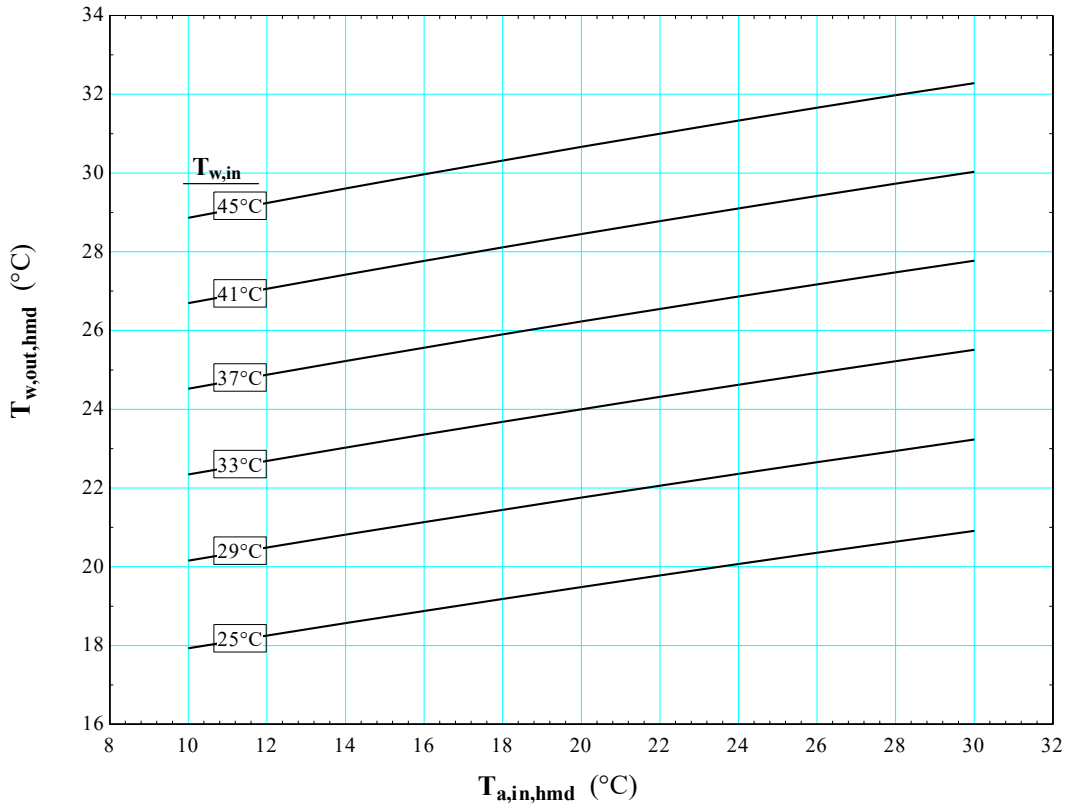

Figure 55. Variation of the outlet water temperature from the humidifier with changing the inlet air and water temperatures

As the heat and mass transfer rates are directly allied to the mechanism of interaction between the two fluids, at a particular aspect ratio of the air channel, changing the air and water mass flow rates transforms the flow regimes. Therefore, in addition to inlet conditions of air and water streams, the effects of air and water flow rates needed to be taken into consideration.

Increasing the airflow rate at a constant water flow rate transforms the flow regime from stable sheet to either flapping or broken sheets, depending on the water flow rate. As shown in Figure 56, increasing the airflow rate under the conditions of 'stable sheets', where the heat and mass transfer intensities are weak, initially reduces the temperatures of both exiting air and water streams but increases the total rate of evaporation.

At sufficiently high water flow rates, further increasing of the airflow rate above approximately 0.012 m^3/s transforms the flow regime to flapping and consequently

enhances the heat and mass transfer processes. This results in a higher rate of evaporation and consequently larger temperature drop of the water stream.

Increasing the airflow rate increases the Reynolds number of air as well as the moisture carrying capacity of the air stream and improves the transfer phenomena. These enhance the total rate of evaporation, and consequently increase the temperature change of the water stream in the humidifier. On the other hand, increasing the airflow rate reduces the temperature change of the air stream in the humidifier due to larger mass of air supplied. Once the exhaust air temperature reaches its maximum possible temperature at around 0.015 m^3/s (for a given evaporation area, water and air inlet temperature and water flow rate), increasing the airflow rate reduces the exhaust air temperature due to larger quantities of air supplied.

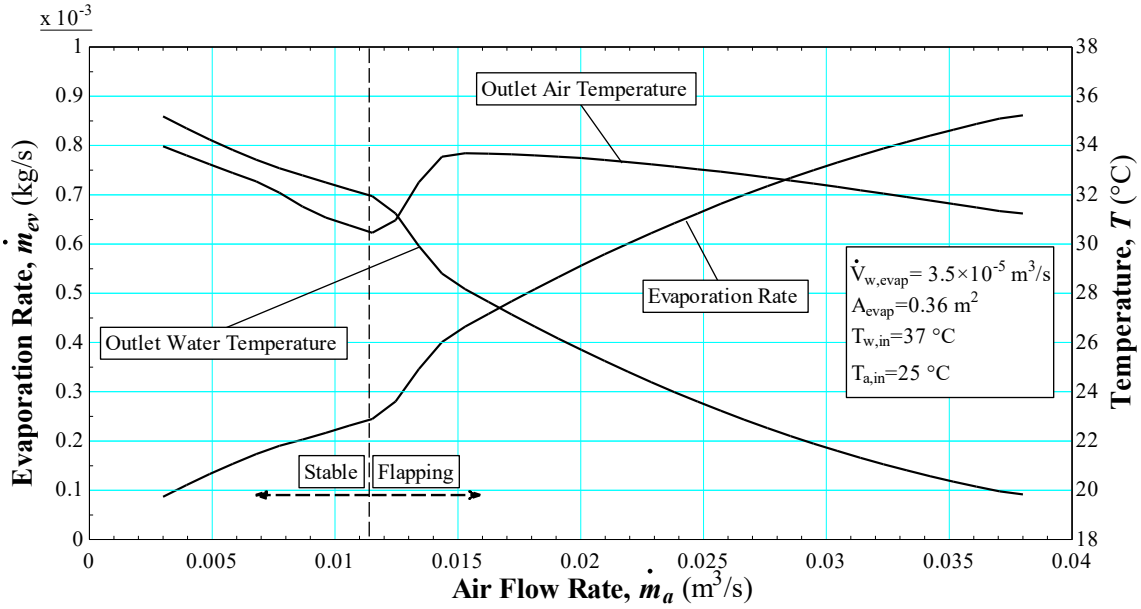

Figure 56. The effect of airflow rate on the evaporation rate and the outlet air and water temperatures from the humidifier at high water flow rate

At lower flow rates of water, increasing the airflow rate, results in transformation of the flow regime from stable to broken, in which the heat and mass transfer processes are weaker. Therefore, as shown in Figure 57 the evaporation rate as well as the outlet

temperature of air reduces whereas the discharge water temperature increases with change of flow regime at an airflow rate of approximately 0.014 m^3/s. However, the broken flow regime occurs at higher flow rates of air where the Reynolds number of air is larger. Therefore, while the flow regime is broken, increasing the airflow rate enhances the intensities of heat and mass transfer. This would initially increase the temperature of exhaust air, however as illustrated in Figure 57 the temperature of exhaust air drops for flow rates of above approximately 0.03 m^3/s. This can be explained by the fact that the extracted heat from the water stream is transferred to a larger mass of air.

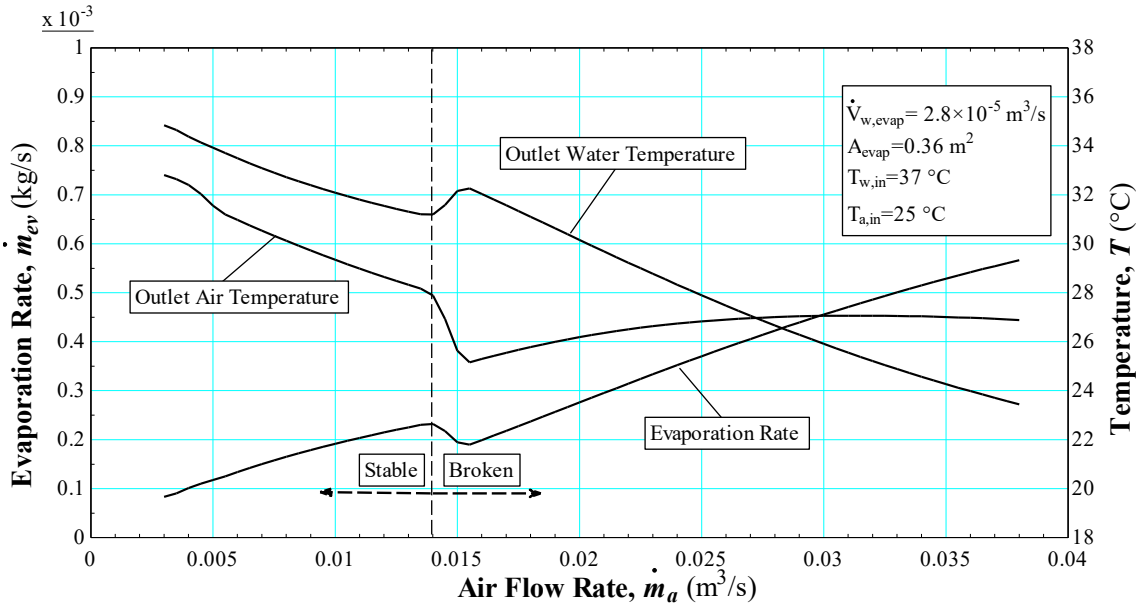

Figure 57. The effect of airflow rate on the evaporation rate and the outlet air and water temperatures from the humidifier at low water flow rate

Looking at lower airflow rates, where the flow regime in the crossflow interaction is stable, as shown in Figure 58, the temperature of the exhaust air, discharge water and evaporation rate increase with increasing the water flow rate, but the increase is less significant on the discharge water temperature. Increasing the water flow rate while the inlet water temperature is maintained constant and the flow regime is stable (low airflow rates) increases the mass flow ratio, which directly enhances the transfer processes. As a

consequence, the temperature of the exhaust air and the evaporation rate increase with increasing the water flow rate, whereas the temperature of the discharge water tends to decrease. Increasing the water flow rate however, reduces the temperature drop across the water stream as a larger mass of water loses heat to the air stream.

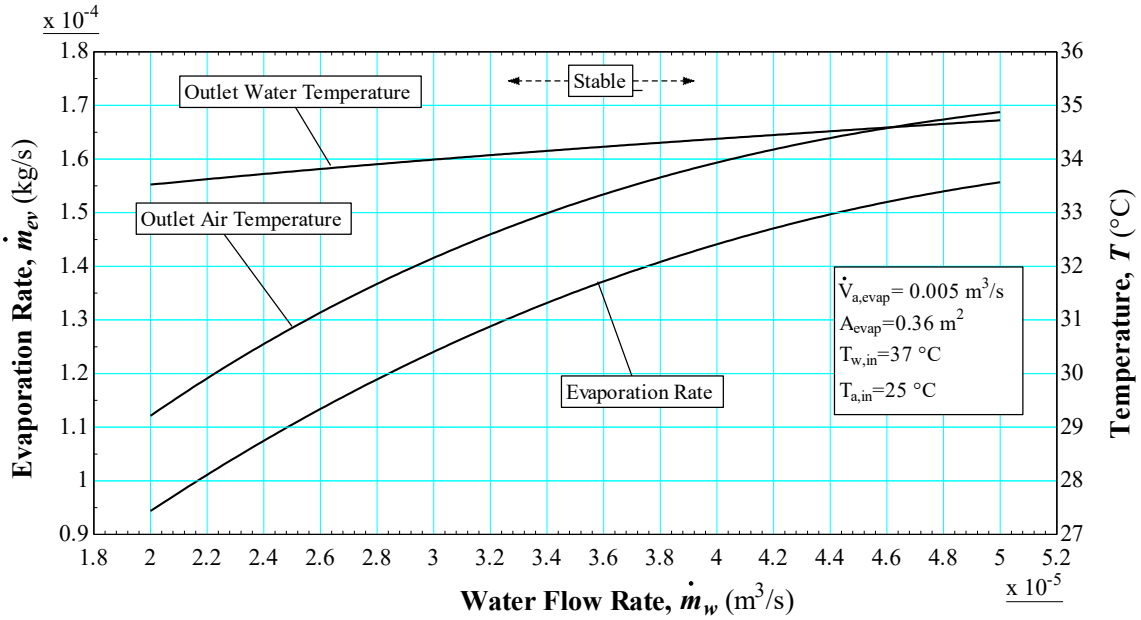

Figure 58. The effect of increasing water flow rate on the evaporation rate and exiting temperature of air and water (stable mode)

Now, considering the effects of water flow rate, it can be outlined that increasing the water flow rate, improves the transfer processes by influencing the Reynolds number of the air stream on one hand and on the other hand by increasing the input heat to the system. Hence, as shown in Figure 59 the temperature of the discharge water decreases whereas the exhaust air temperature increases with increasing the water flow rate.

Further increasing the water flow rate transforms the flow to flapping mode, which enhances the transfer process significantly. Therefore, as illustrated in Figure 59, at a water flow rate of around 2.65×10^{-5} m^3/s, marked increases were seen in the outlet air temperature and the evaporation rate.

At higher water flow rates, a larger mass of water loses heat to the airflow, hence, the discharge water temperature increases when the water flow rate is increased beyond approximately 3.1×10^{-5} m^3/s. However, the temperature of inlet water constrains the temperature of the exhaust air, and as a result, the moisture carrying capacity and the evaporation rate. Hence, the exhaust air temperature and the evaporation rate increase only slightly by increasing the water flow rate above 3.1×10^{-5} m^3/s.

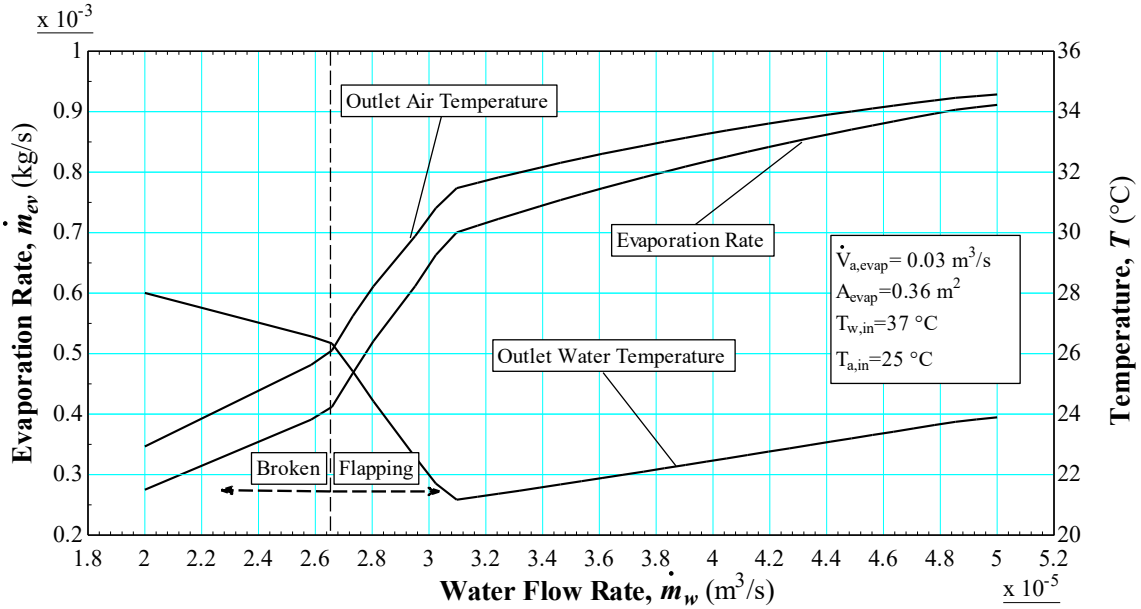

Figure 59. The effect of water flow rate on the outlet temperatures of air and water from the humidifier (broken and flapping modes)

Finally, as shown in Figure 60 enlarging the area of the humidifier increases the evaporation rate and the temperature of the exiting moist air, while decreasing the temperature of the discharge water. The area of evaporation can be increased by adding additional trays in the humidifier, which also increases the number of crossflow contacts in the system. In this respect, the temperature of the inlet water constrains the temperature and moisture carrying capacity of the air and as a result, the evaporation rate. Therefore, as shown in Figure 60, increasing the area of evaporation beyond $0.45m^2$ does not provide

a significant increase in the evaporation rate and hence, the outlet temperatures of air and water change only slightly.

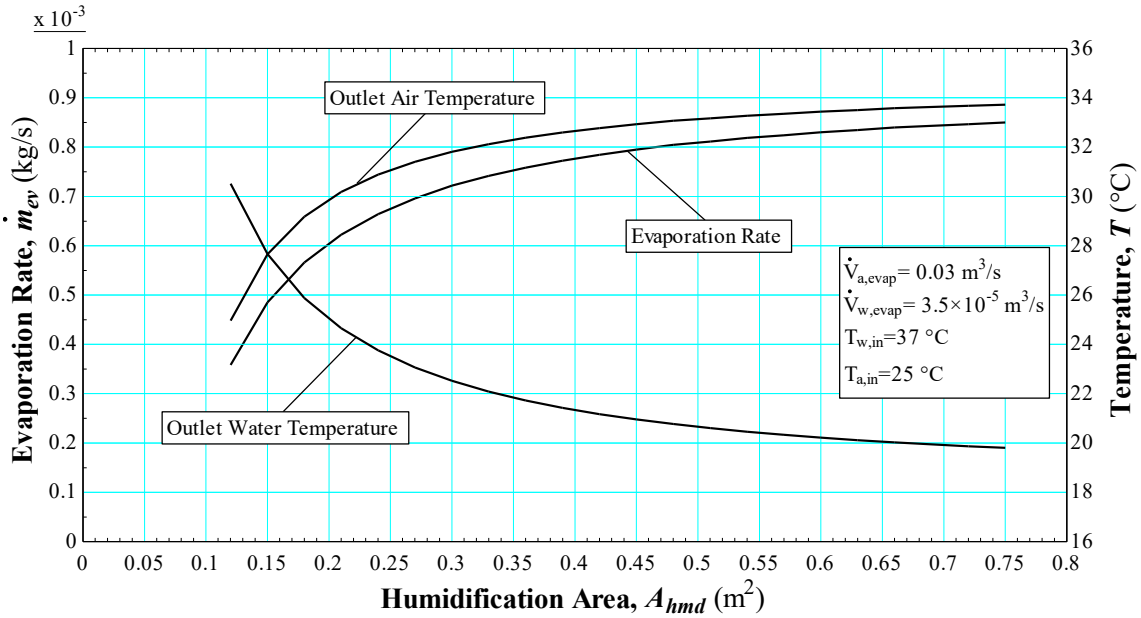

Figure 60. Effect of evaporation area on the rate of evaporation and the temperature of exiting air and water

The model of the humidifier shows an effective transfer phenomenon in cascading configuration, which justifies the application of cascading humidifiers in simple HDH desalination systems.

5.2.3. Results: Solar HDH Desalination System with Cascading Humidifier

In Chapter 2, a solar HDH desalination system was modelled mathematically. In the modelled system a standard solar water collector was used as the heater, the condenser and economizer were single pass shell and double pass tube heat exchangers, and a simple long channel with a rectangular cross section was considered as the humidifier. Using the same climatic conditions as in Chapter 2, a typical summer day in New Zealand was considered for this investigation, where the average radiation received on the absorber plate is 1000 W/m^2 and the average velocity of wind is 5 m/s. The average seawater

temperature is assumed to be 15 °C and the ambient air temperature is 20 °C with a relative humidity of 50%.

In this section, the performance of the modelled cascading humidifier in the solar desalination system modelled in Chapter 2, is examined and compared with a system using a long channel humidifier. The design parameters for the cascading humidifier and the other parts of the system are given in Table 10.

Table 10. Design parameters of the HDH desalination with cascading humidifier

Water Collector		Humidifier		Condenser		Economizer	
$N_{g,col}$	*2 [-]*	A_{hmd}	*0.49 [m^2]*	$N_{\tau,cond}$	*20 [-]*	$N_{\tau,econ}$	*20 [-]*
$N_{\tau,col}$	*20 [-]*	$L_{Tr,hmd}$	*0.35 [m]*	$N_{bf,cond}$	*19 [-]*	$N_{bf,econ}$	*19 [-]*
$D_{o,\tau,col}$	*0.0127 [m]*	$W_{Tr,hmd}$	*0.1 [m]*	$D_{o,\tau,cond}$	*0.0127 [m]*	$D_{o,\tau,econ}$	*0.0127 [m]*
$D_{i,\tau,col}$	*0.01181 [m]*	$H_{ch,hmd}$	*0.05 [m]*	$D_{i,\tau,cond}$	*0.01181 [m]*	$D_{i,\tau,econ}$	*0.01181 [m]*

In order to be able to design and develop a HDH desalination system for a particular location, the sensitivity of the climatic and operational parameters on the rate of production needs to be evaluated. Table 11 show the range and the nominal values of the examined parameters.

Table 11. Range of the independent variables for sensitivity analysis

Variable	*Unit*	*Range*	*Nominal value*
Evaporation area (A_{hmd})	(m^2)	*0.14 to 0.49*	*0.49*
Air flow rate ($\dot{V}_a$)	(m^3/s)	*0.003 to 0.03*	*0.025*
Water flow rate ($\dot{V}_w$)	(m^3/s)	2×10^{-5} *to* 5×10^{-5}	3.3×10^{-5}
Total radiation (G_t)	(W/m^2)	*300 to 1300*	*1000*

As shown in Figure 61, increasing the radiation received on the absorber plate, puts extra energy into the water stream, and consequently increases the evaporation in the humidifier, which eventually increases the production of the system. As shown in Figure 61, for the same radiation received, the system with a cascading humidifier produces more fresh water compared to a system with a long channel humidifier.

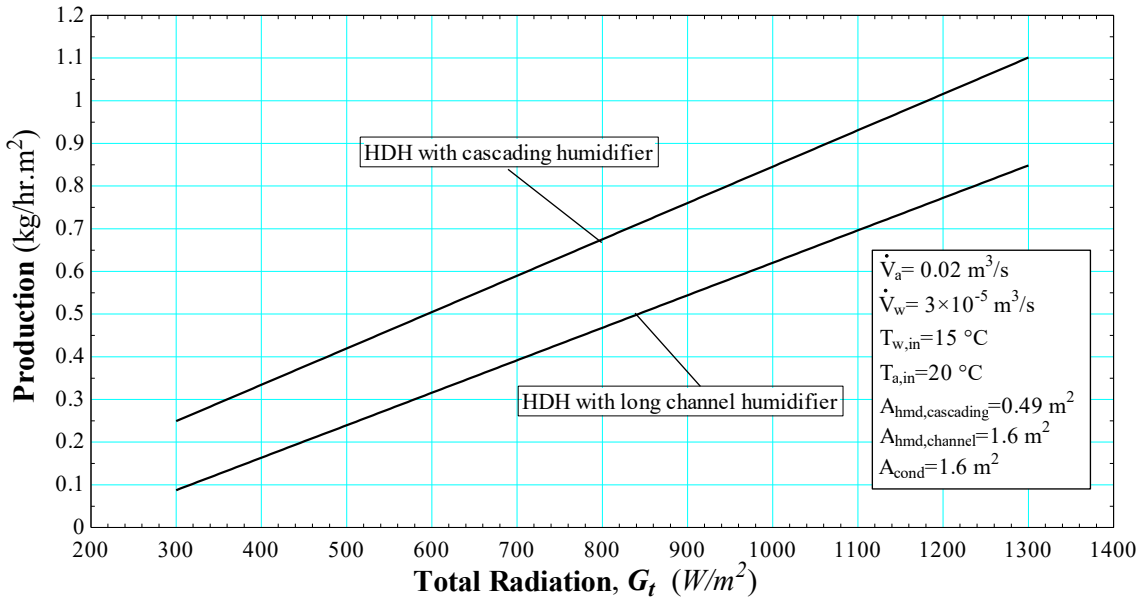

Figure 61. Variation of production versus radiation

As illustrated in Figure 62, increasing the airflow rate initially increases the system production but above $0.8\times10^{-2}\ m^3/s$ has a reducing effect. Then again, further increasing the airflow rate above $1.2\times10^{-2}\ m^3/s$ increases the yield of the system. Increasing the airflow rate enhances the turbulence of the airflow in the humidifier, and also increases the moisture carrying capacity of the air stream. This increases the rate of evaporation in the humidifier but due to the larger volumes of air reduces the change in air temperature in both the humidifier and dehumidifier.

On the other hand, due to the increased evaporation rate, increasing the airflow rate has a cooling effect on the water stream. As a consequence, the inlet water stream to the solar water heater cannot be preheated effectively. This decreases the temperature of the inlet water to the humidifier and acts to reduce the production of the system. Therefore, as shown in Figure 62, increasing the airflow rate above $0.8\times10^{-2}\ m^3/s$, results in a small reduction of the system production. However, further increasing the airflow rate above $1.2\times10^{-2}\ m^3/s$ transforms the flow regime to a 'flapping sheet', which significantly

enhances the intensities of heat and mass transfer and consequently the potable water production.

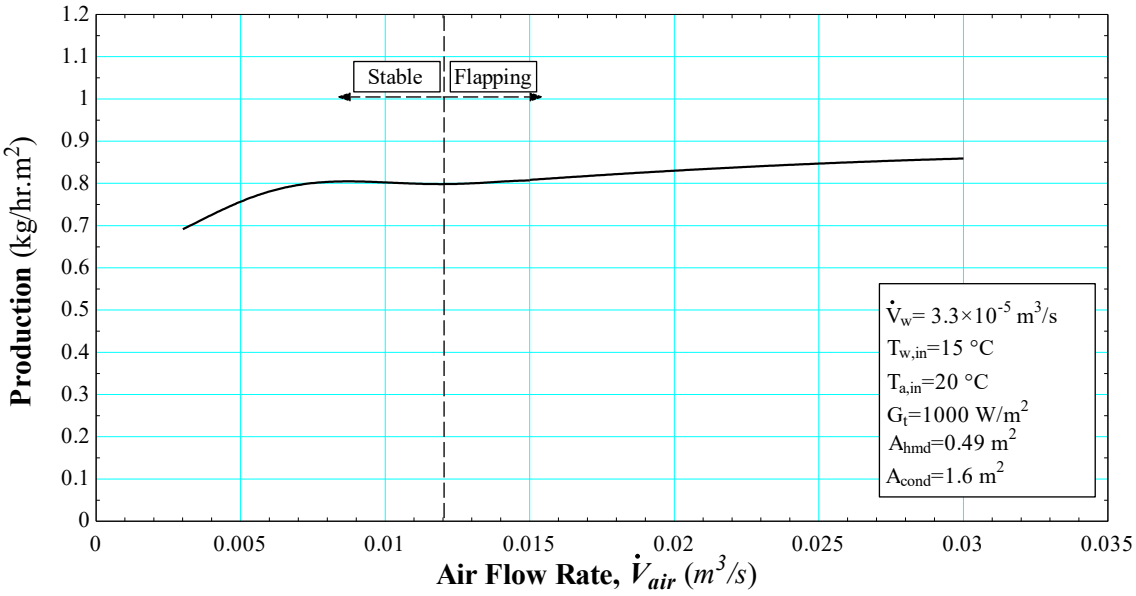

Figure 62. Variation of production versus airflow rate

Now, looking at the effects of increasing the water flow rate, it can be concluded that; increasing the water flow rate enhances the cooling process in the dehumidifier, but weakens the preheating and heating processes in the economizer and the solar water collector. Taking both effects into consideration, increasing the water flow rate, increases the production of the system very gradually. Further, increases in the flow rate of water transform the flow regime from broken to flapping sheets, which enhances the transfer phenomena in the humidifier. This, as discussed previously, increases the evaporation rate but at the same time reduces the temperature of the discharge water from the humidifier. Therefore, as shown in Figure 63, the effect of increasing the water flow rate on the rate of production was found to be very small.

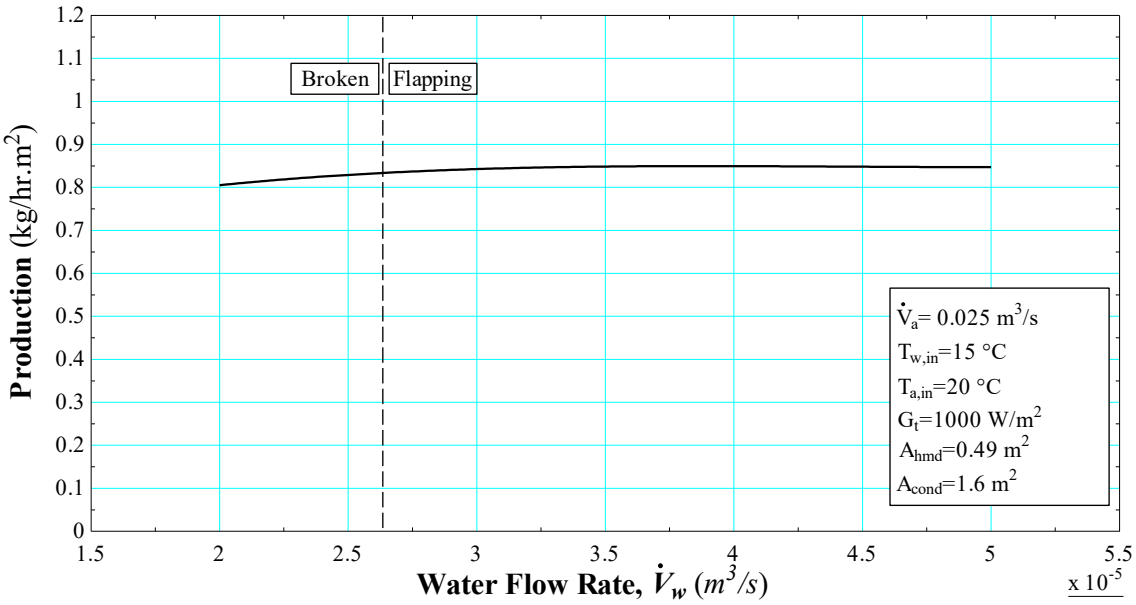

Figure 63. Variation of production versus water flow rate

Finally, the variation of potable production versus the number of cascade trays in the humidifier is shown in Figure 64. Adding more trays in the humidifier, increases the area of evaporation and the number of crossflow interactions, which increase the total yield of the system. However, the temperature of the exhaust air from the humidifier and consequently the rate of evaporation is limited by the inlet water temperature to the humidifier. Therefore, once the evaporation rate in the humidifier is maximized, increasing the number of trays (or evaporation area) does not increase production unless additional energy is added to the system.

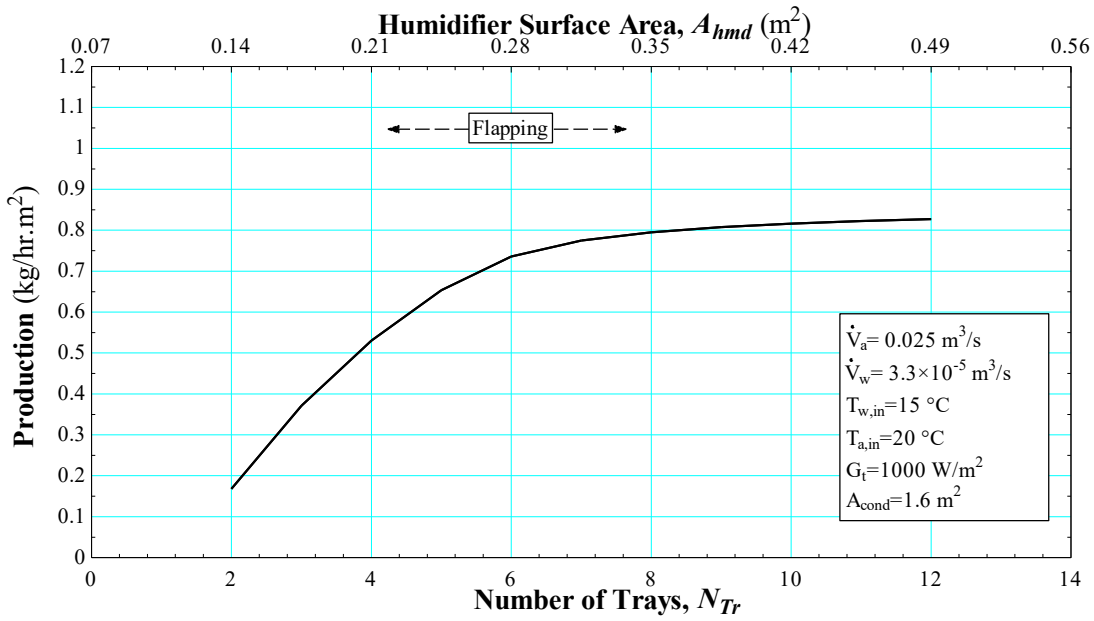

Figure 64. Variation of production versus the number of trays and surface area in the humidifier

That said, compared to the long duct humidifier, the cascade humidifier is a significant improvement in the production for a given humidifier area. As shown in Figure 65, employing a cascading evaporator can increase the yield of the system at lower evaporation areas.

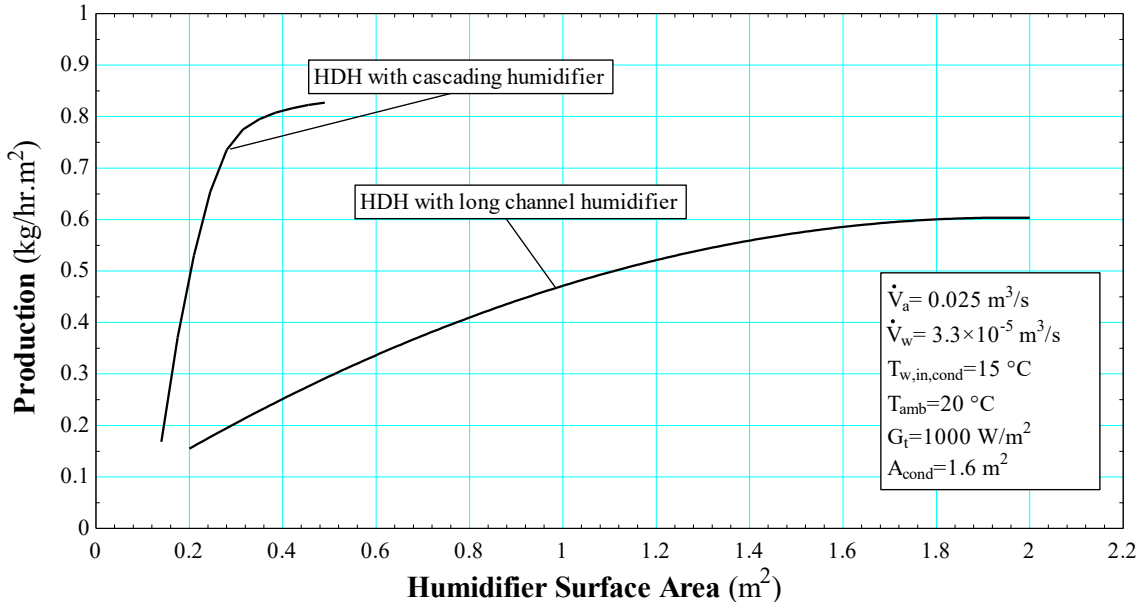

Figure 65. Comparison of the HDH systems with cascading and multi-channel humidifiers

5.3. Chapter Conclusions

A cascading humidifier, with two main types of air and water interaction; crossflow and counter flow, was modelled in this chapter. The simple counter flow interaction was modelled based on the standard correlations for heat and mass transfer in a rectangular duct, described in Chapter 2. Whereas, the crossflow interaction was modelled based on the correlations of heat and mass transfer determined in Chapter 4, for different flow regimes, which were identified in Chapter 3. The sensitivity of the modelled humidifier to the environmental conditions as well as the operating parameters was evaluated and the performance of the system was explained with respect to characteristics of heat and mass transfer in the conditions of the model. It was found that the transition of the flow regime in crossflow interaction would significantly influence the rate of evaporation as well as the outlet temperature of air and water streams.

Thereafter, in order to evaluate the performance of cascading humidifiers in HDH desalination systems, the model of the solar HDH desalination system, introduced in Chapter 2, was modified to include a cascading evaporator. The sensitivity of the new HDH desalination system with a cascading humidifier was tested against different operational and climatic conditions and the performance of the system was explained with respect to its characteristics. A linear relation between the total radiation received on the absorber and the rate of production was observed. Whereas, at the lower range of air flow rates, increasing the airflow rate increased the production to an optimum point, beyond which the production was reduced due to ineffective humidification and dehumidification processes. The rate of production, however, increased by further increasing the air flow rate due to transition of the flow regime from stable to flapping. As a consequence of antithetical effects of increasing the water flow rate on the production, it was seen that

water flow rate has a small effect on the rate of production. It was also found that enlarging the humidification area by increasing the number of cascading trays, increases the yield of the system to a maximum point. Further increasing the production requires additional energy input to the system.

It was seen that using a cascading humidifier can significantly improve the yield of HDH desalination system, and appears to be a simple solution.

Chapter 6 : CONCLUSIONS AND FUTURE WORK

6.1. Conclusions

It was found that improving the heat and mass transfer processes in the humidifier has the potential to increase the yield of the system. In view of that, a novel cascading humidifier that mixes air with falling sheets of water in a crossflow interaction was introduced.

Experiments on falling sheets of water showed that in the absence of airflow, five different shapes of water sheet were observed and detailed: ‘rectangular’, ‘trapezoidal’, ‘V shape’, ‘Y shape’ and ‘finger flow’ sheets. In presence of crossing airflow, four distinct flow regimes were identified and characterised: ‘stable sheet’, ‘broken sheet’, ‘flapping sheet’ and ‘stable lifted sheet’. These were then mapped with respect to the Reynolds number of air and the Weber number of water.

This work identified the dimensionless parameters describing the heat and mass transfer phenomena in the crossflow interaction of air and water streams and three new dimensionless parameters were formulated: the Prandtl Number of Evaporation, the Schmidt Number of Evaporation and the Lewis Number of Evaporation. These dimensionless groups are used to describe the transfer phenomena in low temperature evaporation process in a crossflow interaction.

A series of correlations for the Nusselt and Sherwood numbers were developed, that describe the transfer phenomena for different flow regimes.

Additionally, a modified version of the Chilton-Colburn relationship was developed to describe the analogy between heat and mass transfer.

Using the formulated correlations of the Nusselt and Sherwood numbers, a cascading humidifier was mathematically modelled. From a sensitivity analysis, it was found that the transition of the flow regime in crossflow interaction would significantly influence the rate of evaporation as well as the outlet temperature of air and water streams.

Analysis on the yield of an HDH system with a cascading humidifier has shown that a cascading humidifier can reduce the evaporation area to nearly a quarter of that needed in a long channel humidifier, and increases the yield of the system by approximately 15%.

6.2. Future work

Over and above the knowledge delivered in this thesis, there is still work to be done in the area in the future. Most importantly, to be able to design a heat and mass transfer device that involves the crossflow interaction of air with falling sheets of water, an understanding of the pressure drop of the airflow across the falling sheets of water is required. This would also enable one to analyse the operational cost of such devices and compare it with other technologies. On this basis, further evaluating the effect of the sheet thickness could be beneficial as it directly affects the Weber number of the water flow and the pressure drop in the air stream.

There is also a need to further develop the flow regime map by performing more visualization experiments, especially around the transition lines. This would provide a more accurate flow regime map. To this end, examination of the flow regimes at different fall heights with different sheet thicknesses could be advantageous.

Additionally, the conditions of the velocity, temperature and concentration boundary layers were not studied in this thesis. This would provide a better understanding of the correlations of heat and mass transfer and the modified Chilton-Colburn analogy.

Finally, concerning the design and development of the components of the simple HDH desalination system, there are still possibilities to improve the yield and efficiency of the system. For instance, design and analysis of a cascading humidifier with multiple air injection could enhance the transfer process by continuously supplying unsaturated air. In such a humidifier, the discharged water can be cooled to the wet bulb temperature of the air stream. This would eliminate the need for the economizer, and consequently the costs of the system can be reduced. Furthermore, developing the solar water heater and the dehumidifier can also improve the fresh water production and the efficiency of the system.

REFERENCES

[1] F. Al-Juwayhel, H. El-Dessouky, H. Ettouney, Analysis of single-effect evaporator desalination systems combined with vapor compression heat pumps, Desalination, 114(3) (1997) 253-275.

[2] G. Al-Enezi, H. Ettouney, N. Fawzy, Low temperature humidification dehumidification desalination process, Energy Conversion and Management, 47(4) (2006) 470-484.

[3] M.A. Shannon, P.W. Bohn, M. Elimelech, J.G. Georgiadis, B.J. Marinas, A.M. Mayes, Science and technology for water purification in the coming decades, Nature, 452(7185) (2008) 301-310.

[4] S.A. Kalogirou, Solar energy engineering: processes and systems, Academic Press, 2013.

[5] A. Bajpayee, T. Luo, A. Muto, G. Chen, Very low temperature membrane-free desalination by directional solvent extraction, Energy & Environmental Science, 4(5) (2011) 1672-1675.

[6] M. Mehanna, T. Saito, J. Yan, M. Hickner, X. Cao, X. Huang, B.E. Logan, Using microbial desalination cells to reduce water salinity prior to reverse osmosis, Energy & Environmental Science, 3(8) (2010) 1114-1120.

[7] O.O. Badran, H.A. Al-Tahaineh, The effect of coupling a flat-plate collector on the solar still productivity, Desalination, 183(1) (2005) 137-142.

[8] T. Arunkumar, K. Vinothkumar, A. Ahsan, R. Jayaprakash, S. Kumar, Experimental study on various solar still designs, ISRN Renewable Energy, 2012 (2012) 1-10.

[9] G.P. Narayan, R.K. McGovern, S.M. Zubair, J.H. Lienhard, High-temperature-steam-driven, varied-pressure, humidification-dehumidification system coupled with reverse osmosis for energy-efficient seawater desalination, Energy, 37(1) (2012) 482-493.

[10] G. Yuan, H. Zhang, Mathematical modeling of a closed circulation solar desalination unit with humidification–dehumidification, Desalination, 205(1) (2007) 156-162.

[11] K. Zhani, H.B. Bacha, Experimental investigation of a new solar desalination prototype using the humidification dehumidification principle, Renewable Energy, 35(11) (2010) 2610-2617.

[12] M. Khamooshi, K. Parham, I. Roozbeh, H. Ensafisoroor, Applications of innovative configurations of double absorption heat transformers in water purification technology, Desalination and Water Treatment, 57(18) (2016) 8204-8216.

[13] H. Ensafisoroor, M. Khamooshi, F. Egelioglu, K. Parham, An experimental comparative study on different configurations of basin solar still, Desalination and Water Treatment, 57(5) (2016) 1901-1916.

[14] M. Khamooshi, K. Parham, F. Egelioglu, M. Yari, H. Salati, Simulation and optimization of novel configurations of triple absorption heat transformers integrated to a water desalination system, Desalination, 348 (2014) 39-48.

[15] M. Al-Sahali, H.M. Ettouney, Humidification dehumidification desalination process: Design and performance evaluation, Chemical Engineering Journal, 143(1) (2008) 257-264.

[16] S. Bouguecha, B. Hamrouni, M. Dhahbi, Desalination and the Environment Small scale desalination pilots powered by renewable energy sources: case studies, Desalination, 183(1) (2005) 151-165.

[17] J. Ayoub, R. Alward, Water requirements and remote arid areas: the need for small-scale desalination, Desalination, 107(2) (1996) 131-147.

[18] G.T. Ward, Possibilities for the utilization of solar energy in underdeveloped rural areas, Agricultural Engineering Branch, Land and Water Development Division, Food and Agriculture Organization of the United Nations, 1961.

[19] E. Mathioulakis, V. Belessiotis, E. Delyannis, Desalination by using alternative energy: Review and state-of-the-art, Desalination, 203(1–3) (2007) 346-365.

[20] M. Shatat, M. Worall, S. Riffat, Opportunities for solar water desalination worldwide: Review, Sustainable Cities and Society, 9 (2013) 67-80.

[21] S. Zhao, L. Zou, C.Y. Tang, D. Mulcahy, Recent developments in forward osmosis: Opportunities and challenges, Journal of Membrane Science, 396 (2012) 1-21.

[22] J.-J. Qin, W.C.L. Lay, K.A. Kekre, Recent developments and future challenges of forward osmosis for desalination: a review, Desalination and Water Treatment, 39(1-3) (2012) 123-136.

[23] C. Li, Y. Goswami, E. Stefanakos, Solar assisted sea water desalination: A review, Renewable and Sustainable Energy Reviews, 19 (2013) 136-163.

[24] I.C. Karagiannis, P.G. Soldatos, Water desalination cost literature: review and assessment, Desalination, 223(1–3) (2008) 448-456.

[25] A. Alkhudhiri, N. Darwish, N. Hilal, Membrane distillation: A comprehensive review, Desalination, 287 (2012) 2-18.

[26] M. Maria Antony Raj, K. Kalidasa Murugavel, T. Rajaseenivasan, K. Srithar, A review on flash evaporation desalination, Desalination and Water Treatment, 57(29) (2016) 13462-13471.

[27] D.M. Warsinger, J. Swaminathan, E. Guillen-Burrieza, H.A. Arafat, Scaling and fouling in membrane distillation for desalination applications: a review, Desalination, 356 (2015) 294-313.

[28] K.S. Spiegler, Salt-water purification, Plenum Press., 1977.

[29] R. Saidur, E.T. Elcevvadi, S. Mekhilef, A. Safari, H.A. Mohammed, An overview of different distillation methods for small scale applications, Renewable and Sustainable Energy Reviews, 15(9) (2011) 4756-4764.

[30] H. Rahman, M. Hawlader, A. Malek, An experiment with a single-effect submerged vertical tube evaporator in multi-effect desalination, Desalination, 156(1) (2003) 91-100.

[31] L.R. Evans, J.E. Miller, Sweeping gas membrane desalination using commercial hydrophobic hollow fiber membranes, SAND2002-0138, January, (2002).

[32] A.D. Khawaji, I.K. Kutubkhanah, J.-M. Wie, Advances in seawater desalination technologies, Desalination, 221(1–3) (2008) 47-69.

[33] M.A. Eltawil, Z. Zhengming, L. Yuan, A review of renewable energy technologies integrated with desalination systems, Renewable and Sustainable Energy Reviews, 13(9) (2009) 2245-2262.

[34] A. Khawaji, J. Wie, T. Khan, Operating experience of the royal commission acid-dosed MSF seawater desalination plant, in: Proceedings of the IDA World Congress on Desalination and Water Reuse, 1997, pp. 3-19.

[35] A. Harris, Sea water chemistry and scale control, Desalination technology development and practice. London: Applied Science Publishers, (1983) 31-56.

[36] M. Darwish, Desalination process: A technical comparison, in: Proceedings of IDA World Congress on Desalination and Water Sciences, Abu Dhabi, United Arab Emirates, 1995, pp. 149-173.

[37] A. Ophir, A. Gendel, G. Kronenberg, The LT-MED process for SW Cogen plants, Desalination Water Reuse, 4(1) (1994) 28-31.

[38] A. Christ, K. Regenauer-Lieb, H.T. Chua, Thermodynamic optimisation of multi effect distillation driven by sensible heat sources, Desalination, 336 (2014) 160-167.

[39] S.C. Maroo, D.Y. Goswami, Theoretical analysis of a single-stage and two-stage solar driven flash desalination system based on passive vacuum generation, Desalination, 249(2) (2009) 635-646.

[40] K. Bourouni, M.T. Chaibi, L. Tadrist, Water desalination by humidification and dehumidification of air: state of the art, Desalination, 137(1) (2001) 167-176.

[41] G.P. Narayan, M.H. Sharqawy, E.K. Summers, J.H. Lienhard, S.M. Zubair, M.A. Antar, The potential of solar-driven humidification–dehumidification desalination for small-scale decentralized water production, Renewable and Sustainable Energy Reviews, 14(4) (2010) 1187-1201.

[42] A. Giwa, N. Akther, A.A. Housani, S. Haris, S.W. Hasan, Recent advances in humidification dehumidification (HDH) desalination processes: Improved designs and productivity, Renewable and Sustainable Energy Reviews, 57 (2016) 929-944.

[43] A.A. Abd-Eltwab, M.S. Abd-Elhady, I.M. El-Moghazy, M.S. Hassan, Experimental Study of Deposits Removal in Thermal Desalination Plants by the Thermal Shock Technique, Heat Transfer Engineering, 37(16) (2016) 1382-1391.

[44] K.M. Chehayeb, G.P. Narayan, S.M. Zubair, J.H. Lienhard, Use of multiple extractions and injections to thermodynamically balance the humidification dehumidification desalination system, International Journal of Heat and Mass Transfer, 68 (2014) 422-434.

[45] M.R. Qtaishat, F. Banat, Desalination by solar powered membrane distillation systems, Desalination, 308 (2013) 186-197.

[46] D. Manolakos, G. Papadakis, S. Kyritsis, K. Bouzianas, Experimental evaluation of an autonomous low-temperature solar Rankine cycle system for reverse osmosis desalination, Desalination, 203(1) (2007) 366-374.

[47] J.C. Bruno, J. Lopez-Villada, E. Letelier, S. Romera, A. Coronas, Modelling and optimisation of solar organic rankine cycle engines for reverse osmosis desalination, Applied Thermal Engineering, 28(17) (2008) 2212-2226.

[48] R.A. Khaydarov, R.R. Khaydarov, Solar powered direct osmosis desalination, Desalination, 217(1) (2007) 225-232.

[49] K.W. Lawson, D.R. Lloyd, Membrane distillation, Journal of Membrane Science, 124(1) (1997) 1-25.

[50] J. Koschikowski, M. Wieghaus, M. Rommel, Solar thermal driven desalination plants based on membrane distillation, Water Science and Technology: Water Supply, 3(5-6) (2003) 49-55.

[51] A. Hanafi, Design and performance of solar MSF desalination systems, Desalination, 82(1-3) (1991) 165-174.

[52] M. Sharaf, A. Nafey, L. García-Rodríguez, Exergy and thermo-economic analyses of a combined solar organic cycle with multi effect distillation (MED) desalination process, Desalination, 272(1) (2011) 135-147.

[53] O. Badran, Experimental study of the enhancement parameters on a single slope solar still productivity, Desalination, 209(1) (2007) 136-143.

[54] B. Chaouchi, A. Zrelli, S. Gabsi, Desalination of brackish water by means of a parabolic solar concentrator, Desalination, 217(1) (2007) 118-126.

[55] C. Yıldırım, İ. Solmuş, A parametric study on a humidification–dehumidification (HDH) desalination unit powered by solar air and water heaters, Energy Conversion and Management, 86 (2014) 568-575.

[56] W. He, D. Han, C. Yue, W. Pu, A parametric study of a humidification dehumidification (HDH) desalination system using low grade heat sources, Energy Conversion and Management, 105 (2015) 929-937.

[57] S.K. Garg, S.D. Gomkale, R.L. Datta, D.S. Datar, Development of humidification-dehumidification technique for water desalination in arid zones of India, Desalination, 5(1) (1968) 55-63.

[58] I. Al-Hayeka, O.O. Badran, The effect of using different designs of solar stills on water distillation, Desalination, 169(2) (2004) 121-127.

[59] H.M. Qiblawey, F. Banat, Solar thermal desalination technologies, Desalination, 220(1) (2008) 633-644.

[60] H.E.S. Fath, A. Ghazy, Solar desalination using humidification—dehumidification technology, Desalination, 142(2) (2002) 119-133.

[61] S. Kalogirou, Survey of solar desalination systems and system selection, Energy, 22(1) (1997) 69-81.

[62] F.A. Al-Sulaiman, M.I. Zubair, M. Atif, P. Gandhidasan, S.A. Al-Dini, M.A. Antar, Humidification dehumidification desalination system using parabolic trough solar air collector, Applied Thermal Engineering, 75 (2015) 809-816.

[63] M. Zamen, S.M. Soufari, S.A. Vahdat, M. Amidpour, M.A. Zeinali, H. Izanloo, H. Aghababaie, Experimental investigation of a two-stage solar humidification–dehumidification desalination process, Desalination, 332(1) (2014) 1-6.

[64] M.S. Mahmoud, T.E. Farrag, W.A. Mohamed, Experimental and theoretical model for water desalination by humidification-dehumidification (HDH), Procedia Environmental Sciences, 17 (2013) 503-512.

[65] S. Al-Hallaj, M.M. Farid, A.R. Tamimi, Solar desalination with a humidification-dehumidification cycle: performance of the unit, Desalination, 120(3) (1998) 273-280.

[66] E.H. Amer, H. Kotb, G.H. Mostafa, A.R. El-Ghalban, Theoretical and experimental investigation of humidification–dehumidification desalination unit, Desalination, 249(3) (2009) 949-959.

[67] Y.J. Dai, H.F. Zhang, Experimental investigation of a solar desalination unit with humidification and dehumidification, Desalination, 130(2) (2000) 169-175.

[68] Y.J. Dai, R.Z. Wang, H.F. Zhang, Parametric analysis to improve the performance of a solar desalination unit with humidification and dehumidification, Desalination, 142(2) (2002) 107-118.

[69] C. Yamalı, İ. Solmus, A solar desalination system using humidification–dehumidification process: experimental study and comparison with the theoretical results, Desalination, 220(1) (2008) 538-551.

[70] G. Yuan, Z. Wang, H. Li, X. Li, Experimental study of a solar desalination system based on humidification–dehumidification process, Desalination, 277(1) (2011) 92-98.

[71] H.B. Bacha, T. Damak, M. Bouzguenda, A. Maalej, Experimental validation of the distillation module of a desalination station using the SMCEC principle, Renewable Energy, 28(15) (2003) 2335-2354.

[72] S. Al-Kharabsheh, D. Yogi, Analysis of an innovative water desalination system using low-grade solar heat, Desalination, 156(1) (2003) 323-332.

[73] R. Manjarrez, M. Galvan, Solar multistage flash evaporation (SMSF) as a solar energy application on desalination processes. Description of one demonstration project, Desalination, 31(1) (1979) 545-554.

[74] S. Hou, D. Zeng, S. Ye, H. Zhang, Exergy analysis of the solar multi-effect humidification–dehumidification desalination process, Desalination, 203(1) (2007) 403-409.

[75] J.A. Duffie, W.A. Beckman, Solar engineering of thermal processes, Wiley New York, 1980.

[76] V.K. Agarwal, D.C. Larson, Calculation of the top loss coefficient of a flat-plate collector, Solar Energy, 27(1) (1981) 69-71.

[77] M. Farid, A.W. Al-Hajaj, Solar desalination with a humidification-dehumidification cycle, Desalination, 106(1) (1996) 427-429.

[78] J. Holman, Heat transfer, 10th ed., McGraw-Hill Higher Education, Boston, 2010.

[79] Y.A. Cengel, Heat and Mass Transfer, 3rd ed., New York: McGraw-Hill, 2007.

[80] T.R. Marrero, E.A. Mason, Gaseous Diffusion Coefficients, Journal of Physical and Chemical Reference Data, 1(1) (1972) 3-118.

[81] T.H. Chilton, A.P. Colburn, Mass Transfer (Absorption) Coefficients Prediction from Data on Heat Transfer and Fluid Friction, Industrial & Engineering Chemistry, 26(11) (1934) 1183-1187.

[82] S.A. Klein, Engineering Equation Solver, in, F-Chart Software, Madison, WI, 2016.

[83] H.F. Johnstone, H.E. Silcox, Gas Absorption and Humidification in Cyclone Spray Towers, Industrial & Engineering Chemistry, 39(7) (1947) 808-817.

[84] F. Dalili, M. Westermark, Design of tubular humidifiers for evaporative gas turbine cycles, in: ASME 1998 International Gas Turbine and Aeroengine Congress and Exhibition, American Society of Mechanical Engineers, Stockholm, Sweden, 1998, pp. 1-8.

[85] Z. Xu, Y. Xiao, Y. Wang, Experimental and theoretical studies on air humidification by a water spray at elevated pressure, Applied Thermal Engineering, 27(14–15) (2007) 2549-2558.

[86] A. El-Shazly, M. El-Gohary, M. Ossman, Performance characteristics of a solar humidification dehumidification unit using packed bed of screens as the humidifier, Desalination and Water Treatment, 16(1-3) (2010) 17-28.

[87] F. Yoshida, T. Tanaka, Air-Water Contact Operations in a Packed Column, Industrial & Engineering Chemistry, 43(6) (1951) 1467-1473.

[88] K.H. Javed, T. Mahmud, E. Purba, Enhancement of Mass Transfer in a Spray Tower Using Swirling Gas Flow, Chemical Engineering Research and Design, 84(6) (2006) 465-477.

[89] C.F. Bonilla, J.R. Mottes, M. Wolf, Air Humidification Coefficients in Spray Towers. Gas-Film Mass Transfer Coefficient at Low Air Velocities for Use in Scrubber Design, Industrial & Engineering Chemistry, 42(12) (1950) 2521-2525.

[90] S. Nori, T. Ishii, Humidification of air with warm water in countercurrent packed beds, Chemical Engineering Science, 37(3) (1982) 487-490.

[91] F. Dalili, Humidification in evaporative power cycles, Royal Institute of Technology Sweden, 2003.

[92] Y. Dai, K. Sumathy, Theoretical study on a cross-flow direct evaporative cooler using honeycomb paper as packing material, Applied thermal engineering, 22(13) (2002) 1417-1430.

[93] R. Kraft, U. Atikol, Pilot project SOLARDESY-solar desalination system with cascading evaporation in northern Cyprus, in: 10th International Conference on Clean Energy (ICCE 2010), Famagusta, Cyprus, 2010.

[94] L.W. Casperson, Fluttering fountains, Journal of Sound and Vibration, 162 (1991) 251-262.

[95] L.W. Casperson, Fluttering fountains: Annular geometry, Journal of Applied Physics, 79 (1996) 1275-1278.

[96] D.L. Chubb, F.D. Calfo, M.W. McConley, M.S. McMasters, A.A. Afjeh, Geometry of thin liquid sheet flows, AIAA Journal, 32 (1994) 1325-1328.

[97] L.D. Luca, Experimental investigation of the global instability of plane sheet flows, Journal of Fluid Mechanics, 399 (1999) 355-376.

[98] P.J. Schmid, D.S. Henningson, On the stability of falling liquid curtain, Journal of Fluid Mechanics, 463 (2002) 163-173.

[99] J.O. Marston, S.T. Thoroddsen, J. Thompson, M.G. Blyth, D. Henry, J. Uddin, Experimental investigation of hysteresis in the break-up of liquid curtains, Chemical Engineering Science, 117 (2014) 248-263.

[100] H. Kyotoh, K. Fujita, K. Nakano, T. Tsuda, Flow of a falling liquid curtain into a pool, Journal of Fluid Mechanics, 741 (2014) 350-376.

[101] A.A. Ibrahim, M.A. Jog, Nonlinear instability of an annular liquid sheet exposed to gas flow, International Journal of Mutiphase Flow, 34 (2008) 674-664.

[102] J. Mazzallon, Z. Dai, G.M. Faeth, Primary breakup of nunturbulent round liquid jets in gas crossflows, Journal of Atomization and Sprays, 9 (1999) 291-312.

[103] J.M. Gordillo, M. Perez-Saborid, Aerodynamic effects in the break-up of liquid jets: on the first wind-induced break-up regime, Journal of Fluid Mechanics, 541 (2005) 1-20.

[104] R. Bolanos-Jimenez, A. Sevilla, C. Gutierrez-Montes, E. Sanmiguel-Rojas, C. Martinez-Bazan, Bubbling and jetting regimes in planar coflowing air-water sheets, Journal of Fluid Mechanics, 668 (2011) 519-542.

[105] C.-L. Ng, R. Snakarakrishnan, K.A. Sallam, Bag breakup of nontirbulent liquid jets in crossflow, International Journal of Multiphase Flow, 34 (2008) 241-259.

[106] D.R. Brown, A study of the behaviour of thin sheet of moving liquid, Journal of Fluid Mechanics, 10 (1961) 297-305.

[107] M. Becerra, M.S. Carvalho, Stability of viscoelastic liquid curtain, Chemical Engineering and Processing: Process Intensification, 50 (2011) 445-449.

[108] P. Spedding, D. Spence, Flow regimes in two-phase gas-liquid flow, International journal of multiphase flow, 19(2) (1993) 245-280.

[109] D. Barnea, O. Shoham, Y. Taitel, Flow pattern transition for vertical downward two phase flow, Chemical Engineering Science, 37(5) (1982) 741-744.

[110] A.A. Kendoush, S.A. Al-Khatab, Experiments on flow characterization in vertical downward two-phase flow, Experimental thermal and fluid science, 9(1) (1994) 34-38.

[111] T. Furukawa, T. Fukano, Effects of liquid viscosity on flow patterns in vertical upward gas–liquid two-phase flow, International Journal of Multiphase Flow, 27(6) (2001) 1109-1126.

[112] D. Metzger, L. Florschuetz, D. Takeuchi, R. Behee, R. Berry, Heat transfer characteristics for inline and staggered arrays of circular jets with crossflow of spent air, Journal of Heat Transfer, 101(3) (1979) 526-531.

[113] M.A. Habib, A.M. Attya, S.A.M. Said, A.I. Eid, A.Z. Aly, Heat transfer characteristics and Nusselt number correlation of turbulent pulsating pipe air flows, Heat and Mass Transfer, 40(3) (2004) 307-318.

[114] S.K. Saini, R.P. Saini, Development of correlations for Nusselt number and friction factor for solar air heater with roughened duct having arc-shaped wire as artificial roughness, Solar Energy, 82(12) (2008) 1118-1130.

[115] A.S. Gbadebo, M.S.A. Said, A.M. Habib, Average Nusselt number correlation in the thermal entrance region of steady and pulsating turbulent pipe flows, Heat and Mass Transfer, 35(5) (1999) 377-381.

[116] T.W. Chung, H. Wu, Mass Transfer Correlation for Dehumidification of Air in a Packed Absorber with an Inverse U-Shaped Tunnel, Separation Science and Technology, 35(10) (2000) 1503-1515.

[117] Y.T. Kang, A. Akisawa, T. Kashiwagi, Experimental correlation of combined heat and mass transfer for NH3–H2O falling film absorption, International Journal of Refrigeration, 22(4) (1999) 250-262.

[118] S.J. Kline, F. McClintock, Describing uncertainties in single-sample experiments, Mechanical Engineering, 75(1) (1953) 3-8.

[119] J.P. Holman, Experimental methods for engineers, 6th ed., McGraw Hill, New York, 1994.

[120] T.S. Chen, F.A. Strobel, Combined Heat and Mass Transfer in Mixed Convection over a Horizontal Flat Plate, Journal of Heat Transfer, 102(3) (1980) 538-543.

[121] B. Kader, A. Yaglom, Heat and mass transfer laws for fully turbulent wall flows, International Journal of Heat and Mass Transfer, 15(12) (1972) 2329-2351.

[122] J. Abraham, E. Sparrow, W. Minkowycz, Internal-flow Nusselt numbers for the low-Reynolds-number end of the laminar-to-turbulent transition regime, International Journal of Heat and Mass Transfer, 54(1) (2011) 584-588.

[123] C.F. Colebrook, T. Blench, H. Chatley, E. Essex, J. Finniecome, G. Lacey, J. Williamson, G. Macdonald, Correspondence. Turbulent flow in pipes, with particular reference to the transition region between the smooth and rough pipe laws.(includes plates), Journal of the Institution of Civil Engineers, 12(8) (1939) 393-422.

[124] E. Buckingham, Model experiments and the forms of empirical equations, Transactions of American Society of Mechanical Engineers 37 (1915) 263-296.

[125] R. Enayatollahi, T. Anderson, R. Nates, Mathematical modeling of a solar powered humidification dehumidification desalination prototype, in: Solar 2014: The 52nd Annual Conference of the Australian Solar Council, Solar 2014 Conference & Expo, Melbourne, 2014.

[126] V.D. Stevanovic, An analytical model for gas absorption in open-channel flow, International Communications in Heat and Mass Transfer, 24 (1997) 1187-1194.

[127] P. Naphon, Study on the heat transfer characteristics of an evaporative cooling tower, International Communications in Heat and Mass Transfer, 32 (2005) 1066-1074.

[128] A. Klimanek, R.A. Biatecki, , Solution of heat and mass transfer in counterflow wet-cooling tower fills, International Communications in Heat and Mass Transfer, 36 (2009) 547–553.

[129] Z. Huang, P. Jiang, Theoretical Analysis and Numerical Simulation of Coupled Relationship of Heat and Mass Transfer Between Air and Desiccant in Liquid Desiccant Dehumidification, in: Proceedings of the 8th International Symposium on Heating, Ventilation and Air Conditioning, Springer, 2014, pp. 829-839.

[130] A. Ali, K. Vafai, A.R.A. Khaled, Analysis of heat and mass transfer between air and falling film in a cross flow configuration, International Journal of Heat and Mass Transfer, 47(4) (2004) 743-755.

[131] Y. Yin, B. Zheng, T. Chen, B. Shao, X. Zhang, Investigation on coupled heat and mass transfer coefficients between compressed air and liquid desiccant in a packed dryer, International Journal of Heat and Mass Transfer, 93 (2016) 1218-1226.

[132] Y. Wu, Simultaneous heat and mass transfer in laminar falling film on the outside of a circular tube, International Journal of Heat and Mass Transfer, 93 (2016) 1089-1099.

[133] D. Bond, M.J. Goldsworthy, V. Wheatley, Numerical investigation of the heat and mass transfer analogy in rarefied gas flows, International Journal of Heat and Mass Transfer, 85 (2015) 971-986.

[134] H.J. Steeman, A. Janssens, M. De Paepe, On the applicability of the heat and mass transfer analogy in indoor air flows, International Journal of Heat and Mass Transfer, 52(5–6) (2009) 1431-1442.

[135] G. Caruso, D. Vitale Di Maio, Heat and mass transfer analogy applied to condensation in the presence of noncondensable gases inside inclined tubes, International Journal of Heat and Mass Transfer, 68 (2014) 401-414.

[136] P.T. Tsilingiris, The application and experimental validation of a heat and mass transfer analogy model for the prediction of mass transfer in solar distillation systems, Applied Thermal Engineering, 50(1) (2013) 422-428.

[137] A.P. Colburn, A method of correlating forced convection heat-transfer data and a comparison with fluid friction, International Journal of Heat and Mass Transfer, 7(12) (1964) 1359-1384.

APPENDICES

Appendix A Uncertainty Analysis

All the thermocouples used in the experiment were T-type thermocouples. These thermocouples were calibrated to a secondary standard, with freezing and boiling point of water at the local pressure, in which the uncertainty of these were determined to be ±0.3 °C which was conservatively taken to be ±0.4 °C. The local pressure was measured using a mercury barometer (*Griffins & sons*).

A PicoLog TC-08 data acquisition system with 8 channels, which was connected to a computer through a USB interface, was used to monitor and log the temperatures.

The humidity and temperature sensors used in this study were, Sensirion SHT71, according to the manufacturer the uncertainty of these sensors is ±0.4 °*C* for the temperature readings and 0.3% for the humidity measurements. A Sensirion EK-H4 evaluation kit, connected to a computer via a USB interface, was used to monitor and log the humidity and temperature of the air stream.

The mass flow rate of water was calibrated by manually measuring the time taken for a known mass of water pass through the nozzle. The standard deviation of the mass flow readings was found to be ±1.4%, which was conservatively taken to be ±3% of the readings. The volumetric flow rate of air was determined as a product of the cross sectional area of the channel and the velocity of air stream, which was determined using a pitot tube and a 2080P Digitron manometer with an accuracy of *0.15%reading+0.15%full scale+1*. For the range of air velocity in this experiment, the

standard deviation of mass flow rate of air from its reading was found to be ±2.4%, which was conservatively taken to be ±4%.

To determine the uncertainty of the coefficients of heat and mass transfer, the method proposed by Kline and McClintock [118], as cited by Holman [119], was used. In this method, the result of the target parameter that we wish to determine the uncertainty of its measurements is a function of the independent variables $x_1, x_2, x_3, \ldots, x_n$, as given in Equation 77.

$$R = R(x_1, x_2, x_3, \ldots, x_n) \tag{77}$$

Knowing the uncertainties in each of these variables ($w_1, w_2, w_3, \ldots, w_n$), the uncertainty of the target parameter (w_R), can be determined from Equation 78.

$$w_R = \left[\left(\frac{\partial R}{\partial x_1} w_1\right)^2 + \left(\frac{\partial R}{\partial x_2} w_2\right)^2 + \cdots + \left(\frac{\partial R}{\partial x_3} w_3\right)^2\right]^{1/2} \tag{78}$$

The coefficient of heat transfer is a function of the convective heat transfer rate, area, film temperature and the inlet temperature of air, as given in Equation 79.

$$h = \frac{\dot{Q}_{conv}}{A(T_f - T_{a,in})} \tag{79}$$

Where the rate of convective heat transfer itself is a function of the mass flow rate of air, enthalpy of the inlet air and the enthalpy of outlet air as given in Equation 80.

$$\dot{Q}_{conv} = \dot{m}_a(\hbar_{a,out} - \hbar_{a,in}) \tag{80}$$

Therefore, the uncertainty of the convective heat transfer rate can be determined by Equation 81.

$$w_{\dot{Q}_{conv}} = \sqrt{\left(\frac{\partial \dot{Q}_{conv}}{\partial \dot{m}_a} w_{\dot{m}_a}\right)^2 + \left(\frac{\partial \dot{Q}_{conv}}{\partial \hbar_{a,out}} w_{\hbar_{a,out}}\right)^2 + \left(\frac{\partial \dot{Q}_{conv}}{\partial \hbar_{a,in}} w_{\hbar_{a,in}}\right)^2} \tag{81}$$

Where:

$$\frac{\partial \dot{Q}_{conv}}{\partial \dot{m}_a} = \left(\hbar_{a,out} - \hbar_{a,in}\right)$$

$$\frac{\partial \dot{Q}_{conv}}{\partial \hbar_{a,out}} = \dot{m}_a$$

$$\frac{\partial \dot{Q}_{conv}}{\partial \hbar_{a,in}} = -\dot{m}_a$$

Substituting the values of the measurements and the associated uncertainty of each of them, the uncertainty associated with the rate of convective heat transfer is found to be 13%. Where 93.96% of this uncertainty is due to the uncertainty of the temperature readings, 2.47% is due to humidity readings and 3.58% is due to air velocity measurements.

Similarly, the uncertainty of the coefficient of convective heat transfer can be estimated from Equation 82.

$$w_h = \sqrt{\left(\frac{\partial h}{\partial \dot{Q}_{conv}} w_{\dot{Q}_{conv}}\right)^2 + \left(\frac{\partial h}{\partial T_f} w_{T_f}\right)^2 + \left(\frac{\partial h}{\partial T_{a,in}} w_{T_{a,in}}\right)^2} \quad (82)$$

Substituting the measured values and their uncertainties, results in an uncertainty of 12%. Where 93.3% of this uncertainty is due to temperature measurements and 2.74% is due to humidity measurements and 3.96% is due to uncertainty of air velocity measurements.

On the mass transfer side, the coefficient of mass transfer, as given in Equation 83, is a function of the evaporation mass flow rate, area and vapour densities at film and free stream conditions.

$$j = \frac{\dot{m}_{ev}}{A(\rho_{v,f} - \rho_{v,\infty})} \quad (83)$$

Where the rate of evaporation is a function of mass flow rate of air and specific humidity of air before and after contact with the water stream, as given in Equation 84.

$$\dot{m}_{ev} = \dot{m}_a(\omega_{a,out} - \omega_{a,in}) \quad (84)$$

Therefore, the uncertainty in the evaporation rate can be calculated from Equation 85.

$$w_{\dot{m}_{ev}} = \sqrt{\left(\frac{\partial \dot{m}_{ev}}{\partial \dot{m}_a} w_{\dot{m}_a}\right)^2 + \left(\frac{\partial \dot{m}_{ev}}{\partial \omega_{a,out}} w_{\omega_{a,out}}\right)^2 + \left(\frac{\partial \dot{m}_{ev}}{\partial T_{\omega_{a,in}}} w_{T_{\omega_{a,in}}}\right)^2} \quad (85)$$

Which results in an uncertainty of 9% in the evaporation rate.

The uncertainty of the mass transfer coefficient can be determined from Equation 86.

$$w_j = \sqrt{\left(\frac{\partial j}{\partial \dot{m}_{ev}} w_{\dot{m}_{ev}}\right)^2 + \left(\frac{\partial j}{\partial \rho_{v,f}} w_{\rho_{v,f}}\right)^2 + \left(\frac{\partial j}{\partial \rho_{v,\infty}} w_{\rho_{v,\infty}}\right)^2} \tag{86}$$

This, results in an uncertainty of 10%, where 49.49% of this uncertainty is due to temperature readings, 44.54% is due to humidity readings and 5.97% is due to air velocity measurements.

Appendix B Dimensional Analysis

This appendix details the formulations of heat and mass transfer processes into dimensionless terms. The Nusselt and Sherwood numbers are the representative dimensionless number to describe the heat and mass transfer phenomenon, respectively. For many of simple forced convection processes, the Nusselt number is a function of the Reynolds number and the Prandtl number as given in Equation 87 [79], whereas the Sherwood number is governed by the Reynolds and Schmidt numbers, as given in Equation 88 [79].

$$Nu = f(Re, Pr) \tag{87}$$

$$Sh = f(Re, Sc) \tag{88}$$

In circumstances where the thermal and concentration boundary conditions are of the same type, the functional form of *f* is similar for both Nusselt and Sherwood numbers [79] and varies for different conditions. In this regard, many investigations have been performed to ascertain the functional forms of the Nusselt number with respect to the Reynolds and Prandtl numbers, and also the Sherwood number as a function of the Reynolds and Schmidt numbers in simple geometries [120-123]. In more complex geometries however, the Nusselt number might be governed by some other dimensionless groups in addition to the Reynolds and Prandtl numbers, and similarly the Sherwood number might be defined with some other dimensionless groups besides the Reynolds and Schmidt numbers. In order to develop the generalised correlations of heat and mass transfer, the dimensionless groups that describe the system are identified using the Buckingham π theorem [124]. This theorem states that a physically meaningful equation, which involves "*n*" number of physical variables with "*m*" number of basic physical unit,

exists, in which this equation can be rewritten in terms of "*n* - *m*" number of dimensionless groups that are made from the physical variables. It was noted that for the low temperature evaporation processes in a cascading crossflow configuration, the physical variables that best describe the problem are the air velocity, characteristic length, enthalpy of evaporation, thermal conductivity of air, density of air, viscosity of air, specific heat of air, rate of diffusion, enthalpy content of air stream at film condition and temperature difference between two phases. Such that a general relation as given in Equation 89 can be formed.

$$f\left(\rho_a, k_{a,} V_{ch}, L_{ch}, h, , \mu_a, c_{p_a}, \Delta T, \lambda_{a-w}, j, \hbar_f, \hbar_{fg}\right) = 0 \tag{89}$$

Where *f* is an unknown function. The dimensions of these variable are listed in Table 12, based on four basic physical units of mass (*M*), temperature (*T*), time (*t*) and length (*L*).

Table 12. Dimensions of variables

Variable	Dimension	Variable	Dimension	Variable	Dimension
k_a	$M.L.t^{-3}.T^{-1}$	$L_{ch,a}$	L	ΔT	T
ρ_a	$M.L^{-3}$	h	$M.t^{-3}.T^{-1}$	$\hbar_{fg}$	$L^2.t^{-2}$
μ_a	$M.L^{-1}.t^{-1}$	cp_a	$L^2.t^{-2}.T^{-1}$	V_a	$L.t^{-1}$
j	$L.t^{-1}$	λ_{a-w}	$L^2.t^{-1}$	$\hbar_f$	$L^2.t^{-2}$

As there are twelve quantities and four basic units, according to the Buckingham π theorem, eight dimensionless groups can be predicted. Thus, Equation 89 can be rewritten as Equation 90.

$$f'(\pi_1, \pi_2, \pi_3, \pi_4, \pi_5, \pi_6, \pi_{7,} \pi_8) = 0 \tag{90}$$

Where f' is also an unknown function. Choosing the air density, thermal conductivity, characteristic length and characteristic velocity as the repeating parameters, the first original independent dimensionless groups, which must include the heat transfer coefficient as well as repeating parameters, can be represented as Equation 91:

$$\pi_1 = {\rho_a}^a {k_a}^b {L_{ch}}^c {V_{ch}}^d h \tag{91}$$

Where the exponents of each physical variable represent the exponent of the corresponding variable such that the result is a dimensionless group. Therefore, substituting the units of each physical variable in Equation 91, Equation 92 can be achieved.

$$\pi_1 = (M.L^{-3})^a (M.L.t^{-3}T^{-1})^b (L)^c (L.t^{-1})^d (Mt^{-3}T^{-1}) \tag{92}$$

Solving for each of the basic units, a set of equation can be constructed as given in Equation 93.

$$\begin{matrix} for\ M: \\ for\ t: \\ for\ L: \\ for\ T: \end{matrix} \begin{cases} a + b + 1 = 0 \\ -3b - d - 3 = 0 \\ -3a + b + c + d = 0 \\ -b - 1 = 0 \end{cases} \tag{93}$$

Solving these equations simultaneously will result in:

$$\begin{cases} a = 0 \\ b = -1 \\ c = 1 \\ d = 0 \end{cases}$$

Therefore, substituting these exponents in Equation 91, π_1 can be determined from Equation 94.

$$\pi_1 = {\rho_a}^0 {k_a}^{-1} {L_{ch}}^1 {V_{ch}}^0 h = \frac{L_{ch} h}{k_a} \tag{94}$$

In the same way, the other dimensionless groups were determined, as shown in Table 13.

Table 13. Independent dimensionless groups

$\pi_1 = \frac{L_{ch} h}{k_a}$	$\pi_3 = \frac{\rho_a V_{ch} L_{ch} cp_a}{k_a}$	$\pi_5 = \frac{\lambda_{a-w}}{V_{ch} L_{ch}}$	$\pi_7 = \frac{\hbar_{fg}}{{V_{ch}}^2}$
$\pi_2 = \frac{\mu_a}{\rho_a V_{ch} L_{ch}}$	$\pi_4 = \frac{k_a \Delta T}{\rho_a {V_{ch}}^3 L_{ch}}$	$\pi_6 = \frac{j}{V_{ch}}$	$\pi_8 = \frac{\hbar_f}{{V_{ch}}^2}$

The dimensionless groups from the Buckingham π theorem can be presented individually or can be combined to form other dimensionless groups. The first dimensionless number, π_1, is the Nusselt number (*Nu*) or the ratio of convective to conductive heat transfer coefficients, and in a forced convection process expresses the dimensionless thermal transference. π_2^{-1} is the Reynolds number (*Re*) which is the ratio of fluid inertia to viscous forces and in forced convection heat transfer processes characterises the role of advection. π_3 is the Peclet number (*Pe*) which is the ratio of heat transferred by advection to that transferred by conduction and characterises the convective-diffusive heat transfer processes. π_5^{-1} is the Bodenstein (*Bd*) or mass Peclet (Pe_m) number, which expresses the mass transfer rate by forced convection to the diffusive mass transfer rate and characterizes the convective-diffusive mass transfer processes. π_7^{-1} is the Evaporation number (N_{ev}), which is the ratio of the kinetic energy of the flow to the fluid latent heat of evaporation and characterises the role of kinetic energy of the bulk fluid in providing the heat of evaporation.

The product of π_6 and π_5^{-1} forms the Sherwood number given in Equation 95, which is the equivalent of the Nusselt number in mass transfer.

$$\frac{\pi_6}{\pi_5} = \frac{j}{V_{ch}} \frac{V_{ch} L_{ch}}{\lambda_{a-w}} = \frac{j L_{ch}}{\lambda_{a-w}} = Sh \tag{95}$$

As shown in Equation 96, the product of π_2 and π_3 delivers the Prandtl number (*Pr*), which is the ratio of viscous diffusion to thermal diffusion and characterises the physical properties of the fluid with convective and diffusive heat transfer.

$$\pi_2 \pi_3 = \frac{\mu_a}{\rho_a V_{ch} L_{ch}} \frac{\rho_a V_{ch} L_{ch} cp_a}{k_a} = \frac{cp_a \mu_a}{k_a} = \frac{\nu_a}{\alpha} = Pr \tag{96}$$

Similarly, in Equation 97, the product of π_2 and π_5^{-1} gives the Schmidt number (*Sc*), which is the ratio of viscous diffusion to mass diffusion and characterises the relation between mass and momentum transfer in mass transfer processes.

$$\frac{\pi_2}{\pi_5} = \frac{\mu_a}{\rho_a V_{ch} L_{ch}} \frac{V_{ch} L_{ch}}{\lambda_{a-w}} = \frac{\mu_a}{\rho_a \lambda_{a-w}} = \frac{\nu_a}{\lambda_{a-w}} = Sc \tag{97}$$

The product of π_2, π_3, π_7 and π_8^{-1}, as given in Equation 98 has resulted in another dimensionless group, here called the Prandtl Number of Evaporation (Pr_{ev}).

$$Pr_{ev} = \frac{\pi_2 \pi_3 \pi_7}{\pi_8} = \frac{\frac{\mu_a}{\rho_a V_{ch} L_{ch}} \frac{\rho_a V_{ch} L_{ch} cp_a}{k_a} \frac{\hbar_{fg}}{{V_{ch}}^2}}{\frac{\hbar_f}{{V_{ch}}^2}} = \frac{cp_a \, \mu_a}{k_a} \frac{\hbar_{fg}}{\hbar_f} = Pr \frac{\hbar_{fg}}{\hbar_f} \tag{98}$$

The Prandtl Number of Evaporation expresses the ratio of viscous diffusion to thermal diffusion relative to the enthalpy of vaporization and the enthalpy content of the air stream at film conditions. Hence, higher values indicate that viscous diffusion is the dominant mechanism. This number characterizes low temperature evaporation processes where the enthalpy of evaporation is significantly higher than that delivered to the system.

The Schmidt number is the equivalent of the Prandtl number in mass transfer, therefore we can replace the Prandtl number with the Schmidt number in Equation 98 to determine the Schmidt Number of Evaporation, given in Equation 99.

$$Sc_{ev} = Sc\frac{\hbar_{fg}}{\hbar_f} \tag{99}$$

The Schmidt Number of Evaporation can also be derived from the Buckingham π theorem by combing π_2, π_5, π_7 and π_8 as given in Equation 100.

$$Sc_{ev} = \frac{\pi_2\pi_7}{\pi_5\pi_8} = \frac{\frac{\mu_a}{\rho_a V_{ch} L_{ch}}\frac{\hbar_{fg}}{V_a{}^2}}{\frac{\lambda_{a-w}}{V_{ch}L_{ch}}\frac{\hbar_f}{V_a{}^2}} = \frac{\mu_a}{\rho_a\lambda_{a-w}} = \frac{\nu_a}{\lambda_{a-w}}\frac{\hbar_{fg}}{\hbar_f} \tag{100}$$

The Schmidt Number of Evaporation expresses the ratio of viscous diffusion over the mass diffusion with respect to the required heat of evaporation and the enthalpy content of the bulk stream at the film conditions. This number characterises the mass transfer in a low temperature evaporation process.

Finally, combination of π_2, π_4 and π_7 will form a new dimensionless group, here called Omega (Ω), as given in Equation 101.

$$\frac{\pi_2\pi_7}{\pi_4} = \frac{\frac{\mu_a}{\rho_a V_{ch} L_{ch}} \frac{\hbar_{fg}}{V_a{}^2}}{\frac{k_a \Delta T}{\rho_a V_{ch}{}^3 L_{ch}}} = \frac{\mu_a \hbar_{fg}}{k_a \Delta T} = \Omega \tag{101}$$

This dimensionless group characterises the role of convective heat transfer in providing the latent heat of vaporization, relative to the conductive heat transfer. Such that the higher values indicate that the convective heat transfer dominates. This dimensionless group is also the product of the Prandtl and Jakob numbers.

Appendix C Analysis of the Heat and Mass Transfer Analogy

This appendix details the use of the experimental results to determine the correlation between the heat transfer and the mass transfer, in a crossflow configuration in which a ducted airflow passes through a planar water jet. The Buckingham-π theorem was applied to this process to identify critical dimensionless groups. From this, a modified version of the Chilton-Colburn analogy is developed between the coefficient of total heat transfer and the mass transfer coefficient.

C.1 Introduction

Heat and mass transfer devices involving a liquid interacting with a gas flow have a wide range of applications including distillation plants, cooling towers, aeration processes and desiccant drying [125-129]. Many studies have been made to characterise the heat and mass transfer in such configurations [112, 130-132]. The mechanisms of heat and mass transfer are similar and analogical. Therefore, in some cases where, either the heat or mass transfer data are not reliable or may not be available, the heat and mass transfer analogy can be used to determine the missing or unreliable set of data. In this regards, the Reynolds analogy is the simplest correlation and is applicable only for the special case where the Prandtl and Schmidt numbers are both equal to unity. Chilton and Colburn in 1934 [81] introduced a correlation to predict the coefficient of mass transfer from the experimental data of heat transfer and fluid friction, which is applicable for fully developed flow inside the tubes or between parallel plates with; $0.6 < \text{Prandtl} < 60$ and $0.6 < \text{Schmidt} < 3000$.

However, both of these analogies characterise the “convectional” transport phenomena and may not be applicable for some special cases and geometries. Therefore,

a number of studies have examined the applicability of these analogies to other configurations [133-135]. Steeman et al. [134] employed CFD to investigate the validity of the heat and mass transfer analogy for a particular case of indoor airflows and when the analogy conditions are not met. Similarly, Tsilingiris [136] experimentally developed a heat and mass transfer analogy model in solar distillation systems based on the Chilton-Colburn analogy.

This study investigates the analogy between the intensities of heat and mass transfer in low temperature evaporation processes with crossflow configuration, in which a ducted stream of air passes through a falling sheet of water.

C.2 Experimental Setup

In this experiment, a planar jet of water was directed across a ducted crossing airflow, as shown in Figure 66. A water tank with adjustable height was used to provide a constant pressure head to drive the water flow at different flow rates and a variable speed fan was employed to drive airflow at various steady flow rates. The flow rates of water were determined by measuring the time taken for a known volume of water to pass through the nozzle, and the exact airflow rate was determined from measurements made using a pitot static probe traversed across the duct and a differential manometer.

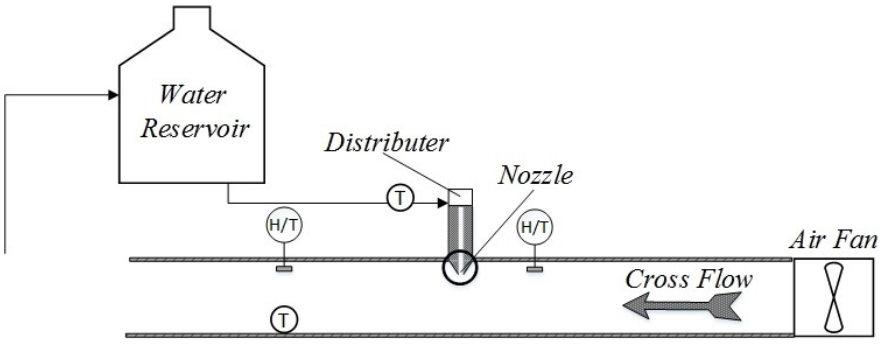

Figure 66. Experimental apparatus

In order to measure the humidity and temperature, a set of 3 humidity/temperature sensors, (Sensirion SHT71) with an accuracy of ±3% for humidity and ±0.3°*C* temperature at standard room condition were used. Two sensors were placed across the sheet measuring the change in humidity and temperature of the air stream as it crossed the water sheet, as seen in Figure 66. A third sensor was placed outside the experiment to monitor the room conditions. A set of two thermocouples (type T) with an accuracy of ±0.3 °*C*were used to record the water temperature before and after contact with the air stream. An auxiliary water heater was used to maintain the inlet water temperature at a constant temperature.

C.3 Dimensional analysis

The Buckingham-π theorem was employed in order to define the dimensionless parameters describing the heat and mass transfer phenomenon in this crossflow configuration. It was considered that the air velocity, characteristic length, enthalpy of evaporation, thermal conductivity of air, density of air, viscosity of air, specific heat of air, rate of diffusion, the enthalpy content of air stream at film conditions and temperature difference between two phases are the describing variable for heat and mass transfer, such that a general relation as given in Equation 89, which is repeated in Equation 102, can be formed.

$$f\left(\rho_a, k_{a,} V_{ch}, L_{ch}, h, , \mu_a, c_{p_a}, \Delta T, \lambda_{a-w}, j, \hbar_f, \hbar_{fg}\right) = 0 \qquad (102)$$

Where *f* is an unknown function. The dimensions of these variable are based on four basic physical units of mass (M), temperature (T), time (t) and length (L).

As there are twelve quantities and four basic units, according to Buckingham-π theorem [124], eight dimensionless groups can be predicted, as shown in Equation 90, which is repeated in Equation 103.

$$f'(\pi_1, \pi_2, \pi_3, \pi_4, \pi_5, \pi_6, \pi_7, \pi_8) = 0 \tag{103}$$

Where f' is also an unknown function. Choosing ρ_a, k_a, V_a and L_a as the repeating parameters, the eight independent dimensionless group can be determined as given in Table 13, which are presented again in Table 14.

Table 14. Independent dimensionless groups

$\pi_1 = \frac{L_{ch}h}{k_a}$	$\pi_3 = \frac{\rho_a V_{ch} L_{ch} cp_a}{k_a}$	$\pi_5 = \frac{\lambda_{a-w}}{V_{ch} L_{ch}}$	$\pi_7 = \frac{\hbar_{fg}}{{V_{ch}}^2}$
$\pi_2 = \frac{\mu_a}{\rho_a V_{ch} L_{ch}}$	$\pi_4 = \frac{k_a \Delta T}{\rho_a {V_{ch}}^3 L_{ch}}$	$\pi_6 = \frac{j}{V_{ch}}$	$\pi_8 = \frac{\hbar_f}{{V_{ch}}^2}$

Where, π_1 is the Nusselt number (*Nu*) and product of π_6 and π_5^{-1} forms the Sherwood number (*Sh*), π_2^{-1} is the Reynolds number (Re), π_3 is the Peclet number (*Pe*) and π_7^{-1} is the Evaporation number (N_{ev}). Grouping π_2 and π_3 delivers the Prandtl number (*Pr*) and combination of π_2 and π_5 gives the Schmidt number (*Sc*). The Lewis number (*Le*) can also be determined as a ratio of Prandtl to Schmidt number, which is the ratio of thermal to mass diffusivity. The Buckingham π analysis is detailed in Appendix B.

C.4 Testing the Chilton-Colburn Analogy

The total rate of heat transfer ($\dot{Q}_t$) is the sum of convective, evaporative and radiative rates of heat transfer. Assuming that the radiation heat transfer is negligible this can be determined from Equation 104.

$$\dot{Q}_t = \dot{Q}_{conv} + \dot{Q}_{ev} = \dot{m}_a(\hbar_{a,o} - \hbar_{a,i}) \quad (104)$$

Where $\dot{Q}_{cv}$ is the convective rate of heat transfer and $\dot{Q}_{ev}$ is the rate of heat transfer through evaporation. $\dot{m}_a$ is the mass flow rate of air and $\hbar_{a,i}$ and $\hbar_{a,o}$ are the enthalpies of the air at the inlet and outlet conditions, respectively. The rate of evaporation can be determined from Equation 105.

$$\dot{Q}_{ev} = \dot{m}_{ev}\hbar_{fg} \quad (105)$$

Where $\hbar_{fg}$ is the enthalpy of vaporization and $\dot{m}_{ev}$ is the rate of evaporation, which can be calculated by measuring the specific humidity (ω) of air at inlet and outlet conditions and the mass flow rate of the air stream as given in Equation 106.

$$\dot{m}_{ev} = \dot{m}_a(\omega_{a,out} - \omega_{a,in}) \quad (106)$$

On the mass transfer side, the experimental value of the coefficient of mass transfer can be determined from Equation 107.

$$j = \frac{\dot{m}_{ev}}{A_{c,a}(\rho_{v,f} - \rho_{v,b})} \quad (107)$$

Where, $\rho_{v,\infty}$ is the density of vapour at the free stream conditions and $\rho_{v,f}$ is the vapour density at film condition, which is considered to be saturated air at the average temperature of the two phases.

The experimental value of the coefficient of convective heat transfer can be calculated from Equation 108.

$$h = \frac{\dot{Q}_{conv}}{A_{c,a}(T_f - T_\infty)} \tag{108}$$

Where $A_{c,a}$ is the cross sectional area of air stream, T_∞ is the bulk stream temperature and T_f is the film temperature. The convective heat transfer rate can be determined from Equation 104.

The existence of an analogy was first assessed by examining the relationship between the heat transfer coefficient determined from Equation 108 and the mass transfer coefficient calculated by Equation 107, as shown in Figure 67.

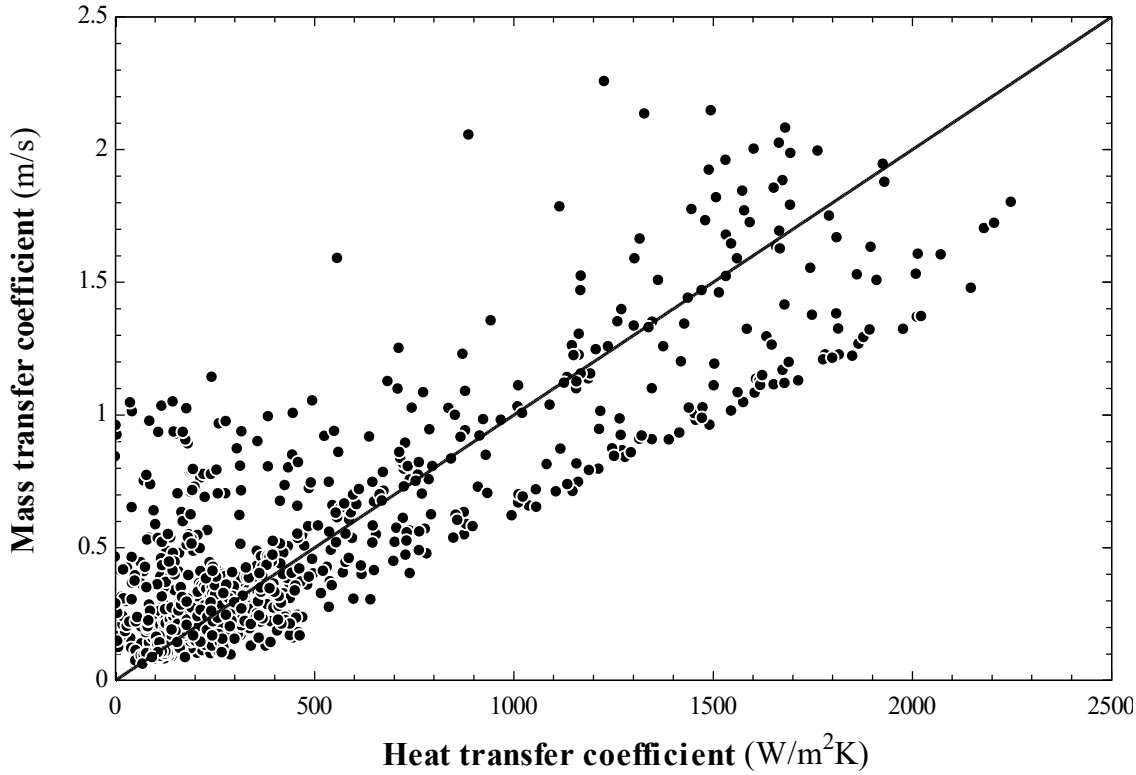

Figure 67. The experimental values of convective heat transfer coefficient versus experimental values of mass transfer coefficient

As seen in Figure 67, the experimental values of the heat and mass transfer coefficients are correlated with a reasonable accuracy, with a coefficient of determination (R^2) of 0.72. The heat and mass transfer are analogues, in circumstances where the thermal and concentration boundary layers are of the same type [79]. For the conditions tested by Chilton and Colburn, the empirical correlations of Nusselt and Sherwood numbers were determined as given in Equations 109 and 110 [137].

$$Nu = a\, Re^{m}\, Pr^{1/3} \tag{109}$$

$$Sh = a\, Re^{m}\, Sc^{1/3} \tag{110}$$

Based on the Reynolds analogy the heat transfer Stanton number is equivalent to the mass transfer Stanton number. Where the heat transfer Stanton number is the ratio of the Nusselt number to the product of the Reynolds and Prandtl numbers, and the mass transfer Stanton number is the ratio of the Sherwood number to the product of the Reynolds and Schmidt numbers, as given in Equations 111 and 112 [79].

$$St_{heat} = \frac{h}{\rho V c_p} = \frac{Nu}{Re\, Pr} \tag{111}$$

$$St_{mass} = \frac{j}{V} = \frac{Sh}{Re\, Sc} \tag{112}$$

Now, substituting the empirical correlation for the Nusselt and Sherwood numbers, results in Equations 113 and 114.

$$St_{heat} = \frac{h}{\rho V c_p} = \frac{a\, Re^m\, Pr^{1/3}}{Re\, Pr} \tag{113}$$

$$St_{mass} = \frac{j}{V} = \frac{a\, Re^m\, Sc^{1/3}}{Re\, Sc} \tag{114}$$

From these, Chilton and Colburn had derived a "*J*" factor for heat and mass transfer as given in Equations 115 and 116 [81].

$$J_{heat} = a\, Re^{m-1} = \frac{h}{\rho V c_p}\, Pr^{2/3} \tag{115}$$

$$J_{mass} = a\, Re^{m-1} = \frac{j}{V}\, Sc^{2/3} \tag{116}$$

Since the "*J*" factor is equal for both heat and mass transfer, the Chilton-Colburn analogy was determined as given in Equation 117 [81].

$$\frac{h}{\rho V c_p}\, Pr^{\frac{2}{3}} = \frac{j}{V}\, Sc^{\frac{2}{3}}$$

or
$$\frac{h}{j} = \rho c_p \left(\frac{Sc}{Pr}\right)^{2/3} = \rho c_p\, Le^{2/3} \tag{117}$$

As mentioned earlier the Chilton-Colburn analogy, seen in Equation 117, is valid for a fully developed flow inside a pipe, and for flow parallel to plane surfaces, when 0.6 < Prandtl <60 and 0.6 < Schmidt <3000.

The applicability of the Chilton-Colburn analogy to other configurations and conditions may be validated for the particular geometry and conditions of the experiment.

Figure 68 shows the experimental values of the convection heat transfer coefficient from Equation 108 compared to the calculated value from the Chilton-Colburn analogy, given in Equation 117 using the experimental mass transfer data. This figure shows some correlation for predicting the heat transfer coefficient from the mass transfer data, but with quite a large scatter.

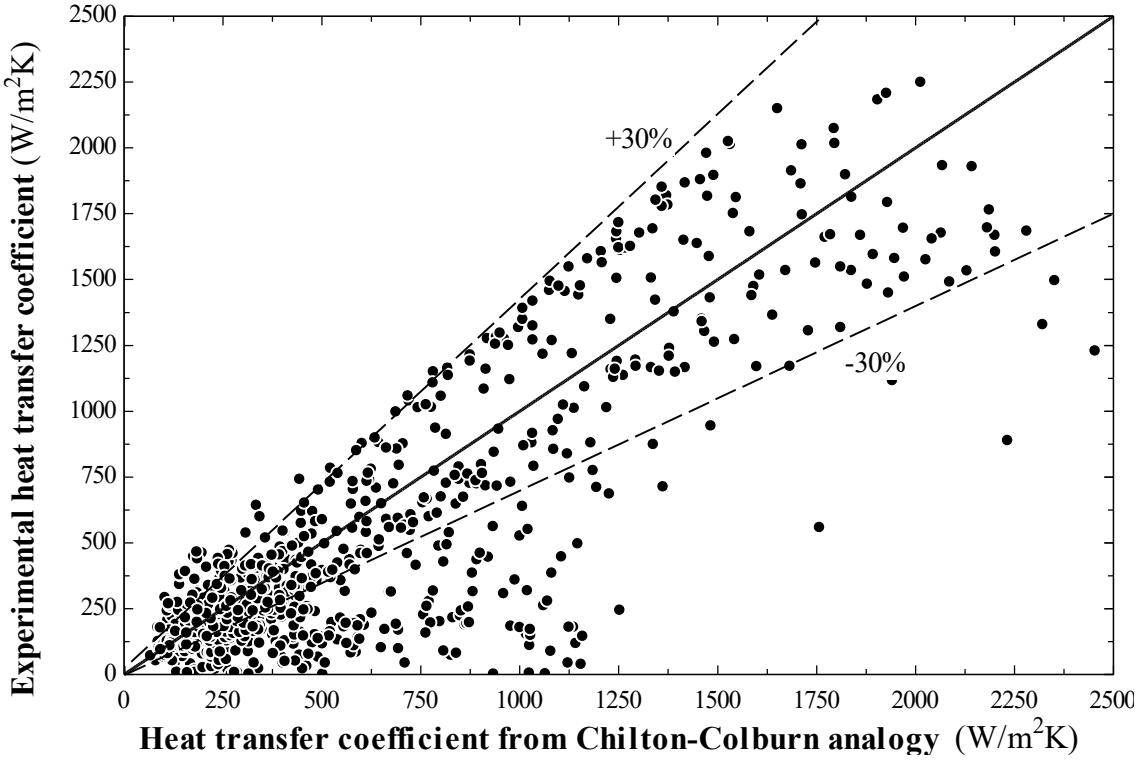

Figure 68. Comparison of experimental heat transfer coefficient with the calculated values from the Chilton-Colburn analogy

From this, it could be considered that, the Chilton-Colburn analogy is reasonably valid for these geometries and conditions. However, considering that in low temperature evaporation processes a considerable fraction of the supplied energy will be consumed to overcome the latent heat of vaporization, it is reasonable to expect that the relationship between heat and mass transfer should account for this. Therefore, this work aims to find

an analogy between the overall heat transfer coefficient and mass transfer coefficient, in that it accounts for both convection and evaporation.

C.5 Analogy between the Coefficient of Total Heat Transfer and Mass Transfer Coefficient

As mentioned earlier, the Chilton-Colburn analogy characterises only the convectional transfer phenomenon. Since in low temperature evaporation processes a significant fraction of the entire heat transfer is through evaporation, it is logical to present a correlation to predict the overall heat transfer coefficient from the mass transfer data. In this respect, the experimental value of the overall heat transfer coefficient can be calculated by substituting $\dot{Q}_{cv}$ in Equation 108 with $\dot{Q}_t$ as shown in Equation 118.

$$h_t = \frac{\dot{Q}_t}{A_{c,a}(T_f - T_\infty)} \tag{118}$$

In order to assess the existence of any analogy between the coefficient of total heat transfer and the mass transfer coefficient, the calculated values from Equation 118 were plotted against the experimental values of mass transfer coefficient from Equation 107, as shown in Figure 69.

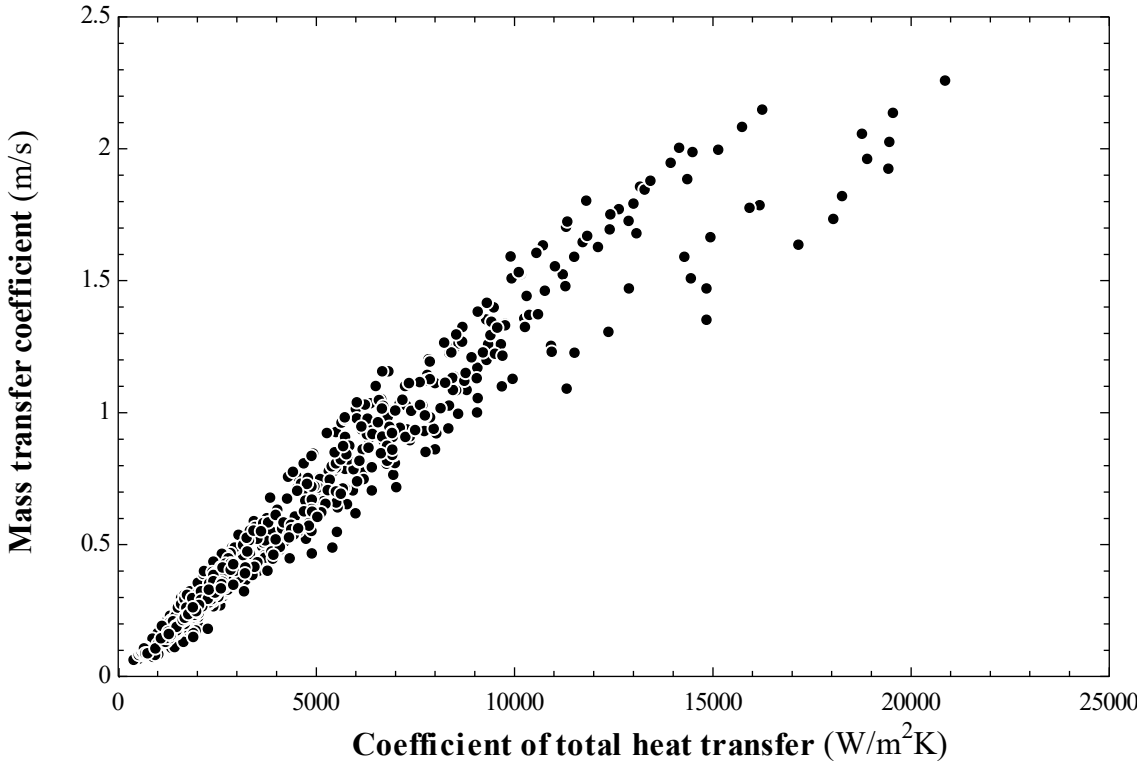

Figure 69. The coefficent total heat transfer versus the mass transfer coefficient

In Figure 69, it can be seen that the mass transfer coefficient is analogous with the coefficient of total heat transfer with a coefficient of determination (R^2) of 0.95. This is a far better correlation than that seen previously in Figure 67.

On this basis, the overall heat transfer coefficient can be expressed as a function of the density and the specific heat of the air stream as well as the dimensionless groups derived from the Buckingham π theorem, as given in Equation 119.

$$h_t = j\,\rho\,c_p \times Pe^b Bd^c\,{\pi_4}^d {\pi_7}^e {\pi_8}^f \tag{119}$$

In order to define the exponent of the dimensionless groups in Equation 119, the least squares analysis was performed, resulting in Equation 120.

$$h_t = j\,\rho\,c_p \times Pe^{-0.575} Bd^{0.575}\,{\pi_4}^{0.00012} {\pi_7}^{0.575} {\pi_8}^{-0.575} \tag{120}$$

The exponents of the Peclet and Bodenstein numbers are identical but with different sign and therefore, can be presented in a fractional form. As mentioned earlier the Bodenstein is the product of the Reynolds and Schmidt numbers and similarly, the Peclet number is the product of the Reynolds and Prandtl numbers. Therefore, the ratio of Bodenstein to Peclet numbers is in fact the ratio of Schmidt to Prandtl number, or the Lewis number (Le), as given in Equation 121.

$$\frac{Bd}{Pe} = \frac{Re\ Sc}{Re\ Pr} = \frac{Sc}{Pr} = Le \tag{121}$$

Similarly, the exponents of π_7 and π_8 are identical with opposite sign and can be presented in a fractional form, as given in Equation 122.

$$\frac{\pi_7}{\pi_8} = \frac{\hbar_{fg}/{V_{ch}}^2}{\hbar_f/{V_{ch}}^2} = \frac{\hbar_{fg}}{\hbar_f} \tag{122}$$

The ratio of π_7 to π_8 is in fact the ratio of enthalpy of vaporization to the enthalpy content of the air stream at the film conditions, which in this context is referred to as the enthalpy ratio. The enthalpy ratio characterises the low temperature evaporation processes with respect to required heat of evaporation and the energy supplied by the bulk stream.

It can be seen that the exponents of the Lewis number and the enthalpy ratio are equal and hence, Equation 120 can now be rewritten as Equation 123.

$$h_t = j\rho_a c_{p_a} \left(Le \frac{\hbar_{fg}}{\hbar_f} \right)^{0.575} \tag{123}$$

The product of Lewis number and the enthalpy ratio can be referred to as the Lewis Number of Evaporation (Le_{ev}) and Equation 123 can be rewritten as Equation 124.

$$h_t = j\rho_a c_{p_a} Le_{ev}{}^{0.575} \tag{124}$$

Shown in Figure 70 is the coefficient of total heat transfer calculated by Equation 124 versus the experimental values calculated from Equation 118.

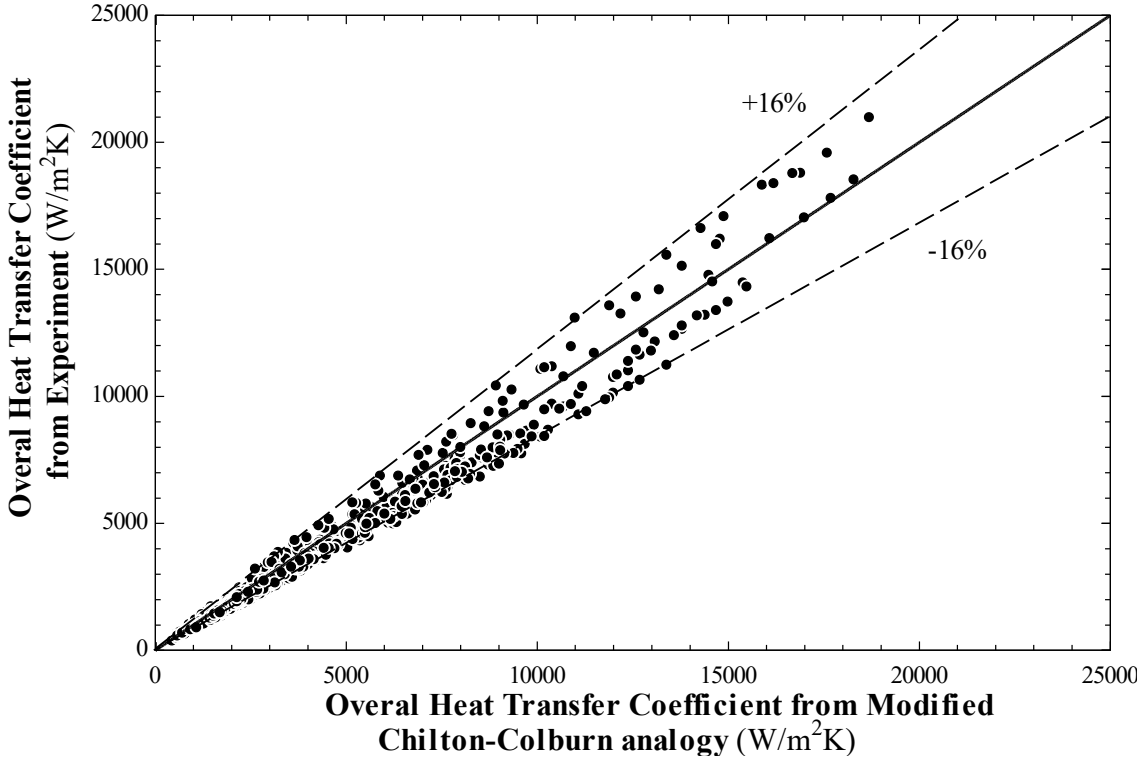

Figure 70. Corrected Chilton-Colburn Analogy for heat and mass transfer with phase change

This figure clearly shows a much stronger correlation, with a coefficient of determination (R^2) of 0.98, when accounting for the phase change process.

C.6 Conclusion

An experimental study was performed in order to examine the relationship between heat and mass transfer coefficients in a low temperature crossflow evaporation process. In this regard, the Buckingham-π theorem as well as the least squares analysis were employed. Eight dimensionless group were determined from the Buckingham-π analysis. Performing the least squares analysis on these dimensionless parameters, showed a strong correlation between the overall heat transfer coefficient and the Lewis Number of Evaporation. This led to the correlation of a modified Chilton-Colburn analogy that includes the Lewis Number of Evaporation to account for the low temperature evaporation processes. As a result of this work, the heat and mass transfer can now be quantified by the measurement and determination of only one of these parameters.